Radiative decays of B mesons at LHCb

Fatima Soomro

Blackett Laboratory

Imperial College London

June 17, 2011

Imperial College London

LHCb

A thesis submitted for the degree of Doctor of Philosophy in the

Department of Physics at Imperial College London

Declaration

The work reported in Chapters 4, 7 and 8 has been carried out by the author, except when explicit references are made to other works. The author also developed the HLT2 algorithm for radiative decays (Section. 6.1.2) and the analysis algorithm for the Laser Monitoring system of the LHC*b* Ring Imaging Cherenkov Detectors (Section. 5.3.1). The details of these are documented in LHC*b* notes [1, 2] and therefore not fully reproduced in this text.

Abstract

This thesis is dedicated to the study of radiative decays of B mesons at LHCb. At quark level, such decays are a $b \to s\gamma$ transition and take place via a penguin loop and are sensitive to virtual contribution of New Physics, which can be indicated by an increase in the decay rates. These decays also offer the possibility to test the V-A structure of the Standard Model coupling in the processes mediated by loop penguin diagrams.

In the decay $B_s \to \phi\gamma$, New Physics contribution can be probed by measuring the polarization of the photon in this decay. Systematic effects in the proper time reconstruction of the B_s in $B_s \to \phi\gamma$ can bias the photon polarization measurement in this decay, which will reduce the sensitivity on the relevant New Physics parameter. The author studied those effects and developed ideas to calibrate them using $B_d \to K^*\gamma$ and $B_s \to J/\psi\phi$ decays as control channels. These studies are mostly Monte Carlo based, due to a relatively small data set from the 2010 running. However, some studies and cross checks have indeed been performed with data.

The author developed the trigger and stripping (another level of skimming the data, after the trigger) selections for $B_s \to \phi\gamma$ and $B_d \to K^*\gamma$ decays, and made a major contribution to the selection of the first significant sample of $B_d \to K^*\gamma$ from the 2010 data set of LHCb.

Acknowledgements

The three and half years I spent doing my PhD have been very memorable, although difficult at times. I would first and foremost like to thank the Higher Education Commission of Pakistan for funding this degree and the LHCb UK collaboration for hosting me in Geneva.

The Imperial College LHCb group were an excellent lot to work with, so were the LHCb collaboration members at CERN. Below is a list, by no means exhaustive, of people who made this time very productive and enjoyable

- My supervisor Dr. Bill Cameron, who had all the patience for my stupid questions
- My supervisor Prof. Andrei Golutvin, Dr. Ulrik Egede and Prof. Peter Dornan, whom I cannot thank enough for their help and guidance
- Patrick Koppenburg, Vanya Belyaev and Olivier Deschamps at CERN, for all their help with understanding the HLT and stripping software, photon reconstruction and the subtleties of the $B_s \to \phi\gamma$ analysis
- Thomas Blake, my LHCb software guru. What would I have done with out you!
- Chris Blanks, Will Reece, Thomas Blake and Kim Vervink for all the coffee breaks at CERN. Special thanks to Chris Blanks for being such a nice office mate
- Bharti Aggarwal, Anil Inkar, Mirza Attiq and Muhammad Zakir for making my stay at CERN hostel fun. Special mention for Bharti's excellent cooking and Attiq's exquisite driving
- Akhtar Rind for hosting me in Durham and the excellent company
- My teacher Altaf Nizamani, for being a friend, philosopher and guide
- My brother Khaleel Soomro, for being him, and most of all my mother who made me what I am. Special is an understatement for you, I love you ammi

Contents

1 Introduction **8**

2 The Standard Model of Particle Physics **12**

2.1 Introduction 12

2.2 The electromagnetic force 12

2.3 The strong force 14

2.4 The electroweak force 16

2.5 Open issues in the SM and outlook 19

3 *CP* violation and flavour physics **24**

3.1 Introduction to *CP* violation 24

3.2 *CP* violation formalism 27

3.2.1 Types of *CP* violation 29

3.2.2 Time evolution of flavour eigenstates 31

3.2.3 Decay rate asymmetries 33

3.3 *CP* violation: the SM explanation 34

3.3.1 The CKM matrix and Unitarity triangle 37

3.3.2 Summary and Future prospects 49

4 Probing the helicity structure of New Physics **51**

4.1 Introduction . . . 51
4.1.1 Low q^2 region and photon polarization . . . 55
4.1.2 $B \to f_{CP}\gamma$ decay rate and photon polarization . . . 56
4.1.3 Tagged and untagged analysis of $B \to f_{CP}\gamma$ . . . 58
4.2 Measuring $\mathcal{A}^{\Delta}$ at LHCb . . . 61
4.2.1 Signal yield . . . 61
4.2.2 Extraction of $\mathcal{A}^{\Delta}$ . . . 61
4.2.3 LHCb resolution on $\mathcal{A}^{\Delta}$ . . . 64
4.2.4 Measurement of $\mathcal{A}^{\Delta}$ and input parameters . . . 66
4.3 Summary . . . 71

5 The LHCb detector and its performance **73**
5.1 Introduction . . . 73
5.1.1 Detector Layout . . . 75
5.2 VELO . . . 77
5.3 The RICH Detectors . . . 79
5.3.1 Monitoring of the RICH mirrors . . . 80
5.3.2 The RICH PID performance . . . 85
5.4 The Tracking system . . . 87
5.5 Calorimeter . . . 88
5.6 Summary . . . 92

6 The LHCb trigger **93**
6.1 Introduction . . . 93
6.1.1 L0 calorimeter trigger for radiative decays . . . 95
6.1.2 HLT for radiative decays . . . 97
6.2 Summary . . . 99

7 Radiative signal in the 2010 data set **100**

7.1 Trigger evolution in 2010 . . . 103

7.2 Efficiency on signal and yield expectation . . . 106

7.3 $B_d \to K^*\gamma$ signal in data . . . 108

7.4 Data/MC comparison in SPD multiplicity . . . 110

7.4.1 Correction for SPD multiplicity . . . 113

7.5 Validation of L0 photon trigger in data . . . 115

7.5.1 Event samples used . . . 117

7.5.2 "Unconverted" photons . . . 118

7.5.3 Photons and π^0 content of samples . . . 118

7.5.4 L0 Photon efficiency . . . 119

7.6 Summary . . . 128

8 Reconstruction of proper time of $B_s \to \phi\gamma$ at LHC*b* **129**

8.1 Proper time reconstruction . . . 132

8.1.1 Momentum reconstruction and proper time . . . 134

8.1.2 Correction for photon momentum . . . 138

8.2 The proper time acceptance function . . . 140

8.2.1 $\phi \to KK$ vertex reconstruction in data . . . 144

8.2.2 Extracting $B_s \to \phi\gamma$ proper time acceptance from $B_d \to K^*\gamma$ . . . 147

9 Conclusions and outlook **150**

Bibliography **153**

Chapter 1

Introduction

Particle physics is the study of the fundamental constituents of matter and their interactions due to the fundamental forces. The Standard Model of Particle Physics is a theory that has been experimentally tested over several decades and provides a consistent description of the nature of the fundamental forces and particles, with some exceptions which will be noted later. In the Standard Model, there are two broad classes of particles, bosons and fermions.

The matter particles, like electrons, are fermions, while bosons are the particles that serve as the mediators of forces between the fermions. There are two types of fundamental fermions, leptons and quarks. While the electron is the most famous charged lepton, there is another kind of lepton called the neutrino, which is electrically neutral. Furthermore, there are three known "generations" of leptons each consisting of a lepton and its accompanying neutrino. The first generation leptons are the electron (e) the electron neutrino (ν_e), and the second and third generation leptons are the muon (μ) and the tau (τ) respectively, along with their associated neutrinos. They are summarised in table 1.1.

Generation	Leptons	Quarks
1^{st}	ν_e, e^-	$u^{2/3}$, $d^{-1/3}$
2^{nd}	ν_μ, μ^-	$c^{2/3}$, $s^{-1/3}$
3^{rd}	ν_τ, τ^-	$t^{2/3}$, $b^{-1/3}$

Table 1.1: Summary of the three generations of matter particles. The superscripts are their electric charges.

Unlike leptons, quarks are never observed in isolation. They are observed only in composite states called Hadrons, famous examples of which are protons and neutrons. Hadrons are further classified into mesons and baryons; mesons are quark anti-quark combinations while baryons are three quark combinations. Like the leptons, quarks also come in three generations, and each generation is composed of two quarks. The *up* and *down* quarks constitute the first generation, *charm* and *strange* constitute the second generation, while *top* and *bottom* are the third generation quarks (table 1.1).

The Standard Model is a quantum field theory in which forces are described in terms of the exchange of their field quanta. The Standard Model describes three fundamental forces of nature, the strong force, the electromagnetic force and the weak force. Each of these forces is mediated by its own carrier boson(s) and the strength of the force is encoded in a quantity called the "coupling constant".

The strong force has eight carriers, all of which are massless and chargeless, but posses a property called "colour" by virtue of which they mediate interactions between the quarks, which also possess this property. The electromagnetic force has only one chargeless and massless carrier, the photon. The weak force has three massive carriers, two of which are charged while one is neutral.

The Electromagnetic and Weak forces were hypothesised to be manifestations of a single force [3, 4], called the Electroweak force. The bosons postulated to exist as a result of such a theory were found experimentally and the agreement between the Standard Model prediction and the experiment in the precision tests of the electroweak sector [5, 6] is a compelling example of the success of the Standard Model.

The Higgs mechanism [7] is an important part of the Standard Model electroweak sector, as it was proposed to generate masses for the weak bosons. The Higgs boson has not yet been observed, hence the mechanism is not experimentally proven. Another shortcoming of the Standard Model framework is that it does not incorporate the gravitational force. This hints at the fact that the Standard Model is not the complete theory of nature but a very good low energy approximation of it. Much like Newton's equations, which are a very good low energy approximation of the theory of relativity.

Another open question is the matter antimatter asymmetry in the Universe. The Universe is postulated to have begun (a fraction of a second after the Big Bang) with equal amounts of matter and antimatter. However, the latter is not found in the Universe in an appreciable amount. In the Standard Model, this asymmetry is incorporated in the form of *CP* violation which is discussed in later chapters. However, the observed amount of *CP* violation is by far not sufficient to generate the matter anti matter asymmetry observed in the Universe.

Particle physics is driven by the quest to understand the core working principles of nature and to fill in the gaps in our knowledge of nature. So, most of the recent effort in this field is dedicated to the pursuit of the "beyond Standard Model" or "New Physics", which will hopefully provide insights into the unexplained phenomena. There are two approaches

to look for New Physics, one is the direct approach which is to look for and discover beyond Standard Model particles. This has been undertaken by the Tevatron experiments and is now being pursued by the general purpose detectors, CMS and ATLAS at the LHC. The other approach is an indirect search for New Physics, by looking for its effects in the decays of heavy flavour particles we have already discovered. Experiments like *BABAR*, BELLE, CLEO, ARGUS and also the Tevatron experiments have made great progress with this approach. The LHCb experiment at CERN is now taking their legacy further. This thesis is dedicated to the study of radiative decays of B mesons with the LHCb detector, as such decays have a rich phenomenology and are excellent probes of New Physics.

In particular, most of the work reported in this thesis is towards making a measurement of the fraction of left to right handed photons in $B_s \to \phi\gamma$ (the decay of a $\bar{b}$ quark), as this quantity is sensitive to New Physics. The author has demonstrated the importance of various systematic effects on this analysis (Chapter 4) and studied ways to correct for most of them using $B_d \to K^*\gamma$ and $B_s \to J/\psi\phi$ decays, some studies with data relevant to this issue are reported in Chapter 8.

While it is optimal to develop data driven methods to evaluate and correct for systematic uncertainties, near perfect agreement between Monte Carlo and data is essential to understanding key issues relating to the photon reconstruction at the trigger and offline level. This understanding is central to the extraction of various efficiencies and biases from data themselves. The author performed initial studies with the 2010 data set to validate the photon reconstruction at the trigger and offline level, and evaluate the efficiency of the former from data (Chapter 7). In addition to that, the author developed and tuned the trigger chain to select radiative decays during the 2010 data taking period. The validation studies reported in this thesis were an important input to the tuning of the trigger for the 2011 data taking.

Chapter 2

The Standard Model of Particle Physics

2.1 Introduction

The Standard Model (SM) is a gauge theory based on the symmetry group

$$SU(3)_c \otimes SU(2)_L \otimes U(1)_Y \tag{2.1}$$

where $SU(3)_c$ is the gauge group describing the strong interaction and $SU(2)_L \otimes U(1)_Y$ is the gauge group describing the electroweak interaction. We discuss the three gauge interactions starting with the electromagnetic one.

2.2 The electromagnetic force

The Electromagnetic (EM) force is mediated by the photon, which is a spin 1 particle. The photon, the gauge boson of the EM field, arises from requiring the fermion Lagrangian to be invariant under local gauge transformations.

Let $\psi(x)$ and $\bar{\psi}(x)$ be the electron and positron fields, then a local gauge transformation on them is given by

$$\begin{aligned} \psi(x) &\longrightarrow \psi'(x) = e^{i\alpha(x)}\psi(x) \\ \bar{\psi}(x) &\longrightarrow \bar{\psi}'(x) = e^{-i\alpha(x)}\bar{\psi}(x) \end{aligned} \tag{2.2}$$

where α is a function of the space time coordinates. Then, the free fermion Lagrangian,

$$\mathcal{L} = i\bar{\psi}\gamma^{\mu}\partial_{\mu}\psi - m\bar{\psi}\psi \tag{2.3}$$

is not invariant under the transformation of ψ as in Eq. 2.2, as it will pick a term of the form $\bar{\psi}\gamma^{\mu}\psi\partial_{\mu}\alpha(x)$. Symmetry under such a transformation can be restored by introducing a field A_{μ} and the "covariant" derivative $D_{\mu} = \partial_{\mu} - ieA_{\mu}$, where A_{μ} transforms as

$$A_{\mu} \longrightarrow A'_{\mu} = A_{\mu} + \frac{1}{e}\partial_{\mu}\alpha(x) \tag{2.4}$$

The Lagrangian can then be written as

$$\begin{aligned} \mathcal{L} &= i\bar{\psi}\gamma^{\mu}D_{\mu}\psi - m\bar{\psi}\psi \\ &= \bar{\psi}\left(i\gamma^{\mu}\partial_{\mu} - m\right)\psi + e\bar{\psi}\gamma^{\mu}\psi A_{\mu} \end{aligned} \tag{2.5}$$

which is invariant under a local gauge transformation of ψ as in Eq. 2.2.

Therefore, in order to restore invariance under local gauge transformation, we need to introduce an interaction between the fermion current $j = \bar{\psi}\gamma^{\mu}\psi$ and a vector field A_{μ}.

The complete EM Lagrangian can be obtained by adding a gauge invariant kinetic energy term for the vector field as well,

$$\mathcal{L} = \bar{\psi}\left(i\gamma^{\mu}\partial_{\mu} - m\right)\psi + e\bar{\psi}\gamma^{\mu}\psi A_{\mu} - \frac{1}{4}F_{\mu\nu}F^{\mu\nu} \tag{2.6}$$

where the first piece is the free fermion part and the middle one describes the interaction between the vector field (EM field in this case) and the fermion current with a strength measured by e. The last term is the kinetic Lagrangian term for the vector field where $F_{\mu\nu} = \partial_{\mu}A_{\nu} - \partial_{\nu}A_{\mu}$ is the electromagnetic field strength tensor.

A Lagrangian can be developed for the other two interactions (the strong and weak interactions) by following similar logic.

2.3 The strong force

The strong force acts on quarks and is responsible for binding them in hadrons. Quarks come in three known families and each family has two *flavours* of quarks. Each of these six flavours of quarks comes in "colours"; red, blue and green, where colour is just an imaginative label having nothing to do with the every day concept of colours.

Although quarks of different flavours have different masses, the quarks of the same flavour but different colours have the same mass. The free fermion part of the Lagrangian, for a particular flavour of the quark, can be written as

$$\mathcal{L} = \left[i\bar{\psi}\gamma^{\mu}\partial_{\mu}\psi - m\bar{\psi}\psi\right] \tag{2.7}$$

where $\psi = \begin{pmatrix} \psi_r \\ \psi_b \\ \psi_g \end{pmatrix}$ and $\bar{\psi} = \begin{pmatrix} \bar{\psi}_r & \bar{\psi}_b & \bar{\psi}_g \end{pmatrix}$. As in the previous section, we now require that it is invariant under a transformation of the form

$$\psi \rightarrow e^{iH}\psi, \qquad (\bar{\psi} \rightarrow \bar{\psi}e^{-iH}) \tag{2.8}$$

where H is a 3×3 hermitian matrix , i.e. $H^\dagger = H$

A 3×3 hermitian matrix can be represented in terms of nine real numbers, say, $\theta, a_1, a_2, ..., a_8$ as $H = I\theta + \lambda.a$, where I is the 3×3 unit matrix and the λ_i (i=1,2, ...,8) are the Gell-Mann matrices. $\lambda.a$ is a shorthand for $\lambda_1 a_1 + \lambda_2 a_2 + ...$ etc

In order for the Lagrangian to be invariant under a transformation of the form,

$$\psi \rightarrow S\psi, \qquad \text{where} \quad S = e^{iq\lambda.\phi(x)} \qquad \text{and} \quad \phi = \frac{a}{q} \tag{2.9}$$

(where q is a coupling similar to e in the EM case) we introduce the appropriate covariant derivative $D_\mu = \partial_\mu - iq\lambda.A_\mu$ and also the appropriate field transformations. The modified lagrangian of Eq. 2.7 is then

$$\mathcal{L} = i\bar{\psi}\gamma^\mu D_\mu\psi - m\bar{\psi}\psi = \left[i\bar{\psi}\gamma^\mu\partial_\mu\psi - m\bar{\psi}\psi\right] - \left(q\bar{\psi}\gamma^\mu\lambda\psi\right)A_\mu \tag{2.10}$$

and is invariant under the transformation of Eq. 2.9. Requiring this invariance means we have to add eight new fields A^a_μ to the theory (where a is the colour index), which are interpreted as the eight gluons.

And adding the free gluon part to the Lagrangian, we get

$$\mathcal{L} = \left[i\bar{\psi}\gamma^{\mu}\partial_{\mu}\psi - m\bar{\psi}\psi\right] - \left(q\bar{\psi}\gamma^{\mu}\lambda\psi\right) A^{a}_{\mu} + \frac{1}{4}F^{\mu\nu}F_{\mu\nu} \tag{2.11}$$

We need six of such equations (for up and down type quarks of the three generations) with the appropriate masses to complete the picture, but the conclusion is that the colour force is mediated by eight massless gluons, which arise from a requirement of invariance of the quark fields under SU(3) gauge transformations.

This Lagrangian has a form similar to Eq. 2.6, where the first term represents free fermions (quarks), the middle one describes an interaction of the quark current $j_{\mu} = \bar{\psi}\gamma^{\mu}\lambda\psi$ with the gluon fields A^{a}_{μ}, and the last term is the kinetic term for the latter.

2.4 The electroweak force

Fermions have been observed to interact via the weak interaction, given by charged currents of the form (Fig. 2.1)

$$\begin{aligned} j^{-}_{\mu} &= \bar{\nu}_L\gamma_{\mu}e_L \\ j^{+}_{\mu} &= \bar{e}_L\gamma_{\mu}\nu_L \end{aligned} \tag{2.12}$$

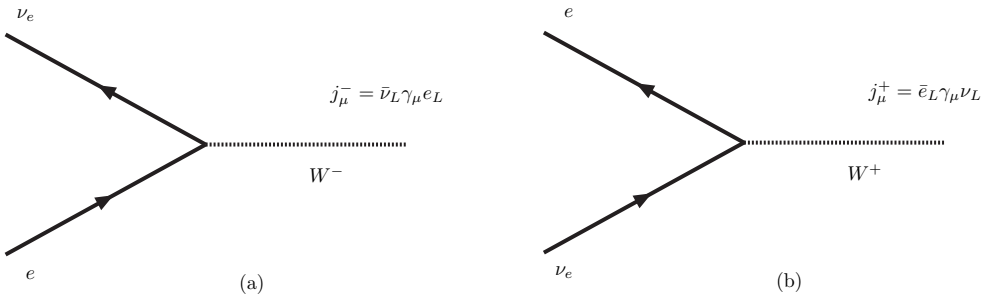

Figure 2.1: Charged current mediated by the W bosons.

Therefore, for weak interactions, we can write the fermion fields as left handed doublets

$$q_L = \begin{pmatrix} u_L \\ d_L \end{pmatrix}, \quad l_L = \begin{pmatrix} \nu_e \\ e^- \end{pmatrix} \tag{2.13}$$

Again, as in the case of the previously discussed forces, we require local gauge invariance under a transformation of the form $\chi_L \rightarrow e^{iH}\chi_L$, where χ_L is any of the left handed doublets q_L and l_L.

In this case, H is a 2×2 hermitian matrix and can be represented as $H = I\theta + \tau.a$, where the τ_i are 2×2 matrices and a_1, a_2, a_3 and θ are real numbers. The matrices τ^i for the case of charged current interactions can be identified with the following combinations of the first two Pauli matrices

$$\tau^{\pm} = \frac{1}{2}(\tau^1 \pm i\tau^2) \tag{2.14}$$

Introducing a third matrix to represent neutral current interactions $\frac{1}{2}\tau^3 = \frac{1}{2}\begin{pmatrix} 1 & 0 \\ 0 & -1 \end{pmatrix}$, we get currents of the form $j^3_\mu = \chi_L\gamma_\mu\tau^3\chi_L = \frac{1}{2}\bar{\nu}_L\gamma_\mu\nu_L - \frac{1}{2}\bar{e}_L\gamma_\mu e_L$.

However, these only represent weak neutral currents for left handed fermions, but right handed fermions also have neutral current interaction. This is addressed by introducing the "weak hypercharge" current

$$j^Y_\mu = 2j^{EM}_\mu - 2j^3_\mu \tag{2.15}$$

where j_μ^{EM} is the electromagnetic current $j_\mu^{EM} = -\bar{e}_L\gamma_\mu e_L - \bar{e}_R\gamma_\mu e_R$, so that

$$j_\mu^Y = -2\bar{e}_R\gamma_\mu e_R - \bar{e}_L\gamma_\mu e_L - \bar{\nu}_L\gamma_\mu\nu_L \tag{2.16}$$

The Z boson cannot "only" mediate the j_μ^3 current as it is known to have right handed couplings as well. So it must be a mixture of the neutral (W^3) field of the weak SU(2) and the weak hypercharge field (A^μ) of the U(1)$_Y$ (where the subscript Y denotes hypercharge). The physical bosons are then

$$\begin{aligned} Z^\mu &= W_3^\mu \cos\theta_W - Y^\mu \sin\theta_W \\ A^\mu &= W_3^\mu \sin\theta_W + Y^\mu \cos\theta_W \end{aligned} \tag{2.17}$$

where θ_W is the weak mixing angle and A^μ can be identified as the photon. The relationship between the coupling strengths g_W and g_Y can be found by requiring that the field A^μ has the right interaction terms, i.e. of the photon. The relation is

$$g_Y = \frac{g_W e}{\sqrt{(g_W^2 - e^2)}}, \quad \text{and} \quad \sin\theta_W = \frac{e}{g_W} \tag{2.18}$$

We can now write the kinetic terms of the Lagrangian for the electroweak field

$$\mathcal{L}_{Kinetic} = -\frac{1}{4}W^i_{\mu\nu}W^{i\mu\nu} - \frac{1}{4}B_{\mu\nu}B^{\mu\nu} \tag{2.19}$$

The Ws and the Z are known to be massive, but we do not have a gauge invariant mass term for them in the Lagrangian. The Higgs mechanism was introduced to address this problem [7]. While the details can be seen in [7, 8], it is sufficient to note here that this mechanism works by introducing a pseudo scalar field, with a non zero vacuum expectation value, into the theory. This field is known as the Higgs field and its associated quantum as

the Higgs boson. The interaction terms between the boson fields of the weak interaction and the Higgs field can be interpreted as the mass terms for the former.

Fermion mass terms can also be attributed to their interaction with the Higgs field as[1]

$$\begin{aligned} \mathcal{L}^{e}_{mass} &= c_e \left[\left(l^{\dagger}_{L} \Phi \right) e_R + e^{\dagger}_{R} \left(\Phi^{\dagger} l_L \right) \right] \\ &= c_e \left[\left(\nu^{\dagger}_{L} \Phi_A + e^{\dagger}_{L} \Phi_B \right) e_R + e^{\dagger}_{R} \left(\Phi^{\dagger}_{A} \nu_L + \Phi^{\dagger}_{B} e_L \right) \right] \end{aligned} \tag{2.20}$$

where l_L is the doublet in Eq. 2.13, e_R is the right handed singlet, c_e is a constant and Φ is the Higgs field with a vacuum expectation value ν

$$\Phi = \begin{pmatrix} 0 \\ \nu + h \end{pmatrix} \tag{2.21}$$

then $\mathcal{L}^{e}_{mass}$ can be written as

$$\mathcal{L}^{e}_{mass} = c_e \nu (e^{\dagger}_{L} e_R + e^{\dagger}_{R} e_L) + (c_e h)(e^{\dagger}_{L} e_R + e^{\dagger}_{R} e_L) \tag{2.22}$$

So, the fermion masses $m_e = c_e \nu$ are proportional to ν, the vacuum expectation value of the Higgs field, and their couplings to the Higgs field h are proportional to their mass, as $c_e h = \frac{m_e}{\nu} h$.

2.5 Open issues in the SM and outlook

The following is a (by no means exhaustive) list of some questions unanswered by the SM:

[1] Eq. 2.20 considers only the first generation leptons

- Neutrino masses: Notice in Eq. 2.22 that the mass terms consist of fermion fields with the opposite handedness. Since there are no right handed neutrinos in the SM, a mass term for them cannot be introduced via this mechanism. Experimentally, neutrinos have been observed to have mass, and this is one of the puzzles the SM has not been able to solve.

- Particle masses: In the SM, masses for elementary particles are postulated to be generated by their interaction with the Higgs field, but the Higgs boson remains the only SM particle that has not been experimentally observed. The Tevatron experiments have performed extensive searches and have narrowed down the allowed phase space for the Higgs, but particle and the mechanism remain a mystery, probably until the former's discovery. Also, the pattern of masses of the three generations of fermions is not understood, i.e. the fact that the first generation leptons are an order of magnitude lighter than the second generation ones, and the latter are much lighter than the third generation fermions.

- The hierarchy problem: It is the question of why the plank scale (10^{19} GeV), where gravity becomes relevant as a force, and the masses of the observed particles are so different. It also manifests in a very large mass for the Higgs boson as it gets quantum corrections to its mass from all the particles that couple to it. The mass of Higgs is brought to the electroweak scale by "fine tuning" parameters in the theory, which is unsatisfactory for a complete theory.

- Dark matter: The amount of observable matter in the Universe is too small to explain the cosmological observations of the rotational speed of galaxies [9]. Therefore, it is speculated that most of the 'matter' in the Universe is non baryonic and weakly interacting, and has hence escaped detection. The SM does not offer any dark matter candidate.

- Free parameters: There are 19 free parameters in the SM which have to be determined experimentally as the theory does not predict their values. This is again unsatisfactory.

- Number of generations: Three generations of quarks and leptons have been observed experimentally, but the SM offers no prediction for that number, nor an explanation of why this number is three.

- Unification: The idea of unification of fundamental forces comes from the electroweak (and even electromagnetic) unification, i.e. that two seemingly different forces unify into a single one at sufficiently high energies. It is not possible to unify the electroweak and strong forces by the SM extrapolation of their coupling constants. It should also be noted here that gravity, one of the four fundamental forces, is not a part of the SM i.e. not incorporated in its theoretical framework.

- Matter anti-matter asymmetry in the Universe: As discussed previously, the SM offers no adequate explanation for this asymmetry. It was pointed out by Andrei Sakharov [10] that such an asymmetric configuration can be reached from a symmetric one (the early Universe had equal amounts of matter and anti matter) only if three conditions are satisfied, namely C and *CP* symmetries are violated, baryon number is violated, and the Universe goes through a period of non thermal equilibrium. Baryon number violation has been looked for but there is no evidence for it yet, while *CP* violation is incorporated in the SM as will be discussed in Chapter. 3. However, the currently observed level of *CP* violation is of the order of 10^{-20} [11], which is orders of magnitude below the baryon-to-photon ratio of the universe. The latter is about 10^{-9}, which is a strong argument for the presence of yet undiscovered sources of *CP* violation.

In the light of the above, we learn that the SM is not "the" complete theory but a very good low energy approximation of it, and hence, we must search for the beyond SM physics to find the theory that completely describes the nature of fundamental particles and forces. Theoretically, many extensions of the SM have been proposed, a popular example is the Supersymmetric theory. It offers a solution to the divergence of the Higgs mass by introducing supersymmetric partners of all the known particles. The quantum corrections to the Higgs mass due to SM particles are then cancelled by the corrections due to their supersymmetric partners, bringing the Higgs mass to electroweak scale without any fine tuning. Another attractive feature of supersymmetry is that it offers a dark matter candidate. The non observation of the supersymmetric particles yet implies that it is a broken symmetry, i.e. the supersymmetric particles have much higher masses than their SM counterparts. However, the former can be produced at hadron colliders like the Tevatron and the LHC. Therefore, it is up to the experiment to find the *beyond* SM or *New* Physics. The indirect way is to look for New Physics contributions in decays mediated by loops. The following table summarises the New Physics sensitivity of different types of measurements from loop decays.

Measurements in loop decays	New Physics properties probed
Decay rates	Couplings/masses of New Physics
CP violating observables	Phases of New Physics
Angular observables	Helicity structure of New Physics

Table 2.1: A summary of the types of measurements possible with loop decays and the properties of New Physics that they probe.

The rates of radiative penguin decays like $B_s \to \phi\gamma$, $B_d \to K^*\gamma$ (and $b \to s\gamma$), and electroweak penguin decays $B_d \to K^{*0}\mu^+\mu^-$ (and $b \to s\ell^+\ell^-$) have been measured and found to be consistent with SM predictions. In the case of the super rare decay $B_s \to \mu\mu$, the field is very much open. The SM prediction for its branching ratio is $(3.35\pm0.32)\times10^{-9}$,

while the current experimental limit is at $< 4.3 \times 10^{-8}$ [12], which is from a $3.7\,\mathrm{fb}^{-1}$ data set of the CDF experiment. LHCb has already reached a similar sensitivity, with a limit of $BR(B_s \to \mu\mu) < 5.6 \times 10^{-8}$ [13] using a data set corresponding to only $37\,\mathrm{pb}^{-1}$. The *CP* violating phases and helicity structure are also sensitive probes of New Physics, as will be discussed in Chapters. 3 and 4.

Chapter 3

CP violation and flavour physics

3.1 Introduction to CP violation

Symmetry of a physical system is interpreted as the invariance of a system under a certain transformation. For instance, if one inverts the spatial coordinates of a classical system, physical laws would still hold, which means that the system exhibits symmetry with respect to spatial transformations. This is an example of a discrete symmetry. Similarly, a sphere rotated around its axis will appear exactly the same, and hence exhibits spherical symmetry, which is a continuous symmetry. Symmetries are important in physics because invariance under a symmetry results in a conservation law. For example, invariance under time translation results in the conservation of energy, and rotational invariance results in the conservation of angular momentum.

Here we consider the invariance of systems under a simultaneous inversion of charge (C) and parity (P), or the CP symmetry. It is a discrete symmetry and essentially means that a system is invariant under a transformation of all its particles into their anti particles and a mirror reflection of its coordinate system.

Both C and P are conserved by the electromagnetic and strong interactions but not by the weak interaction. Parity violation in the weak interaction was demonstrated by Wu et al in 1956 [14] in nuclear beta decay and in *pion* decays [15], after the suggestion by Lee and Yang [16]. Non conservation of C is a direct consequence of P violation as argued by Lee, Oehme and Yang [17]. After the establishment of P and C violation, the combined symmetry CP was considered to be conserved in nature [18], until another experiment found otherwise [19].

In 1964, Cronin and Fitch demonstrated CP violation in weak interaction, by studying the decays of neutral *Kaons* (mesons consisting of an s quark) into *pions* [19]. The K_L meson is CP odd and should not decay to two pion final states if CP is conserved. Cronin and Fitch observed the decay $K_L \rightarrow \pi\pi$, which is a CP even final state, providing evidence for CP violation. Nevertheless, this CP violation is small, and about 1 in 500 K_L will decay into two pions. CP violation in the decays of neutral *kaons* is due to a phenomenon called 'mixing', which is described below.

Kaon mixing and oscillation

The neutral *Kaon* K^0 is produced in strong interactions and has a quark composition of $\bar{s}d$. Its anti particle is $\bar{K^0}$ with the quark composition $s\bar{d}$. The strong interaction conserves the "strangeness" quantum number, and the neutral *Kaons* are in a state of definite "strangeness" when they are produced via strong interaction. However, they decay via the weak interaction which does not conserve "strangeness", i.e. the strangeness eigenstates (as neutral *Kaons* are produced) are not the eigenstates of the weak interaction. The particles that decay are a mixture of the originally produced states of definite strangeness.

If CP were to be conserved, the mixed states of K^0 and $\bar{K^0}$ would be given by $\mid K_1^0\rangle$ and $\mid K_2^0\rangle$

$$CP \mid K^0\rangle = \mid \bar{K^0}\rangle, \quad CP \mid \bar{K^0}\rangle = \mid K^0\rangle \tag{3.1}$$

$$\mid K_1\rangle = \left(\frac{1}{\sqrt{2}}\right)(\mid K^0\rangle + \mid \bar{K^0}\rangle), \quad \mid K_2\rangle = \left(\frac{1}{\sqrt{2}}\right)(\mid K^0\rangle - \mid \bar{K^0}\rangle) \tag{3.2}$$

where K_1 and K_2 are the CP even and odd states respectively. Two neutral *Kaon* states have been experimentally observed, with definite mass and lifetimes. The *Kaons* decay weakly, and the weak interaction does not conserve CP, hence the physical states (K_s and K_L) that decay are not eigenstates of CP but their mixture

$$\mid K_s\rangle = \frac{(K_1 + \epsilon K_2)}{\sqrt{1+|\epsilon|^2}}, \quad \mid K_L\rangle = \frac{(K_2 + \epsilon K_1)}{\sqrt{1+|\epsilon|^2}} \tag{3.3}$$

Therefore, K_s and K_L have small contamination of CP odd and even components respectively, quantified by ϵ which has been experimentally measured to be 2.3×10^{-3}.

Since the original measurement of Cronin and Fitch [19], CP violation has also been observed in B mesons, particles containing b quarks, and extensive experimental and theoretical work has taken place to qualify and quantify this effect. While CP violation in the *Kaon* system led to many insights into this entirely new phenomenon, B mesons offer a richer ground due to their larger mass. Many more interesting final states are possible in B meson decays as compared to *Kaons*, and therefore, have been the focus of not only B factories but also the Tevatron experiments. The LHCb experiment is built specifically to look for hints of New Physics in decays of B mesons. In the rest of this chapter, we describe the CP violation formalism in some detail.

3.2 *CP* violation formalism

For a generic neutral meson M^0, flavour eigenstates produced in strong interactions are not *CP* eigenstates

$$CP|M^0\rangle = |\bar{M}^0\rangle, \quad CP|\bar{M}^0\rangle = |M^0\rangle \tag{3.4}$$

so we construct the *CP* eigenstates as

$$M_+ = |M^0\rangle + |\bar{M}^0\rangle, \qquad M_- = |M^0\rangle - |\bar{M}^0\rangle \tag{3.5}$$

Then, the flavour eigenstates can be written in terms of *CP* eigenstates as

$$M^0 = \frac{1}{\sqrt{2}}\left(|M_+\rangle + |M_-\rangle\right), \qquad \bar{M}^0 = \frac{1}{\sqrt{2}}\left(|M_+\rangle - M_-\rangle\right) \tag{3.6}$$

where the $\frac{1}{\sqrt{2}}$ is for normalization. Now consider the time evolution of the flavour eigenstates

$$i\frac{d}{dt}\psi = \mathcal{H}\psi, \qquad \psi = \begin{pmatrix} M^0 \\ \bar{M}^0 \end{pmatrix} \tag{3.7}$$

where $\mathcal{H}$ is the Hamiltonian, and can be written as the combination of two hermitian matrices $\mathcal{M}$ and Γ as

$$\mathcal{H} = \mathcal{M} - \frac{i}{2}\Gamma = \begin{pmatrix} M_{11} - i\frac{\Gamma_{11}}{2} & M_{12} - i\frac{\Gamma_{12}}{2} \\ M_{21} - i\frac{\Gamma_{21}}{2} & M_{22} - i\frac{\Gamma_{22}}{2} \end{pmatrix} \tag{3.8}$$

CPT invariance requires the masses and decay rates of particles and anti-particles to be equal. For this to be true, the diagonal elements of $\mathcal{H}$ should be equal, i.e. $\mathcal{H}_{11} = \mathcal{H}_{22}$, and the hermicity of $\mathcal{M}$ and Γ implies $\mathcal{H}_{21} = \mathcal{M}_{12}^* - i\frac{\Gamma_{12}^*}{2}$. The ψ of Eq. 3.7 is not an eigenstate of the above Hamiltonian, but we can construct its eigenstates by combining the two flavour eigenstates M^0 and $\bar{M}^0$. The physical states, which we choose to denote by H and L for "heavy" and "light" can then be written as

$$\mathcal{H}|M_{H,L}\rangle = \left(m_{H,L} - i\frac{\Gamma_{H,L}}{2}\right)|M_{H,L}\rangle \tag{3.9}$$

the states H and L have distinct masses and decay widths. The mass and decay width difference between them, and the average decay width ($\bar{\Gamma}$) are defined as

$$\Delta m \equiv m_H - m_L, \quad \Delta\Gamma \equiv \Gamma_H - \Gamma_L, \quad \bar{\Gamma} \equiv \frac{1}{2}\left(\Gamma_H + \Gamma_L\right) \tag{3.10}$$

The time evolution of the physical states is given by

$$|M_{H,L}(t)\rangle = e^{-im_{H,L}t}e^{-\frac{\Gamma_{H,L}}{2}t}|M_{H,L}(0)\rangle \tag{3.11}$$

and their expression in terms of the flavour eigenstates is

$$|M_H\rangle = p|M^0\rangle + q|\bar{M}^0\rangle, \qquad |M_L\rangle = p|M^0\rangle - q|\bar{M}^0\rangle \tag{3.12}$$

Note here that while the flavour and *CP* eigenstates are orthogonal, the physical states are not

$$\langle M^0|\bar{M}^0\rangle = 0, \qquad \text{and} \qquad \langle M_+|M_-\rangle = 0 \tag{3.13}$$

$$\langle M_H|M_L\rangle = p^*q - q^*p = \xi \tag{3.14}$$

Therefore, if *CP* symmetry is to hold, $\frac{p}{q} = 1$, i.e. the physical states coincide with the *CP* eigenstates.

3.2.1 Types of *CP* violation

CP violation can be classified in the following types

- ***CP* violation in mixing**

  This type of *CP* violation is due to the fact that $|q|^2 \neq |p|^2$ and physical states do not coincide with flavour eigenstates. In presence of *CP* violation in mixing, there are two amplitudes in the decay of a meson (or anti meson) with different phases, one from $M^0 \to \bar{M}^0$ and one from $\bar{M}^0 \to M^0$.

- ***CP* violation in decay**

  This type of *CP* violation occurs if the decay amplitude of a process and its *CP* conjugate process are not equal, i.e. $|\bar{A}_{\bar{f}}| \neq |A_f|$. It requires the presence of at least two interfering decay amplitudes, with different weak and strong phases. This is also called "direct" *CP* violation and is the only type of *CP* violation for charged particles which cannot mix, due to the conservation of electric charge.

- ***CP* violation in interference of mixing and decay**

  Also called "mixing induced" *CP* violation, occurs when meson and anti meson can decay to a common final state configuration. It occurs due to the fact that such a meson can either decay directly to a final state or can oscillate to its conjugate state which then decays to the same final state. The overall amplitude for such a decay can be written as

$$A(M^0 \to f) + A(M^0 \to \bar{M}^0)A(\bar{M}^0 \to f)$$

If θ_M is the phase of mixing amplitude, and θ_f and $\bar{\theta}_f$ are the phases of M^0 and $\bar{M^0}$ decay amplitudes to f, then the two terms above have a relative phase of $\theta_f - \bar{\theta}_f - \theta_M$. For the *CP* conjugate process, the phase will be $\bar{\theta}_f - \theta_f - \bar{\theta}_M$, hence the decays of M^0 and $\bar{M^0}$ to the common final state f will have phases which differ not only in sign but also in magnitude, making possible a difference in the decay probabilities for M^0 and $\bar{M^0}$, which is a signal of *CP* violation. If there is different *CP* violation in different final states, then that can be characterized as direct *CP* violation as the mixing phase θ_M, is the same for all final states.

Signatures of *CP* violation

For dealing with decays into a common final state, one can define the parameter λ_f

$$\lambda_f = \frac{q}{p}\frac{\bar{A}_f}{A_f} \tag{3.15}$$

The phases involved in the mixing process can be written as

$$\frac{q}{p} = \left|\frac{q}{p}\right| e^{-2i\theta_M} \tag{3.16}$$

so that

$$Im(\lambda_f) = |\lambda_f| \sin(\bar{\theta}_f - \theta_f - 2\theta_M) \tag{3.17}$$

For the decays driven by a single amplitude, the phases to the final state f can be written as $\theta_f = \phi_f + \delta_f$ and $\bar{\theta}_f = -\phi_f + \delta_f$ where ϕ and δ are the weak and strong phases respectively.

Then Eq. 3.15 can be written as

$$\lambda_f = \left|\frac{q}{p}\right| e^{-2i(\theta_M+\phi_f)} \tag{3.18}$$

Generally, if *CP* symmetry holds

$$\lambda_f = \frac{1}{\lambda_{\bar{f}}} \tag{3.19}$$

If $q/p = 1$ and $|\bar{A}_{\bar{f}}| = |A_f|$, the above equation will hold for the magnitude but not for the phase, hence the signature of *CP* violation in the interference of mixing and decay is

$$arg(\lambda_f) + arg(\lambda_{\bar{f}}) \neq 0 \tag{3.20}$$

while for a *CP* eigenstate, *CP* violation in either mixing or decay is indicated by

$$|\lambda_f| \neq 1$$

and *CP* violation due to interference is indicated by

$$Im(\lambda_f) \neq 0$$

We will now explore in more detail some consequences of the different types of *CP* violation and their effect on measurable quantities like decay rates.

3.2.2 Time evolution of flavour eigenstates

Since physical states are not eigenstates of flavour, a state of definite flavour, say M^0, will evolve into a mixture of M^0 and $\bar{M}^0$. The time evolution of flavour eigenstates can be

expressed as

$$|M^0(t)\rangle = F_+(t)|M^0\rangle + \frac{q}{p}F_-(t)|\bar{M}^0\rangle \tag{3.21}$$

$$|\bar{M}^0(t)\rangle = \frac{p}{q}F_-(t)|M^0\rangle + F_+(t)|\bar{M}^0\rangle \tag{3.22}$$

where

$$F_\pm(t) = \frac{1}{2}e^{-im_L t}e^{-\Gamma_L t/2}\left[1 \pm e^{-i\Delta m t}e^{-\Delta\Gamma t/2}\right] \tag{3.23}$$

Therefore, the probability for a M^0 at t=0 to be a M^0 at a later time t is the same as the probability for a $\bar{M}^0$ at t=0 to be a $\bar{M}^0$ at time t, and is equal to $|F_+(t)|^2$. However, the probability for a M^0 at t=0 to be a $\bar{M}^0$ at a later time t is not the same as the probability for a $\bar{M}^0$ at t=0 to be M^0 at t. The two probabilities are

$$P\left[M^0(t) \to \bar{M}^0\right] = \left|\frac{q}{p}\right|^2 |F_-(t)|^2, \quad P\left[\bar{M}^0(t) \to M^0\right] = \left|\frac{p}{q}\right|^2 |F_-(t)|^2 \tag{3.24}$$

Using the above equations, the time dependent decay rates into a final state accessible to both flavour eigenstates can be written as

$$\Gamma\left[M^0(t) \to f\right] \propto \frac{1}{4}|A_f|^2\left[|F_+(t)|^2 + |F_-(t)|^2|\lambda_f|^2 + 2Re\left(f_+^*(t)f_-(t)\lambda_f\right)\right] \tag{3.25}$$

$$\Gamma\left[\bar{M}^0(t) \to f\right] \propto \frac{1}{4}|\bar{A}_f|^2\left[|F_+(t)|^2 + |F_-(t)|^2\frac{1}{|\lambda_f|^2} + 2Re\left(f_+^*(t)f_-(t)\frac{1}{\lambda_f}\right)\right] \tag{3.26}$$

where A_f and $\bar{A}_f$ are the amplitudes for M^0 and $\bar{M}^0$ to decay to the final state f, and the time dependence is contained in $f_\pm(t)$. Explicitly

$$\Gamma\left[M^0(t) \to f\right] \propto \frac{1}{4}\big[R_f^{(+)}e^{-\Gamma_L t} + R_f^{(-)}e^{-\Gamma_H t} + C_f e^{-\bar{\Gamma}t}\cos(\Delta m t) + S_f e^{-\bar{\Gamma}t}\sin(\Delta m t)\big] \tag{3.27a}$$

$$\Gamma\left[\bar{M}^0(t) \to f\right] \propto \frac{1}{4}\big[\bar{R}_f^{(+)}e^{-\Gamma_L t} + \bar{R}_f^{(-)}e^{-\Gamma_H t} + \bar{C}_f e^{-\bar{\Gamma}t}\cos(\Delta m t) + \bar{S}_f e^{-\bar{\Gamma}t}\sin(\Delta m t)\big] \tag{3.27b}$$

where

$$R_f^{(\pm)} = |A_f|^2 \left[|1 \pm \lambda_f|^2\right], \qquad \bar{R}_f^{(\pm)} = |\bar{A}_f|^2 \left[|1 \pm \tfrac{1}{\lambda_f}|^2\right] \tag{3.28}$$

$$C_f = 2|A_f|^2 \left(1 - |\lambda_f|^2\right), \qquad \bar{C}_f = 2|\bar{A}_f|^2 \left(1 - \tfrac{1}{|\lambda_f|^2}\right) \tag{3.29}$$

$$S_f = -4|A_f|^2 Im(\lambda_f), \qquad \bar{S}_f = -4|\bar{A}_f|^2 Im(\tfrac{1}{\lambda_f}) \tag{3.30}$$

and

$$R_f^{(\pm)} = \left|\tfrac{q}{p}\right|^2 \bar{R}_f^{(\pm)}, \quad C_f = -\left|\tfrac{q}{p}\right|^2 \bar{C}_f, \quad S_f = -\left|\tfrac{q}{p}\right|^2 \bar{S}_f \tag{3.31}$$

CP violation in mixing or decay introduces the $\cos(\Delta mt)$ terms which are visible in the decay rate from t=0, while *CP* violation in the interference of mixing and decay introduce the $\sin(\Delta mt)$ terms, which become visible after flavour oscillations have started.

3.2.3 Decay rate asymmetries

Eqs. 3.27 can be written in a form more convenient for the B meson system

$$\Gamma\left[M^0(t) \to f\right] \propto \frac{1}{2}|A_f|^2(1+|\lambda_f|^2)e^{-\bar{\Gamma}t}\big[\cosh(\Delta\Gamma t/2) + A_f^{(\Delta)}\sinh(\Delta\Gamma t/2) + A_f^{(MD)}\cos(\Delta mt) - A_f^{(I)}\sin(\Delta mt)\big] \tag{3.32}$$

$$\Gamma\left[\bar{M}^0(t) \to f\right] \propto \frac{1}{2}|A_f|^2\left|\frac{p}{q}\right|^2(1+|\lambda_f|^2)e^{-\bar{\Gamma}t}\big[\cosh(\Delta\Gamma t/2) + A_f^{(\Delta)}\sinh(\Delta\Gamma t/2) - A_f^{(MD)}\cos(\Delta mt) + A_f^{(I)}\sin(\Delta mt)\big] \tag{3.33}$$

where

$$A_f^{(MD)} = \frac{1-|\lambda_f|^2}{1+|\lambda_f|^2}, \quad A_f^{(I)} = \frac{2Im(\lambda_f)}{1+|\lambda_f|^2}, \quad A_f^{(\Delta)} = \frac{2Re(\lambda_f)}{1+|\lambda_f|^2} \tag{3.34}$$

The expressions for $\Gamma\left[M^0(t) \to \bar{f}\right]$ and $\Gamma\left[\bar{M}^0(t) \to \bar{f}\right]$ can be obtained by substituting λ_f by $\frac{1}{\lambda_{\bar{f}}}$. For decays which are unmixed or flavour specific, λ_f and $1/\lambda_{\bar{f}}$ are small or zero, and asymmetry can be written as

$$\Delta_f^{(Unmix)}(t) = \frac{\Gamma\left[\bar{M}^0(t) \to \bar{f}\right] - \Gamma\left[M^0(t) \to f\right]}{\Gamma\left[\bar{M}^0(t) \to \bar{f}\right] + \Gamma\left[M^0(t) \to f\right]} = \frac{|\bar{A}_{\bar{f}}|^2 - |A_f|^2}{|\bar{A}_{\bar{f}}|^2 + |A_f|^2} \equiv -\delta_A(f) \tag{3.35}$$

which is independent of time and sensitive only to *CP* violation in decay. In the limit of no *CP* violation in mixing, the asymmetry for decays into a single (non flavour specific) final state can be written as

$$\begin{aligned} \Delta_f(t) &= \frac{\Gamma\left[\bar{M}^0(t) \to f\right] - \Gamma\left[M^0(t) \to f\right]}{\Gamma\left[\bar{M}^0(t) \to f\right] + \Gamma\left[M^0(t) \to f\right]} \\ \Delta_f(t) &= \frac{A_f^{(I)} \sin(\Delta m t) - A_f^{(MD)} \cos(\Delta m t)}{\cosh(\Delta\Gamma t/2) + A_f^{(\Delta)} \sinh(\Delta\Gamma t/2)} \end{aligned} \tag{3.36}$$

Note than $A_f^{(MD)}$ parametrizes *CP* violation in mixing and in the decay, and reduces to $\delta_A(f)$ in case of no *CP* violation in mixing. $A_f^{(I)}$ is due to *CP* violation in interference and $A_f^{(\Delta)}$ is a non *CP* violating parameter.

Having summarised different types of *CP* violation and also how they manifest themselves in the experiment through time decay rate asymmetries, we summarise how the SM accommodates *CP* violation in its framework.

3.3 *CP* violation: the SM explanation

Consider the terms of the SM lagrangian which describe the interaction of fermions with the Higgs field doublet Φ, which has a vacuum expectation value of ν [20]

$$\mathcal{L} = -G^{(u)}\bar{q}_L \Phi u_R - G^{(d)}\bar{q}_L \epsilon \Phi^* d_R + h.c. = -G^{(u)}\nu\bar{u}_L u_R - G^{(d)}\nu\bar{d}_L d_R + h.c. \tag{3.37}$$

In Eq. 3.37, G are coupling constants, ϵ is the 2×2 antisymmetric tensor, q_L is a left handed quark doublet, $(u/d)_R$ are right handed quark singlets and the $q_{L,R}$ represent $q_{(i)L,R}$, where the subscript i represents a flavour index.

The up type (and the down type) quark fields represented by the $q_{(i)L,R}$ are the same at this stage, because they have the same electric charge and are all massless. Therefore, Eq. 3.37 represents couplings not only between the u and d quarks, but also between u and s, and u and b. This implies that the coupling constants $G^{(u,d)}$ are $n \times n$ matrices in flavour (family) space, where n=3 in the SM.

However, the terms containing the fields quadratically are interpreted as mass terms, and in the presence of coupling constants of the form $G^{(u,d)}$ in the mass terms, the down type quark field D which couples to a particular up type quark field U in the weak interaction terms like

$$J^{\mu}_{CC} = \bar{U}_{Li}\gamma^{\mu}D_{Li} \tag{3.38}$$

$$J^{\mu}_{NC} = \frac{1}{2}\left(\bar{U}_{Li}\gamma^{\mu}U_{Li} - \bar{D}_{Li}\gamma^{\mu}D_{Li}\right) - \sin^2\theta_W J^{\mu}_{(EM)} \tag{3.39}$$

$$J^{\mu}_{(EM)} = \frac{3}{2}\bar{U}_i\gamma^{\mu}U_i - \frac{1}{3}\bar{D}_i\gamma_{\mu}D_i \tag{3.40}$$

is not the same down type quark which couples in the mass terms. We choose to diagonalize the mass terms, and the $G^{(u,d)}$ can be made diagonal by multiplication with unitary matrices A and B such that

$$AGB^{\dagger} = D, \quad BG^{\dagger}A^{\dagger} = D \tag{3.41}$$

where D is a diagonal matrix.

We rotate the quark fields to the states of definite mass using unitary matrices S

$$U_{L,R}^{(m)} = S_{L,R}^{(U)} U_{L,R}, \quad D_{L,R}^{(m)} = S_{L,R}^{(D)} D_{L,R} \tag{3.42}$$

We now write Eq 3.37 in terms of the new quark fields

$$-\nu \bar{U}_L^{(m)} S_L^{(U)} G^{(U)} S_R^{(U)\dagger} U_R^{(m)} - \nu \bar{D}_L^{(m)} S_L^{(D)} G^{(D)} S_R^{(D)} U_R^{(m)\dagger} + h.c. \tag{3.43}$$

$$= m_u \bar{u}_L^{(m)} u_R^{(m)} + m_c \bar{c}_L^{(m)} c_R^{(m)} + ... \tag{3.44}$$

where the matrices S_L and S_R can be identified with A and B in Eq. 3.41.

This rotation of quark fields should not affect the neutral current terms (since S are unitary), but in the expression of charged current

$$J_{CC}^{\mu} = \bar{U}_{Li} \gamma^{\mu} D_{Li} = \bar{U}_L^{(m)} \gamma^{\mu} S_L^{(U)} S_L^{(D)\dagger} D_L^{(m)} \tag{3.45}$$

a unitary matrix appears, which measures the mismatch between the matrices that diagonalize the U and D quark masses

$$V \equiv S_L^{(U)} S_L^{(D)\dagger} \tag{3.46}$$

where V is the famous CKM matrix, named after Cabibbo, Kobayashi and Maskawa.

It is an extension of the idea of Cabibbo [21] who postulated that in a charged current interaction, the object to which the u quark couples is a linear combination of the d and s quarks. In other words, the physical d and s quark states are rotated with respect to the d and s states in flavour space, characterized by the Cabibbo angle θ_C. This leads to

a 2×2 unitary mixing matrix

$$\begin{pmatrix} d' \\ s' \end{pmatrix} = \begin{pmatrix} \cos\theta_C & \sin\theta_C \\ -\sin\theta_C & \cos\theta_C \end{pmatrix} \begin{pmatrix} d \\ s \end{pmatrix} \tag{3.47}$$

which rotates the flavour eigen states d and s into the mass eigen states d' and s'. The "mixing" matrix in this two generation case has only one free parameter, θ_C, which is real. In the absence of a complex parameter, it is not possible to generate *CP* violation. However, in the case of three generations, the mixing matrix is 3×3, and has $3^2 = 9$ free parameters. Five of the parameters can be absorbed in a redefinition of the quark fields and the remaining parameters are the three mixing angles and one (complex) weak phase. This phase is the only source of *CP* violation in the SM.

3.3.1 The CKM matrix and Unitarity triangle

The CKM matrix can be parametrized in many ways but the most widely used choice is of the Wolfenstein parametrization [22] as shown below (only to $\mathcal{O}(\lambda^4)$)

$$V_{CKM} = \begin{pmatrix} V_{ud} & V_{us} & V_{ub} \\ V_{cd} & V_{cs} & V_{cb} \\ V_{td} & V_{ts} & V_{tb} \end{pmatrix}$$

$$\sim \begin{pmatrix} 1-\lambda^2/2 & \lambda & A\lambda^3(\rho - i\eta + i\eta\lambda^2/2) \\ -\lambda & 1-\lambda^2/2 - i\eta A^2\lambda^4 & A\lambda^2(1+i\eta\lambda^2) \\ A\lambda^3(1-\rho-i\eta) & -A\lambda^2 & 1 \end{pmatrix} \tag{3.48}$$

The four parameters of the CKM matrix are free parameters in the SM and have been determined experimentally to be $\lambda \simeq 0.22$, A$\simeq 0.81$, $\rho \simeq 0.14$ and $\eta \simeq 0.35$ [23].

The hierarchical structure of the CKM matrix can be seen in the Wolfenstein parametrization, i.e. that quarks prefer to couple to the oppositely charged quark from the same family, as the diagonal terms are of order 1. On the other hand, the off diagonal terms are of order λ between the first and second generation, of order λ^2 between second and third generations and of order λ^3 between first and third generations.

The unitarity requirement on the CKM matrix can be written as

$$\begin{aligned} \sum_{\alpha=d,s,b} V_{i\alpha} V_{j\alpha}^* &= 0, \quad (\mathrm{i} < \mathrm{j}) \\ \sum_{i=u,c,t} V_{i\alpha} V_{i\beta}^* &= 0, \quad (\alpha < \beta) \end{aligned} \tag{3.49}$$

which gives six relations which can be visualized in the form of triangles in the complex plane, as shown in Fig. 3.1.

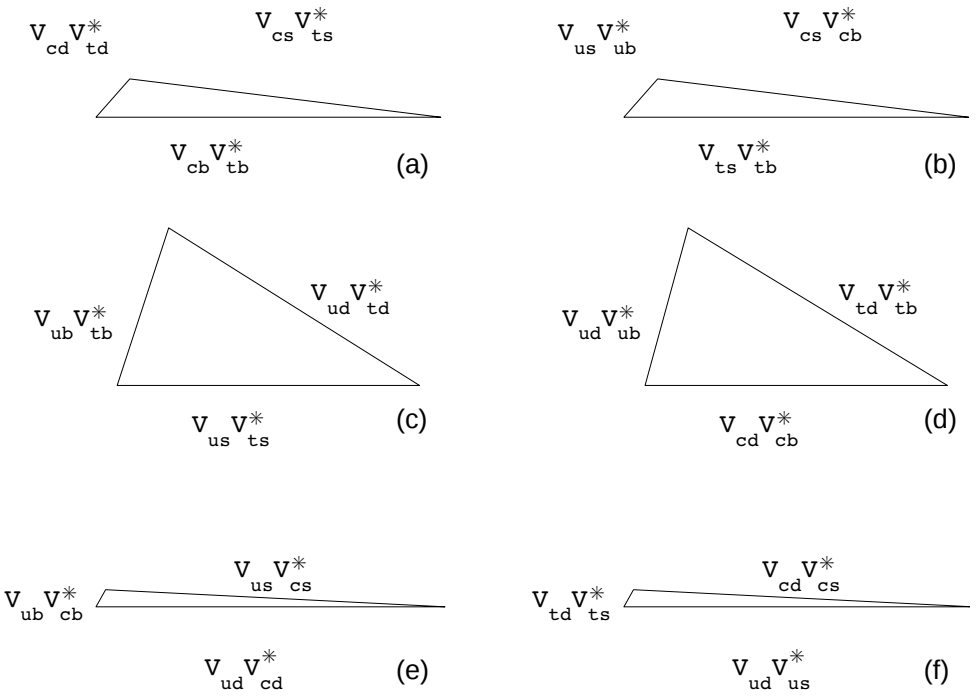

Figure 3.1: CKM triangles from the unitarity conditions in Eq. 3.49.

The sides of the triangles concerning $b \to d$ transitions (Fig. 3.1 *d*) represents the relation $V_{ud}V_{ub}^* + V_{cd}V_{cb}^* + V_{td}V_{tb}^* = 0$ and is usually called "*the*" unitarity triangle. It is usually represented as in Fig. 3.2, so that its vertices lie at (0,0), (0,1) and $(\bar{\rho}, \bar{\eta})$, where $\bar{\rho}$ and $\bar{\eta}$ are defined as $\bar{\rho} \equiv \rho(1 - \frac{\lambda^2}{2})$ and $\bar{\eta} \equiv \eta(1 - \frac{\lambda^2}{2})$. The angles of this triangle are given special names which are defined in Eq. 3.50.

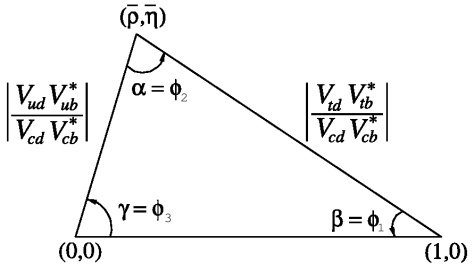

Figure 3.2: A sketch of the Unitarity triangle

$$\begin{aligned} \alpha \equiv \phi_2 &\equiv arg\left[-\frac{V_{tb}^* V_{td}}{V_{ub}^* V_{ud}}\right] \\ \beta \equiv \phi_1 &\equiv arg\left[-\frac{V_{cb}^* V_{cd}}{V_{tb}^* V_{td}}\right] \\ \gamma \equiv \phi_3 &\equiv arg\left[-\frac{V_{ub}^* V_{ud}}{V_{cb}^* V_{cd}}\right] \end{aligned} \tag{3.50}$$

The relations between the angles α, β and γ, and the parameters $\bar{\rho}, \bar{\eta}$ are as follows [24]

$$\begin{aligned} \sin 2\alpha &= \frac{2\bar{\eta}\left(\bar{\eta}^2 - \bar{\rho}\left(1-\bar{\rho}\right)\right)}{\left(\bar{\eta}^2 + (1-\bar{\rho})^2\right)\left(\bar{\eta}^2 + \bar{\rho}^2\right)} \\ \sin 2\beta &= \frac{2\bar{\eta}\left(1-\bar{\rho}\right)}{\bar{\eta}^2 + (1-\bar{\rho})^2} \\ \tan\gamma &= \frac{\bar{\eta}}{\bar{\rho}} \end{aligned}$$

The aim of CKM measurements is to determine the apex $(\bar{\rho}, \bar{\eta})$ as precisely as possible. The motivation is to check the consistency of the CKM picture, which assumes unitarity and also the SM size of the phases, which may not hold in presence of NP. The current status of the measurements of the CKM triangle is summarised in Fig. 3.3, which includes all experimental constraints on the various quantities linked to this triangle.

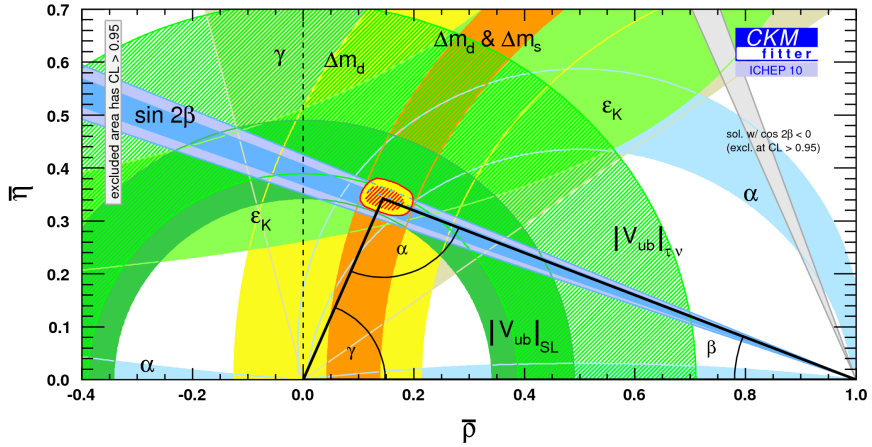

Figure 3.3: Constraints on the Unitarity triangle. Taken from [25]

Most of the sensitivity for the determination of the point $(\bar{\rho}, \bar{\eta})$ comes from loop processes, as can be seen by comparing this figure to Fig. 3.4, which shows the constraints coming from tree level measurements only.

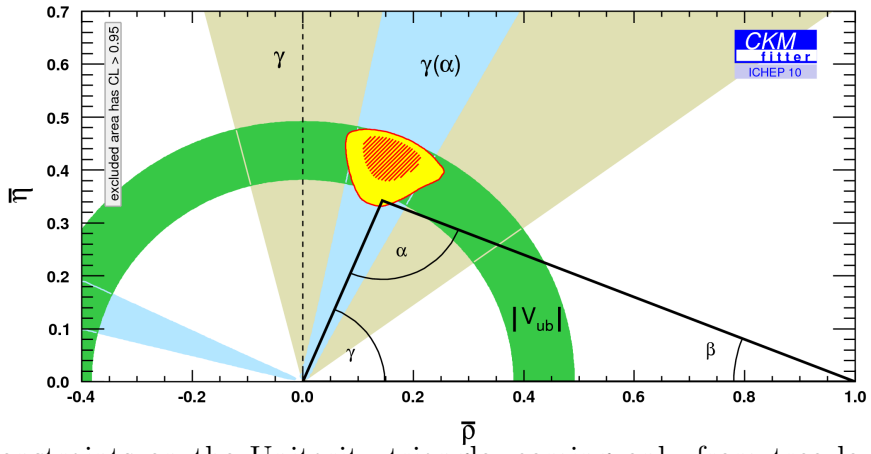

Figure 3.4: Constraints on the Unitarity triangle, coming only from tree level measurements. Taken from [25]

While the tree level processes are not expected to be affected by NP, loop processes are very sensitive to NP contribution. Therefore, it is useful to determine the CKM parameters with tree level processes and check for a differences with respect to their values determined in processes dominated by loops. In the following, we summarise the current status of the measurements of the sides and angles of the Unitarity triangle shown in Fig 3.2.

Measurement of $|V_{cb}|$

The parameter $|V_{cb}|$ can be measured from inclusive semileptonic $b \to cl\nu$ or exclusive $B \to D^{(*)}l\nu$ decays [26, 27]. The inclusive semileptonic decay rate can be parametrized, in the Operator Product Expansion (OPE) framework using the Heavy Quark Effective Theory (HQET), in terms of $|V_{cb}|$, m_b and matrix elements of the decay. The latter cannot be treated using perturbative calculations, and this, coupled with the uncertainty on the quark mass m_b, results in sizeable uncertainties on the extraction of $|V_{cb}|$. Also, experimentally, a cut has to be made on the lepton momentum and the measurement has to then be extrapolated in the whole region which involves theoretical assumptions. The current best fit values for $|V_{cb}|$, using all available measurements (CLEO and B factories) and employing two different schemes to treat m_b are reported in [28] and are consistent with each other.

For the $|V_{cb}|$ measurement in exclusive decays, the uncertainties are mainly due to poor knowledge of the form factors of the decays but there are subtle differences in the theoretical issues for $B \to Dl\nu$ and $B \to D^*l\nu$. Experimentally, the former decay is more challenging to isolate from background and while $B \to D^*l\nu$ can be isolated with good purity, it suffers from low efficiency due to the slow charged pion from the D^*. The $|V_{cb}|$ measurement from $B \to Dl\nu$ has twice the experimental uncertainty as the one from $B \to D^*l\nu$, while the theoretical uncertainties are similar for these channels. The world averages of the $|V_{cb}|$ measurements in these exclusive channels are reported in [28] and are consistent with each other. However, they are not in agreement with values obtained from inclusive measurements, which tend to be higher than the exclusive determinations. The discrepancy is at the level of 2σ, and the errors on the measurements in both cases are dominated by theoretical uncertainties and difficult to improve [28].

The theoretical uncertainties on $|V_{cb}|$ are different for inclusive and exclusive measure-

ments, a combination of both measurements with scaled errors is quoted by the PDG [29]

$$|V_{cb}| = (40.6 \pm 1.3) \times 10^{-3} \tag{3.51}$$

Measurement of $|V_{ub}|$

The first evidence of a non zero $|V_{ub}|$ comes from the end point of the lepton spectrum where $b \to cl\bar{\nu}$ events are not kinematically allowed due to the c quark mass [30, 31]. But there are theoretical uncertainties in the extrapolation of $|V_{ub}|$ to the entire range of the lepton spectrum. It has been pointed out that near the end point region of the phase space, the OPE framework does not work very well and so a lot of effort has been put into finding a phase space region where the charm backgrounds can be suppressed and the theoretical errors are controllable [28].

Experimentally, this measurement is more difficult than $|V_{cb}|$ because the charmless semileptonic decay width is about 1% of the total semileptonice width. So a big experimental challenge is the suppression of the large background.

The world average values (using CLEO and B factory results) are reported in [28] which also reports the exclusive measurement of $|V_{ub}|$ in $B \to \pi l\bar{\nu}$ and $B \to \rho l\bar{\nu}$. The error on exclusive measurements is dominated by the theoretical prediction of the hadronic form factor of the decays. However, similar to the situation in $|V_{cb}|$, the inclusive $|V_{ub}|$ measurements result in values that are significantly larger than the exclusive ones, and the discrepancy is more severe than in the case of $|V_{cb}|$ [28]. A combined value from inclusive and exclusive measurements is quoted by the PDG [29] as

$$|V_{ub}| = (3.89 \pm 0.44) \times 10^{-3} \tag{3.52}$$

Measurement of $|V_{tb}|$

$|V_{tb}|$ can be measured by the ratio of t quark decays to b quarks and sum of all t decays, assuming unitarity. The CDF and D0 measurements are $|V_{tb}| > 0.78$ and $|V_{tb}| > 0.89$ at 95% CL [29]. The most precise measurement of $|V_{tb}|$ (without assuming unitarity) comes from the single top production cross section, averaging the results from D0 and CDF, the PDG [29] quote

$$|V_{tb}| = 0.88 \pm 0.07 \tag{3.53}$$

Measurement of $|V_{td}|$

$|V_{td}|$ can be measured in the B_d meson oscillations, as the oscillation probability $x_d \equiv \frac{\Delta m}{\Gamma}$ can be related to $|V_{tb}^* V_{td}|^2$. The measurement from this method, assuming $|V_{tb}|$ =1 [32], results in a value of

$$|V_{td}| = (8.4 \pm 0.6) \times 10^{-3} \tag{3.54}$$

The dominant uncertainty is due to the theoretical calculation of the Bag parameter (B_B) and the decay constant (f_B) [29]. Much of this uncertainty is reduced in the ratio $\frac{|V_{td}|}{|V_{ts}|}$ which is proportional to ratio of $\frac{f_{B_d}\sqrt{B_{B_d}}}{f_{B_s}\sqrt{B_{B_s}}}$. The current value as quoted by PDG [29] is given in Eq. 3.55.

$$\frac{|V_{td}|}{|V_{ts}|} = 0.211 \pm 0.001 \pm 0.005 \tag{3.55}$$

$$\frac{|V_{td}|}{|V_{ts}|} = 0.2 \pm 0.04 \tag{3.56}$$

The ratio of the rates of $B \to \rho\gamma$ and $B \to K^*\gamma$ is also sensitive to $\frac{|V_{td}|}{|V_{ts}|}$. However, there is uncertainty from the theoretical input of the form factors and the assumption of

isospin symmetry. The determination of $\frac{|V_{td}|}{|V_{ts}|}$ using this method is given in Eq. 3.56 [29]. A theoretically clean measurement of $V_{td}^* V_{ts}$ can be made in $K^+ \to \pi^+ \nu\bar{\nu}$ to improve these errors, however, this measurement is presently limited by low statistics [33, 34].

Measurement of $|V_{ud}|$

This parameter has been measured quite precisely from nuclear beta decays. The measurement of the half life the Q value of the decay, and a calculation of radiative and isospin violating effects are combined to determine $|V_{ud}|$. The average, as quoted by PDG [29] is given in Eq. 3.57.

$$|V_{ud}| = 0.97425 \pm 0.00022 \tag{3.57}$$

$$|V_{ud}| = 0.9728 \pm 0.0030 \tag{3.58}$$

The accuracy is limited by the knowledge of nuclear Coulomb distortions and radiative corrections. The measurement of $|V_{ud}|$ in $\pi^+ \to \pi^0 e^+ \nu$ by the PIBETA experiment [29] yields the value given in Eq. 3.58, which is compatible with the result from nuclear beta decay.

Measurement of $|V_{cd}|$

$|V_{cd}|$ is measured in the semileptonic decays of D mesons, where the accuracy is limited by the theoretical predictions for the form factors. The average of CLEO-c and Belle measurements of $D \to \pi l \nu$, as quoted by PDG [29] is given in Eq. 3.59, where the first uncertainty is experimental and the second is due to the form factor calculations.

$$|V_{cd}| = 0.229 \pm 0.006 \pm 0.024 \tag{3.59}$$

$$|V_{cd}| = 0.230 \pm 0.011 \tag{3.60}$$

A more precise determination of $|V_{cd}|$ can be made in the production of charm in neutrino nucleon interactions (see for example [35]). The measurement is sensitive to $|V_{cd}|^2$ times the average semileptonic branching ratio of charm quarks, denoted by $\mathcal{B}_\mu$ in literature, which is also measured. The determination of $|V_{cd}|$ using this method is given in Eq. 3.60.

Measurement of $|V_{us}|$, $|V_{cs}|$ and $|V_{ts}|$ [32]

- The average value of $|V_{us}|$ measured in the decays of $K_L \to \pi e\nu$, $K_L \to \pi\mu\nu$, $K^\pm \to \pi^0 e^\pm \nu$ and $K_S \to \pi e\nu$ is $|V_{us}| = 0.2246 \pm 0.0012$, where the form factor for each decay has to be theoretically calculated.

  Another way to measure this parameter is in the ratio of the branching ratios of $K^+ \to \mu^+\nu(\gamma)$ and $\pi^+ \to \mu^+\nu(\gamma)$, which is proportional to $|V_{us}|/|V_{ud}|$ times the ratio of the decay constants f_K/f_π. The latter has to be provided by theory while $|V_{ud}|$ is measured to per mille precision in nuclear beta decays. This method yields $|V_{us}| = 0.2259 \pm 0.0014$, and the average of these results is

$$|V_{us}| = 0.2252 \pm 0.0009$$

- $|V_{cs}|$ can be measured with flavour tagged decays of $W^+ \to c\bar{s}$ but this measurement from LEP has a large statistical uncertainty. $|V_{cs}|$ can also be measured in the semileptonic D and leptonic D_s decays. These measurements need the theoretical input of the semileptonic D form factor and the D_s decay constant respectively, and the result from the semileptonic D decays has a larger theoretical uncertainty. The average from the two methods is

$$|V_{cs}| = 1.023 \pm 0.036$$

- Similar to the case of $|V_{td}|$, $|V_{ts}|$ can be related to the oscillation probability of the B_s meson. Using the Δm_s measurement by CDF, the PDG quote

$$|V_{ts}| = (38.7 \pm 2.1) \times 10^{-3}$$

Measurement of β

This is the most well measured of the three angles of the Unitarity triangle. The current best value, as quoted by the UTFit [36] is

$$\beta = (22.0 \pm 0.8)^\circ \tag{3.61}$$

where the measurement of β in $b \to c\bar{c}s$ transitions, done by the B factories, LEP experiments and CDF have been averaged. The accuracy is by far dominated by the B factory measurements.

At the B factories, this angle is measured in the time dependent decay rate asymmetry in $B_d \to J/\psi K^0$ decays [37]. The formulae for the time dependent decay rate in the case where the final state is accessible to both B and $\bar{B}$ mesons were given in Eq. 3.33. The definitions of the parameters $\left[A_f^{(MD)}\right]$ and $\left[A_f^{(I)}\right]$ from Eq. 3.34 and λ_f from Eq. 3.15 are

$$A_f^{(MD)} = \frac{1-|\lambda_f|^2}{1+|\lambda_f|^2}, \quad A_f^{(I)} = \frac{2Im(\lambda_f)}{1+|\lambda_f|^2}, \quad \lambda_f = \frac{q}{p}\frac{\bar{A}_f}{A_f}$$

As mentioned earlier, $\left[A_f^{(MD)}\right]$ parametrizes CP violation in mixing and $\left[A_f^{(I)}\right]$ parametrizes CP violation in interference. The former is measured to be very close to zero, in the semileptonic asymmetry in B decays [38], hence then $[A_f^{(I)}] = Im(\lambda_f)$. The phase of λ_f is the

phase of q/p

$$\frac{q}{p} = \frac{(V_{tb}^* V_{td})^2}{|V_{tb}^* V_{td}|^2} = e^{i2\beta}, \quad \text{and} \quad Im\frac{q}{p} = \sin 2\beta \tag{3.62}$$

The phase from the decay part $\frac{\bar{A}}{A}$ is $\frac{(V_{cb}^* V_{cs})^2}{|V_{cb}^* V_{cs}|^2}$ is real to order λ^4, so the time dependent decay rate asymmetry in $B_d \to J/\psi K$ is a measure of $\sin 2\beta$.

Measurement of α

This angle can be measured in decays of the type $B \to h^+h^-$ (where h is a π or ρ). The phase from $\frac{\bar{A}}{A}$ is $\frac{(V_{ud}^* V_{ub})^2}{|V_{ud}^* V_{ub}|^2} = e^{-i2\gamma}$, and assuming there is only one decay amplitude, the time dependent asymmetry measures the angle α, as

$$Im\,\lambda = Im\,(e^{-i2\beta}e^{-i2\gamma}) = Im\,e^{i2\alpha} = \sin(2\alpha) \tag{3.63}$$

But there is another amplitude in $B \to h^+h^-$ due to a gluonic penguin diagram, which spoils the above assumption. In presence of the penguin contribution, an isospin analysis of $B \to \pi^+\pi^-$, $B \to \pi^0\pi^0$ and $B^+ \to \pi^+\pi^0$, along with their branching ratios, can be used to extract α [39]. The B factories have performed isospin analyses of the $\pi\pi$ and $\rho\rho$ states, and Dalitz plot analyses of $\pi^+\pi^-\pi^0$ in $B \to \rho\pi$ decays. The value of α quoted by the UTFit [36] group is

$$\alpha = (92.0 \pm 3.4)^\circ$$

Measurement of γ

This angle can be measured by a time integrated analysis in $B^- \to DK^-$ and $\bar{B}_d \to D\bar{K}^{*0}$ where the D represents a D^0 or $\bar{D}^0$ decaying to a common final state. The diagram for $B^- \to \bar{D}K^-$ is colour and CKM suppressed with respect to the $B^- \to DK^-$ diagram, the weak phase difference between them being γ and the strong phase difference is δ. Their

amplitudes interfere if the D mesons decay to a common final state. In this method, the ratio between the allowed and suppressed amplitudes r_B and the parameter δ have to be extracted from data, along with γ. The sensitivity on the latter depends on the value of r_B. The mixing and CP violation in $D^0\bar{D}^0$ is neglected here, the former estimated to have $< 1^\circ$ effect on γ (Chapter 2 of [40]).

The diagrams for $\bar{B}_d \to D\bar{K}^{*0}$ and $\bar{B}_d \to \bar{D}\bar{K}^{*0}$ are both colour suppressed, so the sensitivity to γ is increased, but their Branching ratios are comparatively small. Also, the parameters r_{B^0} and δ_{B^0} have to be measured separately in this analysis.

There are two methods to extract γ from time integrated measurements of two body D decays in the above mentioned B decays. In the one called the GLW method (after its authors Gronau, London, Wyler) [41, 42], the D mesons are reconstructed in CP eigenstates like $\pi^+\pi^-$ or K^+K^-. In the ADS method (Atwood, Dunietz, Soni) [43], the D mesons are reconstructed in their flavour specific final states like $K^+\pi^-$, which is Cabibbo suppressed for the D^0 meson but $K^-\pi^+$ is favoured. Other flavour specific multibody final states of the D mesons can also be explored, but require a Dalitz plot analysis. A Dalitz plot analysis of $B^\pm \to D(\to K_s\pi^+\pi^-)K^\pm$ also provides sensitivity to γ which is due to the difference in the Dalitz plot of the D coming from B^+ or B^-.

Another way to measure γ is offered by the time dependent asymmetries in $B_d \to D^{*\pm}\pi^\mp$. These asymmetries allow one to measure $\gamma + 2\beta$, and β is measured to a precision of $< 1^\circ$ already. Time dependent asymmetries in $B_s \to D_s^{*\pm}K^\mp$ allow $\gamma - 2\phi_M$ to be measured, where $2\phi_M$ is the B_s mixing phase which will be constrained in $B_s \to J/\psi\phi$ decays. The analysis in B_s decays is likely to be unique to LHCb (Chapter 2 of [40]) and will eventually provide the best sensitivity on γ once a sufficiently large data sample has been collected [44].

The average value of γ by combining the GLW, ADS and Dalitz analyses, is quoted by the PDG [29] to be

$$\gamma = (73^{+22}_{-25})^\circ \tag{3.64}$$

Most of the external constraints on γ are from loop processes so there is much effort to make tree level measurements of γ with enough precision to determine if direct γ measurement from tree level is compatible with the value given by constraints from loop processes.

The time dependent *CP* asymmetries in $B_d \to \pi^+\pi^-$ and $B_s \to K^+K^-$, which have sizeable penguin contributions in their amplitudes, can also be used to measure γ as pointed out in [45, 46]. An assumption about the invariance of strong interaction dynamics under an exchange of s and d quarks, or the U spin symmetry, has to be made. The B factories have made a measurement of the time dependent *CP* asymmetry in $B_d \to \pi\pi$ [47, 48], there is some disagreement between the BELLE and *BABAR* results [40], while the Tevatron experiments have not made any time dependent measurement. LHCb has access to both the B_d and B_s system, and the sensitivity on γ for this time dependent analysis is estimated to be 10%, for $2\,\text{fb}^{-1}$ of luminosity (Chapter 3 of [40]).

3.3.2 Summary and Future prospects

The current status of the measurements of the CKM triangle is summarised in Fig. 3.3. The determination of the sides of the triangle, especially of the elements $|V_{ub}|$, $|V_{cb}|$ and $|V_{td}|$ (and $|V_{ts}|$) is limited by theoretical uncertainties, while its angles, especially γ, are limited by experimental accuracy.

The angles β and γ can be further constrained by comparing the former angle to the side proportional to $\frac{|V_{ub}|}{|V_{cb}|}$ and the latter angle to the side proportional to $\frac{|V_{td}|}{|V_{ts}|}$. Unfortunately, these are not stringent constraints because of the large error on $|V_{ub}|$ and γ. LHCb can improve the error on the latter by a factor of 2 with only 500 pb^{-1} [40]. The current LHC plan is to provide an integrated luminosity of $1\,\text{fb}^{-1}$ to LHCb during the physics run starting in 2011.

The measurement of the angle β_s, the angle of the "bs" triangle (Fig. 3.1 b) equivalent to the β of "bd" triangle discussed earlier, is also one of the key LHCb measurements. It has quite a precise prediction in the SM $(3.6 \pm 0.2) \times 10^{-2}$ rad, and LHCb sensitivity for $2\,\text{fb}^{-1}$ is estimated to be ~ 0.03 (Chapter 4 of [40]).

While the measurement of CKM phases is an excellent way to probe and constrain New Physics, another powerful test is of the helicity structure of New Physics. This thesis is devoted to the measurement of the photon polarization in the decay $B_s \to \phi\gamma$ at LHCb. In the following chapter we motivate this measurement and explore the LHCb prospects.

Chapter 4

Probing the helicity structure of New Physics

4.1 Introduction

Flavour changing neutral current transitions are not allowed at tree level in the SM. They occur only via loop decays which offer the possibility to look for contributions from NP particles, which can enter the loop. An example is a $b \to s$ transition, shown in Fig. 4.1.

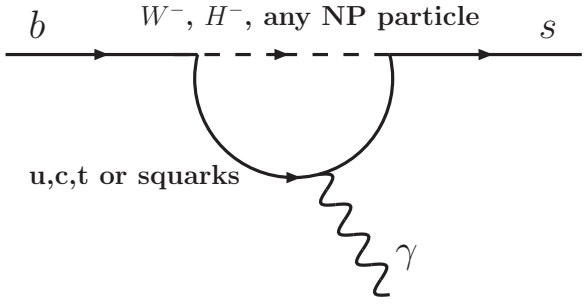

Figure 4.1: The loop diagram for a $b \to s\gamma$ transition

For loop decays, the decay rates, decay rate asymmetries and angular distributions and polarizations of the final state particles can be predicted in the SM. These observables can be changed significantly by the presence of NP, making these decays sensitive probes of NP [49, 50, 51]. Also, the current measurements from these decays can be used to constrain NP models. For example Ref [52] reports on the constraints and possible exclusion of the parameter space of a certain NP scenario, as a function of $b \to s\gamma$ and other rare decay rates.

We will concentrate on $b \to s$ transitions in particular, and introduce Operator product expansion (OPE) here, which is a useful tool to study these decays. The details of this framework which can be seen in Ref. [53, 54, 55]. It is sufficient to note here that in the OPE framework, the 'effective' Hamiltonian for a given process can be parametrized as the sum of the products of Wilson coefficients C and Operators Q as

$$\mathcal{H}_{eff} = \sum_{K=1}^{10} C_K Q_K \tag{4.1}$$

where the operators encode the contributions due to particles at or below the energy scale (mass) of the decaying particles, while the Wilson coefficients encode the contributions due to particles much heavier than the decaying particles.

The first order diagrams contributing to $b \to s(\gamma, g, ll)$ are shown in Fig. 4.2, where (a) represents operators $Q_{7\gamma}$ and Q_{7g} for the cases where a photon or gluon is emitted from the t quark, respectively. The operators represented by Fig. 4.2 (b) are called Q_{9V} and Q_{10A} for the cases where the final state leptons are in vector and axial state respectively. The operator $Q_{7\gamma}$ is the most dominant one for $b \to s\gamma$ decays while for $b \to sll$ decays, Q_{9A}, Q_{10A} and $Q_{7\gamma}$ are dominant [56].

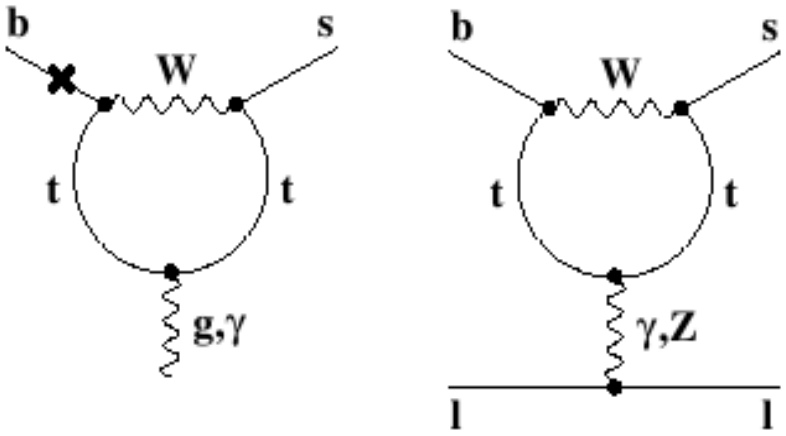

(a) (b)

Figure 4.2: First order diagrams contributing to $b \rightarrow (\gamma, g, ll)$ quark decays (Figure from [54]).

The decay rates of loop processes are sensitive to Wilson coefficients, e.g. $b \rightarrow s\gamma$ is sensitive to $C_{7\gamma}$ while the rate of $b \rightarrow sll$ is sensitive not only to the magnitude but also to the sign of C_7, C_9 and C_{10} [57]. Although the measured branching ratios of these decays are compatible with the SM prediction, the structure and composition of operators involved in these decays is still open to experimental test.

To test the structure and composition of operators involved in a decay, different observables can be constructed which have different distributions in SM and various NP scenarios. An example of such an observable is the Forward backward asymmetry (A_{FB}) in $b \rightarrow sll$, usually measured in $B_d \rightarrow K^*\mu\mu$. This is defined as the asymmetry in the number of positively and negatively charged leptons travelling in the same direction as the K^* in the dilepton rest frame. The shape of this asymmetry, as a function of the square of the invariant mass of the lepton pair in the final state (denoted by q^2 or s in some literature), is shown in Fig. 4.3. This figure shows a comparison between the SM prediction and various NP scenarios where the signs of one or more Wilson coefficients have been inverted, i.e. $C_7 = -C_7^{SM}$, $C_9 = -C_9^{SM}$ or $C_{10} = -C_{10}^{SM}$.

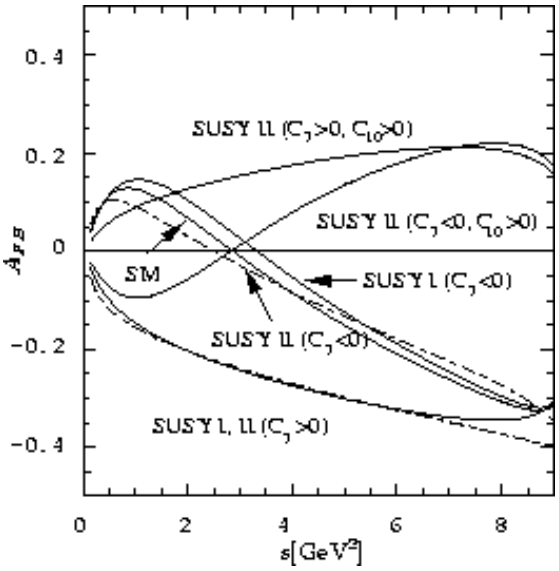

Figure 4.3: Forward backward asymmetry in $B_d \to K^* \mu\mu$, in the SM and some SUSY scenarios (Figure from [56]).

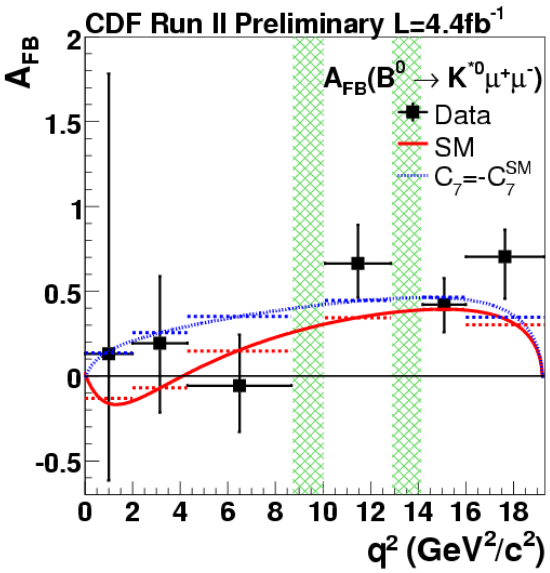

Figure 4.4: Measurement of A_{FB} by the CDF experiment [58] (Figure from [59]).

Also noticeable in the figure is the zero crossing point of the asymmetry, which is the point along q^2 where the asymmetry flips sign. This point is accurately predicted in the SM [56] and is proportional to the ratio of the coefficients C_7 and C_9. Some NP scenarios can have different or no zero crossing points for the A_{FB}, as shown in Fig. 4.3.

The A_{FB} measurements by CDF and the B factories are shown in Fig. 4.4 and 4.5 respectively. There is indication of a discrepancy between the SM prediction and the measurements of A_{FB} at low q^2, but the measurements are statistically limited. LHCb can achieve a precision on A_{FB} comparable to the B factory measurements with a 300 pb^{-1} data sample, which LHCb is set to collect relatively soon. A statistical precision of $\pm 0.5\,\text{GeV}^2$ on the zero crossing point can be achieved with 2 fb^{-1} (Chapter 6 of [40]).

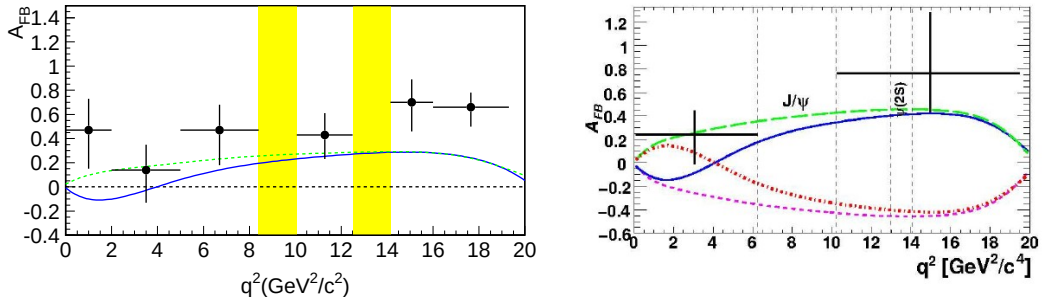

(a) (b)

Figure 4.5: The measurements of A_{FB} in $B_d \to K^*\mu\mu$ by *Belle* (a) and *BABAR* (b). Solid curves in both figures represnt the SM prediction while the dotted ones represent different scenario where the signs of one or a combination of the Wilson coefficients C_7, C_9 and C_{10} have been inverted (Figures from [60, 61]).

4.1.1 Low q^2 region and photon polarization

The low q^2 region of $b \to sll$ is of special interest, as it is almost entirely dominated by the photon penguin in Fig. 4.2 (b), while the high q^2 region is dominated by the Z penguin. The other photon penguin operator is Fig. 4.2 (a).

Due to the helicity structure of the W bosons, the real or virtual photon in $b \to s(\gamma, ll)$ is predicted to be almost entirely left handed in the SM, with very small corrections of the order of $\frac{m_s}{m_b}$ [49]. This is because helicity is not a conserved quantity for massive particles like the s and b quarks. The SM prediction for the "wrong" helicity photons from a b (or a $\bar{b}$) quark decay is of the order of a percent [49]. It has later been noted that gluonic contributions to the penguin loop can also give up to a 1% effect [50]. The presence of NP can change the composition of the right and left handed currents in the decay, as is predicted by many NP models [49, 54, 56]. Hence, the measurement of the polarization of the photon is a very useful null test of the SM.

The low q^2 region in $b \to sll$ can also be probed with an angular analysis of the final

state particles in $B_d \to K^* e^+ e^-$. At LHCb, the sensitivity on the ratio of right to left handed component is about 0.1 for an integrated luminosity of $2\,\text{fb}^{-1}$ [62].

In case of a real final state photon in a $b \to s\gamma$ decay (Fig. 4.2 a), the polarization of the photon can be determined using decays where the B decays to a photon and a CP eigenstate, i.e. $B \to f_{CP}\gamma$. Due to the presence of interference in mixing and decay, both flavours of the B meson in $B \to f_{CP}\gamma$ can decay to both left and right handed final states of the photon, but one final state of the photon is suppressed for a certain flavour of B. A time dependent analysis of the decay rate of the B and $\overline{B}$ mesons in $B \to f_{CP}\gamma$ gives access to the polarization of the photon in the final state. The work done in this thesis is concerned with making this measurement at LHCb, with the decay $B_s \to \phi\gamma$. In the following we introduce the terms in the decay rate of $B_s \to \phi\gamma$ which provide access to the "wrong" helicity photon from a $\bar{B}$ or a B decay.

4.1.2 $B \to f_{CP}\gamma$ decay rate and photon polarization

We write the expression for the time dependent decay rate of a B meson (Eq. 3.33)

$$\Gamma\left[B(t) \to f\right] \propto \frac{1}{2}|A_f|^2(1+|\lambda_f|^2)e^{-\bar{\Gamma}t}\big[\cosh(\Delta\Gamma t/2) + A_f^{(\Delta)}\sinh(\Delta\Gamma t/2) + A_f^{(MD)}\cos(\Delta m t) - A_f^{(I)}\sin(\Delta m t)\big] \tag{4.2}$$

$$\Gamma\left[\bar{B}(t) \to f\right] \propto \frac{1}{2}|A_f|^2\left|\frac{p}{q}\right|^2(1+|\lambda_f|^2)e^{-\bar{\Gamma}t}\big[\cosh(\Delta\Gamma t/2) + A_f^{(\Delta)}\sinh(\Delta\Gamma t/2) - A_f^{(MD)}\cos(\Delta m t) + A_f^{(I)}\sin(\Delta m t)\big] \tag{4.3}$$

We now change the notation and represent $A_f^{(MD)}$ with $\mathcal{C}$, $A_f^{(I)}$ with $\mathcal{S}$ and $A_f^{(\Delta)}$ with $-\mathcal{A}^{\Delta}$, as these definitions are frequently used in literature, and also later in this thesis. The quantities are defined as (Eq. 3.34)

$$A_f^{(MD)} = \mathcal{C} = \frac{1-|\lambda_f|^2}{1+|\lambda_f|^2}, \quad A_f^{(I)} = \mathcal{S} = \frac{2Im(\lambda_f)}{1+|\lambda_f|^2}, \quad A_f^{(\Delta)} = -\mathcal{A}^{\Delta} = \frac{2Re(\lambda_f)}{1+|\lambda_f|^2} \tag{4.4}$$

where λ_f is defined as $\lambda_f = (q/p)\,(\bar{A}_f/A_f)$.

We define the amplitudes $A_{L(R)}$ for the emission of left handed and right handed photons in a $\bar{B}$ decay as

$$A_{L,R} \equiv A(B \to f_{CP}\gamma_{L,R}), \quad \bar{A}_{L,R} \equiv A(\bar{B} \to f_{CP}\gamma_{L,R}) \tag{4.5}$$

For B mesons, CP violation in mixing can be neglected, since all the measurements to date point to an extremely small if any mixing induced CP violation in B system [38]. Hence we assume $|q/p| = 1$, and use the above definitions to write $\mathcal{C}$, $\mathcal{S}$ and $\mathcal{A}^{\Delta}$ [63]

$$\mathcal{C} = \frac{(|A_L|^2 + |A_R|^2) - (|\bar{A}_L|^2 + |\bar{A}_R|^2)}{|A_L|^2 + |A_R|^2 + |\bar{A}_L|^2 + |\bar{A}_R|^2} \tag{4.6}$$

$$\mathcal{S} = \frac{2Im\left[\frac{q}{p}\left(\bar{A}_L A_L^* + \bar{A}_R A_R^*\right)\right]}{|A_L|^2 + |A_R|^2 + |\bar{A}_L|^2 + |\bar{A}_R|^2} \tag{4.7}$$

$$\mathcal{A}^{\Delta} = \frac{2Re\left[\frac{q}{p}\left(\bar{A}_L A_L^* + \bar{A}_R A_R^*\right)\right]}{|A_L|^2 + |A_R|^2 + |\bar{A}_L|^2 + |\bar{A}_R|^2} \tag{4.8}$$

The parameters $\mathcal{S}$ and $\mathcal{A}^{\Delta}$ can also be expressed as

$$\mathcal{S} = \sin(2\psi)\sin\phi, \qquad \mathcal{A}^{\Delta} = \sin(2\psi)\cos\phi \tag{4.9}$$

where ϕ is the B mixing phase (depending on the meson, $\phi_d(2\beta)$ or ϕ_s). The parameter ψ contains the information on the fraction of photons with the "wrong" polarization in the decay of a $\bar{B}$ (or B) as:

$$\tan\psi = \frac{\bar{B} \to f^{CP}\gamma_R}{\bar{B} \to f^{CP}\gamma_L} \tag{4.10}$$

Therefore, the parameters $\mathcal{S}$ and $\mathcal{A}^{\Delta}$ can be used to probe NP, as they give access to the right handed contribution (parameter ψ) in $B \to f_{CP}\gamma$ decays. The parameter $\mathcal{C}$ is

sensitive to new weak phases rather than the right handed contribution in $B \to f_{CP}\gamma$ [63], and will not be discussed further.

4.1.3 Tagged and untagged analysis of $B \to f_{CP}\gamma$

We now rewrite the decay rate in terms of $\mathcal{C}$, $\mathcal{S}$ and $\mathcal{A}^{\Delta}$

$$\Gamma_B(t) \propto |A|^2 e^{\Gamma t}\left[\cosh(\Delta\Gamma t/2) - \mathcal{A}^{\Delta}\sinh(\Delta\Gamma t/2) \pm \mathcal{C}\cos(\Delta m t) \mp \mathcal{S}\sin(\Delta m t)\right] \quad (4.11)$$

where the last two terms are negative and positive respectively in case of a $\bar{B}$ (positive and negative respectively in case of a B), and the parameter $\mathcal{S}$ will appear in the *difference* between the B and $\bar{B}$ decay rates. Therefore, a measurement of $\mathcal{S}$ will require flavour tagging, i.e. the determination of the flavour of the meson that decayed through $B \to f_{CP}\gamma$.

The parameter $\mathcal{A}^{\Delta}$ appears in the sum of the two decay rates, and its measurement does not require any flavour tagging. This is a big experimental advantage as effective flavour tagging efficiencies tend to be less than 10% [40] and require very good understanding of various systematics. It is worth noting that sensitivity on $\mathcal{A}^{\Delta}$ is proportional to the size of $\Delta\Gamma$, so $\mathcal{A}^{\Delta}$ is accessible only in the B_s system [63].

The B factories have access to the B_d system only, and they measure the parameter $\mathcal{S}$ in the time dependent asymmetry of $B_d \to K^*(K_s\pi^0)\gamma$ decays. The measurements are statistically limited and the averaged results by the HFAG group [64] are:

$$\mathcal{S}_{K^*(K_s\pi^0)\gamma} = -0.19 \pm 0.23, \quad \mathcal{S}_{K_s\pi^0\gamma} = -0.09 \pm 0.24 \quad (4.12)$$

where the value on left is the determination of $\mathcal{S}$ using only resonant decays $K^* \to K_s\pi^0$, while on the right is using all $B_d \to K_s\pi^0\gamma$ decays. The current uncertainty on $\mathcal{S}$ translates

into $\sigma_{sin(2\psi)} = 0.33$, or an uncertainty of 0.16 on $\frac{A_R}{A_L}$, the ratio of the right to left handed components of the photon polarization (Eq. 4.9, 4.10). LHCb can reduce this uncertainty to $\sigma_{\frac{A_R}{A_L}} \sim 0.1$ with the untagged analysis of $B_s \to \phi\gamma$ decay, and to 0.05 with the tagged analysis, as listed in Table. 4.1.

Decay	Analysis	$\sigma_{\frac{A_R}{A_L}}$
$B_d \to K^*\gamma$	$\sigma_{\mathcal{S}} \sim 0.23$ (B factories)	~ 0.16
$B_s \to \phi\gamma$	Untagged, $\sigma_{\mathcal{A}^\Delta} \sim 0.2$ [40]	~ 0.1
$B_s \to \phi\gamma$	Tagged, $\sigma_{\mathcal{S}} \sim 0.1$ [40]	~ 0.05
$B_d \to K^*ee$	Angular distribution [62]	~ 0.1

Table 4.1: Sensitivity of LHCb analyses to the fraction of the right to left handed photons ($\frac{A_R}{A_L}$) in radiative B decays. These estimates are calculated for $2\,\text{fb}^{-1}$ of itnegrated luminosity, with a simulation at $\sqrt{s}$ =14 TeV.

The tagged and untagged analyses of $B_s \to \phi\gamma$ at LHCb are very complimentary to each other as $\mathcal{S}$ and $\mathcal{A}^\Delta$ appear with the *sine* and *cosine* of the mixing phase (ϕ_s in case of the B_s system) respectively. So, the sensitivity on the parameter ψ or $\frac{A_R}{A_L}$ (Eq. 4.10) by a measurement of $\mathcal{S}$ or $\mathcal{A}^\Delta$ depends on the value of ϕ_s.

In addition to that, $\mathcal{A}^\Delta$ appears with the *sinh* of $\Delta\Gamma_s$, hence the sensitivity on ψ with the untagged analysis depends on the value of $\Delta\Gamma_s$. The experimental measurement of $\Delta\Gamma_s$ currently has a 50% uncertainty, as $\Delta\Gamma_s = 0.062^{+0.034}_{-0.037}$ [29]. If, with more precise measurements, this parameter turns out to be larger, $\sigma_{\frac{A_R}{A_L}}$ for the untagged analysis can shrink further.

Measuring $\mathcal{A}^{\Delta}$ in $B_s \to \phi\gamma$

The decay rate for $B_s \to \phi\gamma$ where the B_s mesons are untagged, can be written as

$$\Gamma_{B_s}(t) \propto |A|^2 e^{-\Gamma_s t} \left[\cosh(\Delta\Gamma t/2) - \mathcal{A}^{\Delta} \sinh(\Delta\Gamma t/2)\right] \tag{4.13}$$

where, assuming that the partial rates of B_s and $\bar{B}_s$ are equal, the terms with $\mathcal{C}$ and $\mathcal{S}$ cancel in the addition of the two decay rates. In the limit of a small value of $\mathcal{A}^{\Delta}$, the above equation can be written as

$$\Gamma_{B_s}(t) \propto |A|^2 e^{-\Gamma_s t} \left[1 - \frac{\mathcal{A}^{\Delta}\Delta\Gamma t}{2} + \frac{1}{2}\left(\frac{\mathcal{A}^{\Delta}\Delta\Gamma t}{2}\right)^2 + ...\right] \approx |A|^2 e^{-\Gamma_{B_s\to\phi\gamma} t} \tag{4.14}$$

$$\text{where} \quad \Gamma_{B_s\to\phi\gamma} = \Gamma_s + \frac{\mathcal{A}^{\Delta}\Delta\Gamma}{2} \tag{4.15}$$

so the analysis for $\mathcal{A}^{\Delta}$ is actually a measurement of the *difference* in the B_s lifetime as measured in some other channel (and input in the above equation as Γ_s) and in $B_s \to \phi\gamma$.

LHCb plans to measure the lifetime precisely in $B_s \to J/\psi\phi$ to a precision of 3 fs, which will be a crucial input to this analysis. Also important is the value of $\Delta\Gamma$, the LHCb precision on it is estimated to be $\sim$9 fs for 2 fb^{-1} (Chapter 4 of [40]). LHCb results from $B_s \to J/\psi\phi$ have already been shown in Ref [65] and are predicted to become competitive with the world results with the 2011 data set.

The understanding of the reconstruction of the B_s proper time is also of prime importance to the analysis, as will be shown in the following section. In this section we report toy MC studies[1] to determine the sensitivity of the experiment on $\mathcal{A}^{\Delta}$ and also explore the impact of certain systematic effects on the experimental sensitivity on $\mathcal{A}^{\Delta}$.

[1] We use RooFit to perform all the toy MC studies described in this thesis.

4.2 Measuring $\mathcal{A}^{\Delta}$ at LHC*b*

4.2.1 Signal yield

At LHC*b*, the yield of $B_s \to \phi\gamma$ estimated to be about 11000 signal events for an integrated luminosity of $2\,\text{fb}^{-1}$ [40][2]. The mass resolution of the B_s in this decay mode is dominated by the electromagnetic calorimeter resolution, and is about 100 MeV. Fig. 4.6 shows the invariant mass distribution of selected and truth matched $B_s \to \phi\gamma$ candidates, from the full LHC*b* Monte Carlo simulation, and Fig. 4.7 shows their proper time distribution[3].

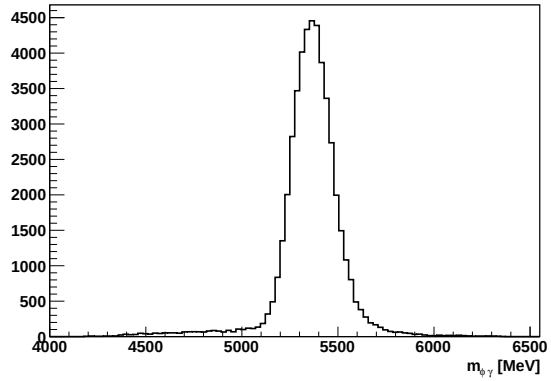

Figure 4.6: The invariant mass of the B_s reconstructed in $B_s \to \phi\gamma$ channel, using full LHC*b* MC events.

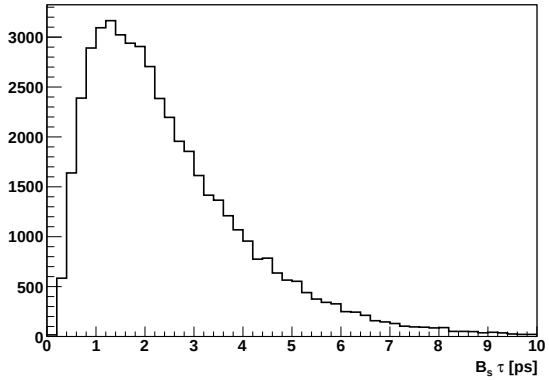

Figure 4.7: The reconstructed proper time of the B_s reconstructed in $B_s \to \phi\gamma$ channel, using full LHC*b* MC events.

4.2.2 Extraction of $\mathcal{A}^{\Delta}$

The proper time distribution *measured* by a detector (Fig. 4.7) is the product of the proper time distribution *generated* by nature multiplied by a selection efficiency (which is a function of proper time $\epsilon(t)$), convoluted with the proper time resolution of the detector. The proper time resolution and acceptance functions for the selected signal sample are plotted in Fig. 4.8. The resolution function has been parametrized with two Gaussians

[2]This estimate was made with a simulation at $\sqrt{s} = 14\,\text{TeV}$

[3]The selection criteria and Monte Carlo sample will be discussed in detail in Chapters 7 and 8.

and the acceptance has been parametrized by as

$$\epsilon(t) = \frac{(at)^c}{1 + (at)^c} \tag{4.16}$$

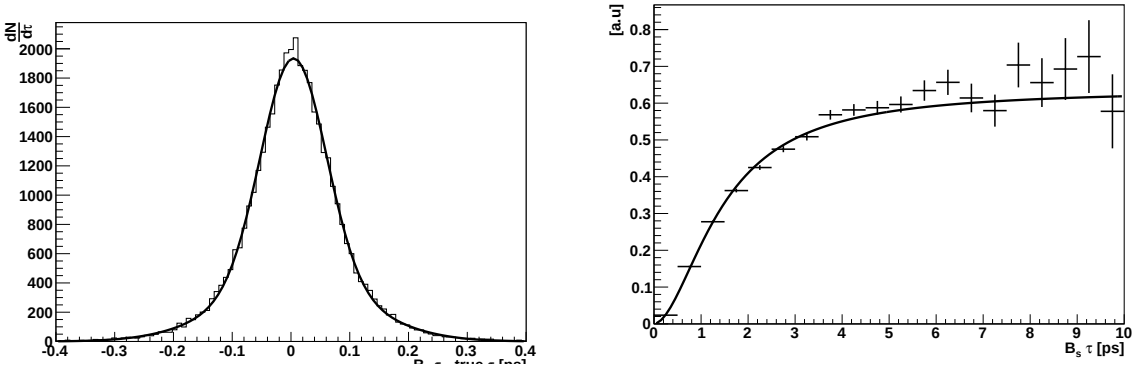

(a) (b)

Figure 4.8: (a) The proper time resolution of $B_s \to \phi\gamma$ from the MC signal sample, parametrized by two Gaussians. (b) The proper time acceptance function, fitted with Eq. 4.16.

The parameters of the functions which characterise the proper time resolution and acceptance will be referred to as the "detector parameters". The values obtained for these from the MC sample are listed in table 4.2.

Physics parameters [29]	
τ_s	$1.472\ ^{+0.024}_{-0.026}$ ps
$\Delta\Gamma_s$	$0.062^{+0.034}_{-0.037}$
Detector parameters	
σ_{core}	50 fs
σ_{wide}	110 fs
μ_{core}	4 fs
μ_{wide}	22 fs
$fraction_{core}$	83%
$\epsilon(t)$	a = 0.84 , c = 2.16

Table 4.2: Summary of the input parameters to Eq. 4.13

In order to extract $\mathcal{A}^\Delta$ from $B_s \to \phi\gamma$ events, their proper time distribution has to be fitted with a function which is the product of Eq. 4.13 and the acceptance function

(Eq. 4.16) convoluted with a resolution model for the proper time. However, recall from the previous section (Eq. 4.15) that the measurement of $\mathcal{A}^{\Delta}$ is simply a measurement of the B_s lifetime in $B_s \to \phi\gamma$. So if it can be demonstrated that the width of the resolution function does not affect the measurement of $\mathcal{A}^{\Delta}$, we can skip the convolution step in the exercise above. To demonstrate this, we perform toy studies to measure the lifetime of a purely exponential decay with different resolutions on the proper time[4].

More technically, in each toy experiment we *generate* 11000 signal events with a purely exponential proper time distribution with a mean of 1.472 ps, convoluted with a single Gaussian, which emulates our detector resolution. We then *fit* this toy data set with an exponential convoluted with a Gaussian, and extract the mean of the former. We perform 1000 such toy MC experiments for a range of values for the width of the detector resolution function.

The result of this exercise is shown in Fig. 4.9, where each point represents 1000 toy experiments. In Fig. 4.9 (a) we plot the mean of the difference between the 1000 fitted lifetimes and the actual lifetime 1.472 ps, for a range of values of the detector resolution (on the x axis). In Fig. 4.9 (b) we plot the resolution of our toy experiment on the lifetime, again as a function of the detector resolution.

From these results we conclude that the width of the proper time resolution function does not bias the measurement of the lifetime (Fig. 4.9 a), nor does it degrade the sensitivity of the (toy) experiment (Fig. 4.9 b). Therefore, we will now report studies for the sensitivity on $\mathcal{A}^{\Delta}$, ignoring the width of the proper time resolution function of our detector.

[4]Note that in this study we do not include any acceptance $\epsilon(t)$.

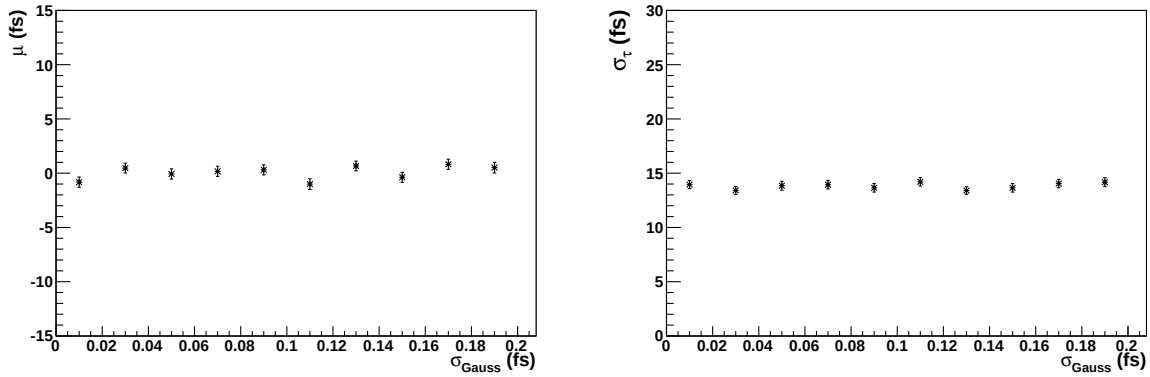

(a) (b)

Figure 4.9: The mean (a) and width (b) of the distribution of the difference between the fitted and actual lifetime (1.472 ps) for 1000 toy experiments, as a function of the width of the Gaussian resolution function.

4.2.3 LHC*b* resolution on $\mathcal{A}^{\Delta}$

We now perform a toy study to determine the purely statistical sensitivity LHC*b* can achieve with 11000 signal $B_s \to \phi\gamma$ events. For this purpose, we *generate* a proper time distribution of 11000 events from the product of Eq. 4.13 and $\epsilon(t)$ from Eq. 4.16, which will be later referred to as $B_{LHCb}(t)$

$$\begin{aligned} \Gamma_{B_s}(t) &\propto |A|^2 e^{-\Gamma_s t}\left[\cosh(\Delta\Gamma t/2) - \mathcal{A}^{\Delta}\sinh(\Delta\Gamma t/2)\right] \quad \text{(From Eq. 4.13)} \\ B_{LHCb}(t) &= \mathcal{N} e^{-\Gamma_s t}\left[\cosh(\Delta\Gamma t/2) - \mathcal{A}^{\Delta}\sinh(\Delta\Gamma t/2)\right]\left(\frac{(at)^c}{1+(at)^c}\right) \end{aligned} \tag{4.17}$$

where $\mathcal{N}$ is a normalization factor, 11000 in our case. The parameters Γ_s, $\Delta\Gamma$, a and c are taken from table 4.2 while an $\mathcal{A}^{\Delta}$ of 0.0 was used to generate our toy sample. We then fit this distribution with $B_{LHCb}(t)$ but let the parameter $\mathcal{A}^{\Delta}$ float. Fig. 4.10 shows the fitted values of $\mathcal{A}^{\Delta}$ for 1000 such toy experiments, while Fig. 4.11 shows the pull distribution.

The width of the distribution in Fig. 4.10, which is 0.2, gives us the LHC*b* sensitivity on $\mathcal{A}^{\Delta}$, for 11000 signal events and the values of input parameters Γ_s, $\Delta\Gamma$, a and c in table 4.2. This translates into a sensitivity of 0.1 on the ratio of right to left handed currents

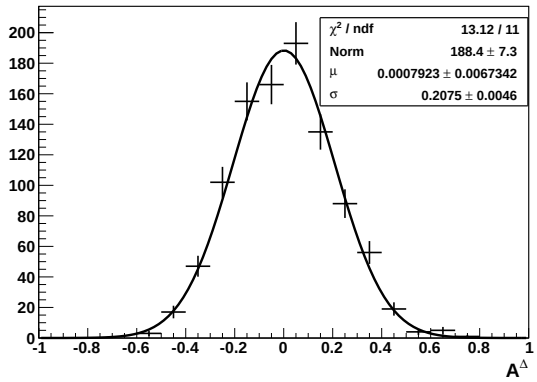

Figure 4.10: A Gaussian fit to the fitted value of $\mathcal{A}^{\Delta}$ from 1000 toy experiments, with the input values of table. 4.2 and 11000 $B_s \to \phi\gamma$ events per experiment.

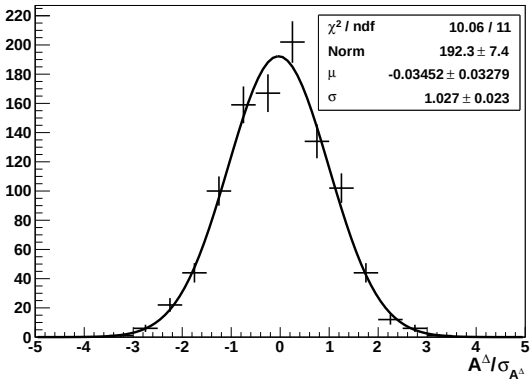

Figure 4.11: The pull distribution for the fits to $\mathcal{A}^{\Delta}$ from 1000 toy experiments, with the input values of table. 4.2 and 11000 $B_s \to \phi\gamma$ events per experiment.

$\frac{\bar{B}_s \to f^{CP}\gamma_R}{\bar{B}_s \to f^{CP}\gamma_L}$ (assuming $\phi_s = 0$). The resolution for non zero input values of $\mathcal{A}^{\Delta}$ is similar, and an example for an input value of $\mathcal{A}^{\Delta} = 0.2$ is shown in Figs. 4.12 and 4.13.

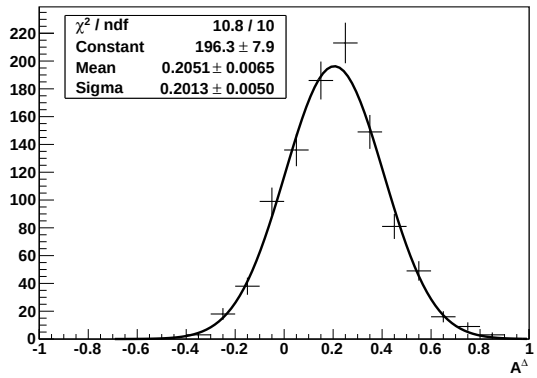

Figure 4.12: A Gaussian fit to the fitted value of $\mathcal{A}^{\Delta}$ from 1000 toy experiments, with the input values of table. 4.2 and 11000 $B_s \to \phi\gamma$ events per experiment. The input value for $\mathcal{A}^{\Delta}$ was 0.2.

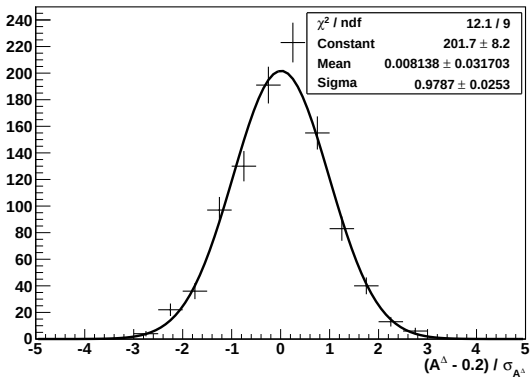

Figure 4.13: The pull distribution for the fits to $\mathcal{A}^{\Delta}$ from 1000 toy experiments, with the input values of table. 4.2 and 11000 $B_s \to \phi\gamma$ events per experiment. The input value for $\mathcal{A}^{\Delta}$ was 0.2.

The input parameters listed in Table. 4.2 are measured quantities, with experimental errors. We now explore the impact of a change in the input values of the various parameters on the fitted value of $\mathcal{A}^{\Delta}$. In order to do that, we *generate* our toy MC sample following Eq. 4.17 using the values of parameters given in Table. 4.2, but *fit* them with slightly

different values, simulating our ignorance of the "true" value of the parameters. We perform this study for each parameter, keeping all others constant in the *generation* and in the *fit*. A correct parameterization of the proper time distribution of the background under the signal peak is very important for this analysis. Here we assume that it can be achieved by extrapolating the background proper time from side bands (Chapter. 7 of [40]), and we do not include any background in the following toy study.

4.2.4 Measurement of $\mathcal{A}^{\Delta}$ and input parameters

The value of Γ_s

The B_s lifetime τ_{B_s} (or $1/\Gamma_s$) is one of the inputs needed in Eq. 4.17, to fit for the value of $\mathcal{A}^{\Delta}$. τ_{B_s} has been experimentally measured to be $\tau_{B_s} = 1.472\ ^{+0.024}_{-0.026}$ ps [29], i.e. to the precision of 1.6%. To estimate the effect of this precision on the measurement of $\mathcal{A}^{\Delta}$, we *generate* the toy data sets with the central value of τ_{B_s} while we vary it from $\tau - 2\sigma_{\tau}$ to $\tau + 2\sigma_{\tau}$ when we *fit* the toy distribution for $\mathcal{A}^{\Delta}$. The result is shown in Fig 4.14 where each point is the mean of the fitted value of $\mathcal{A}^{\Delta}$ from 1000 toy experiments, for a certain value of τ_{B_s} used at the *fitting* stage.

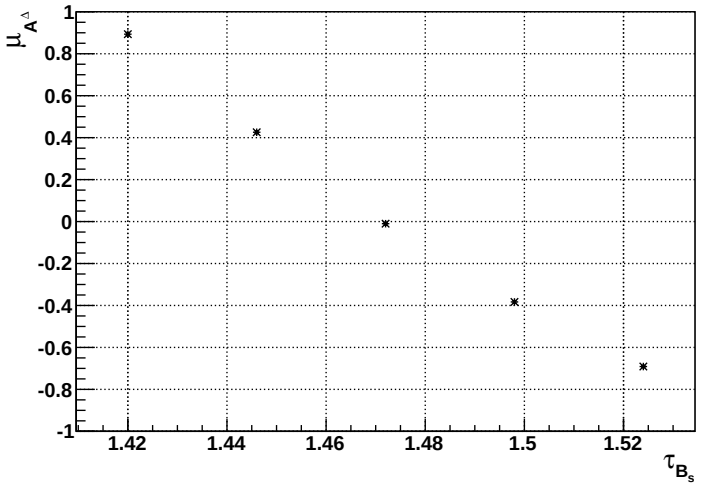

Figure 4.14: The variation in the fitted value of $\mathcal{A}^{\Delta}$ from 1000 toy experiments, as a function of the value of τ_{B_s} used while extracting $\mathcal{A}^{\Delta}$.

A deviation of ∼10-15 fs from the *true* value of τ_{B_s} introduces a shift in the fitted value of $\mathcal{A}^{\Delta}$ which is comparable to the statistical sensitivity on $\mathcal{A}^{\Delta}$. It is therefore important for this analysis that τ_{B_s} is measured to less than 1% of its value. While the current precision is 1.6%, LHCb will improve this precision in $B_s \to \phi J/\psi$ to sub percent level (Chapter 4 of [40]).

The value of $\Delta\Gamma_s$

The width difference $\Delta\Gamma_s$ is currently measured to 50% precision: $\Delta\Gamma_s = 0.062^{+0.034}_{-0.037}$ [29]. To look at the effect of this precision on the measurement of $\mathcal{A}^{\Delta}$, we *generate* the toy data sets with the central value of $\Delta\Gamma_s$ while we vary it from $\Delta\Gamma - \sigma_{\Delta\Gamma}$ to $\Delta\Gamma + \sigma_{\Delta\Gamma}$ when we *fit* the toy distribution for $\mathcal{A}^{\Delta}$. We vary this parameter within 1σ only because the error is quite large, and $\Delta\Gamma - 2\sigma_{\Delta\Gamma}$ is compatible with zero. The result is shown in Fig 4.15 where each point is the mean of the fitted value of $\mathcal{A}^{\Delta}$ from 1000 toy experiments, for a certain value of $\Delta\Gamma_s$ used at the *fitting* stage.

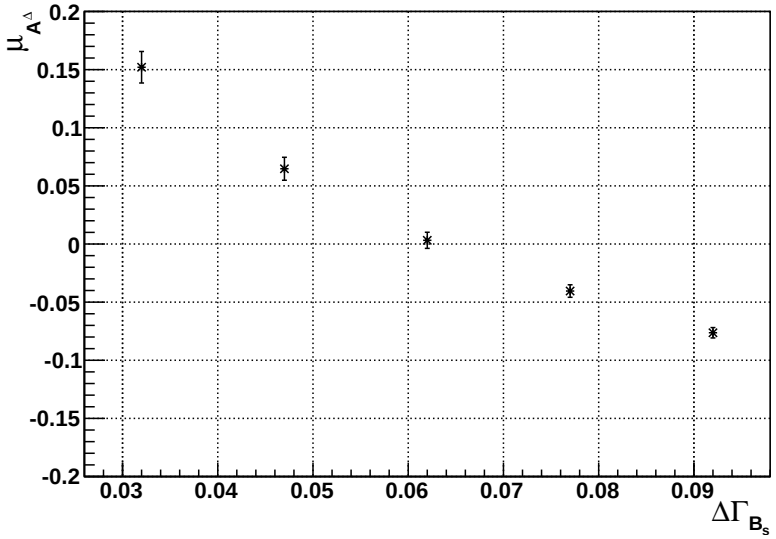

Figure 4.15: The variation in the fitted value of $\mathcal{A}^{\Delta}$ from 1000 toy experiments, as a function of the value of $\Delta\Gamma$ used while extracting $\mathcal{A}^{\Delta}$.

From Fig 4.15 we conclude that the input value of $\Delta\Gamma_s$ introduces a bias on $\mathcal{A}^{\Delta}$ which is not significant compared to the statistical sensitivity for $2\,\mathrm{fb}^{-1}$ ($\sigma_{\mathcal{A}^{\Delta}} = 0.2$). This is only true if $\Delta\Gamma_s$ is indeed small in nature. For a larger *true* value of $\Delta\Gamma_s$, the sensitivity on $\mathcal{A}^{\Delta}$ improves by a factor of 2 as shown in Fig. 4.16. Therefore, to avoid systematic biases on the extracted value of $\mathcal{A}^{\Delta}$, a better precision on $\Delta\Gamma_s$ is required, which will be achieved at LHCb (Chapter 4 of [40]).

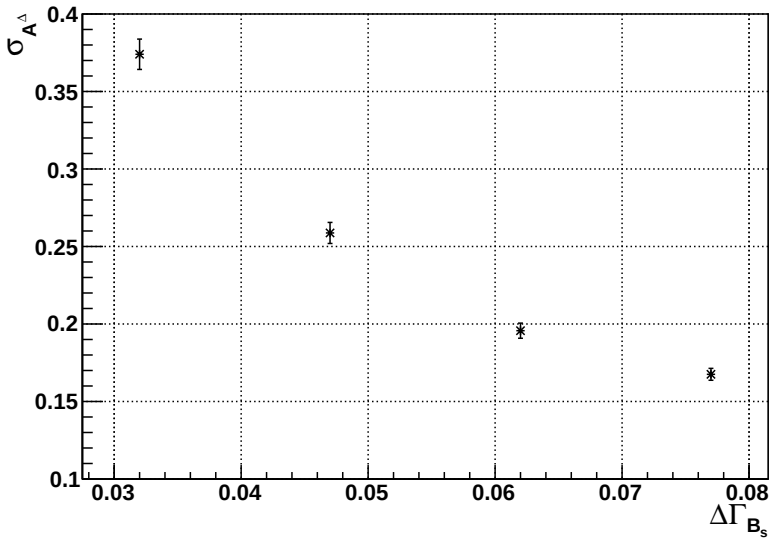

Figure 4.16: The change in the statistical sensitivity of LHCb, $\sigma_{\mathcal{A}^{\Delta}}$, as a function of the value of $\Delta\Gamma_s$.

The proper time acceptance function

The parametrization of the proper time acceptance is also a very important systematic in this analysis. We evaluate the impact of a 2σ variation of the proper time acceptance parameters a and c of Eq. 4.16, which are determined from Monte Carlo.

We *generate* the toy data sets with the central value of a from table 4.2, while we vary it within two standard deviations when we *fit* the toy distribution for $\mathcal{A}^{\Delta}$. We do the same for the parameter c of the acceptance function. The result is shown in Fig 4.17 for a

and Fig 4.18 for c, where each point is the mean of the fitted value of $\mathcal{A}^{\Delta}$ from 1000 toy experiments, for a certain value of a and c respectively, used at the *fitting* stage.

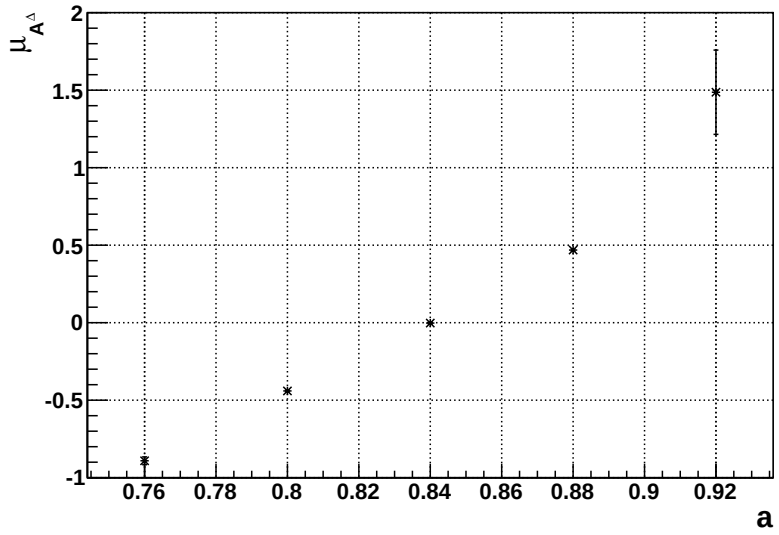

Figure 4.17: Mean of the fitted value of $\mathcal{A}^{\Delta}$ from 1000 toy experiments, as a function of the input value for parameter a. The value used at the *generating* stage was 0.84.

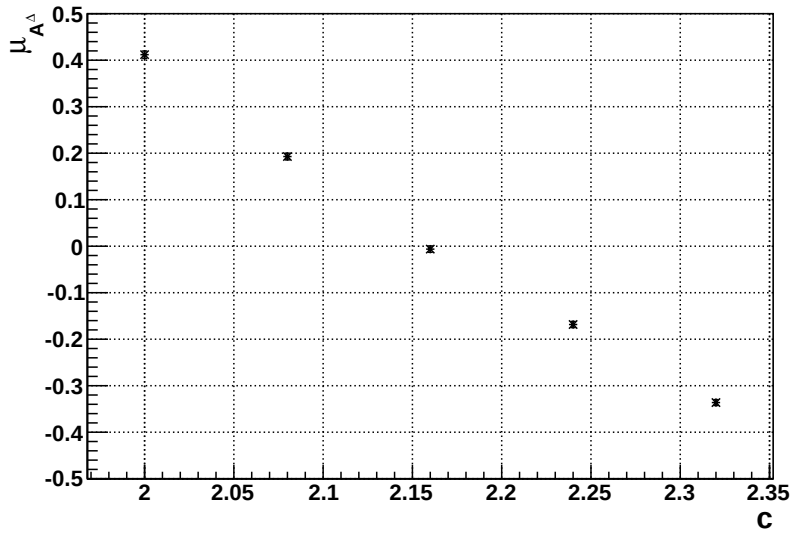

Figure 4.18: Mean of the fitted value of $\mathcal{A}^{\Delta}$ from 1000 toy experiments, as a function of the input value for parameter c. The value used at the *generating* stage was 2.16.

From Figs. 4.17 and 4.18 we conclude that a 1σ shift in the acceptance parameters introduces a systematic shift in $\mathcal{A}^{\Delta}$ which is comparable to the statistical accuracy on $\mathcal{A}^{\Delta}$. Therefore, the proper time acceptance function needs to be determined to 2-3 % level.

Bias in the proper time reconstruction

Although we have seen that the width of the proper time resolution of the detector does not affect the measurement of $\mathcal{A}^{\Delta}$, any bias in the resolution function will indeed affect the measurement. A bias of 4 fs in the core Gaussian component and about 20 fs in the second Gaussian component of the proper time resolution has been observed in $B_s \to \phi\gamma$ events from Monte Carlo simulation (table 4.2). The reason will be discussed in detail in Chapter 8, but here we estimate the affect of such a bias on the measurement of $\mathcal{A}^{\Delta}$.

We *generate* the toy data sets with the value of input parameters reported in table 4.2. It is important to note that for this study, we do not convolute the proper time ($B_{LHCb}(t)$) with a resolution (Gaussian) function. This is because the width of the resolution is irrelevant for the extraction of $\mathcal{A}^{\Delta}$. We want to simulate a *bias* in the proper time reconstruction, so we bias the toy data set by adding a small quantity to the proper time of each of the 11000 events of our *generated* sample. We then *fit* this distribution but do not take into account the bias we have introduced.

The result is shown in Fig 4.19 where each point is the mean of the fitted value of $\mathcal{A}^{\Delta}$ from 1000 toy experiments, for a certain value of the 'bias' in the proper time measurement that we introduced when *generating* the sample. From this figure, we can conclude that a bias of $\sim$20 fs introduces a systematic shift in the fitted value of $\mathcal{A}^{\Delta}$ which is comparable to the statistical sensitivity on $\mathcal{A}^{\Delta}$. Therefore, it is important to understand the bias in the proper time reconstruction to this level.

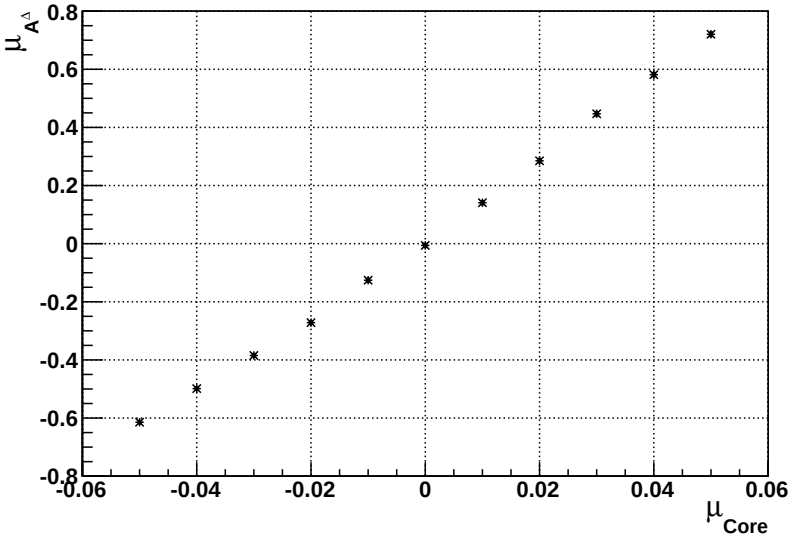

Figure 4.19: The fitted value of $\mathcal{A}^\Delta$, for a 1000 toy experiments, where the bias in the proper time μ_{Core} was varied from -50 to 50 fs.

A more detailed discussion on the causes and a possible correction for the bias will be undertaken in Chapter 8.

4.3 Summary

Right handed currents due to NP operators in radiative penguin B decays are a remarkable sign of its presence. In this chapter we motivated this subject by an example of A_{FB} in $B_d \to K^* \mu\mu$ and introduced the parameters which allow to probe right handed currents in radiative B decays of type $B \to f_{CP}\gamma$.

B factory measurement in this area were presented and the LHCb analyses were introduced. In particular, we looked at the sensitivity of LHCb on the parameter $\mathcal{A}^\Delta$ in the decay $B_s \to \phi\gamma$ and also identified systematic effects which could bias this measurement.

A sensitivity of 0.2 on $\mathcal{A}^{\Delta}$ translates into a sensitivity of 0.1 on the ratio of right to left handed components $\frac{A_R}{A_L}$. SM predicts this ratio to be at 1% level while NP scenarios predict large deviations [49, 63]. We show that in order to achieve this sensitivity at LHCb, the reconstruction of the proper time of $B_s \to \phi\gamma$ needs to be understood up to % level. We also show that a precision of 1% is required on the lifetime of the B_s, and improvement in the measurement of $\Delta\Gamma_s$, which is currently known to about 50%. LHCb will achieve these with $2\,\text{fb}^{-1}$ in the decay $B_s \to \phi J/\psi$ (Chapter 4 of [40]).

The decay $B_d \to K^*\gamma$ is very similar to $B_s \to \phi\gamma$ and can be used to test and validate the trigger and reconstruction chain for radiative decays at LHCb. The branching ratio of the former is also about 5 times higher, so LHCb will collect reasonable statistics for $B_d \to K^*\gamma$ much before $B_s \to \phi\gamma$.

In the next chapter we describe the LHCb detector and its performance with the 2010 data. This will be followed by the trigger strategy to select radiative decays in Chapter. 6. We will then show the $B_d \to K^*\gamma$ and $B_s \to \phi\gamma$ signal seen in the data and some studies on the validation of the photon reconstruction in Chapter. 7. Finally, some discussion on the $B_s \to \phi\gamma$ proper time bias correction, and the extraction of acceptance function from data will be presented in Chapter. 8.

Chapter 5

The LHC*b* detector and its performance

5.1 Introduction

LHC*b* is a dedicated B physics experiment at the Larger Hadron Collider at CERN. The aim of the experiment is to search for New Physics via precision measurements of CP violating effects in B hadrons and their rare decays. LHC*b* benefits from the large $b\bar{b}$ cross section at the LHC; compare $\sim$300 μb at $\sqrt{s} = 7$ TeV of which about 25% is inside the LHC*b* acceptance [66], to $\sim$1 nb at the B factories. This results in copious production of all kinds of B hadrons, especially B_s and B baryons, which are not accessible to B factories.

The design collision energy of the LHC is 14 TeV and a bunch crossing rate of 40 MHz, at which it is designed to provide an instantaneous luminosity of $10^{34}\, cm^2 s^{-1}$. The LHC beam optics allow for the beams to be defocused at the LHC*b* interaction point, and the experiment was designed to be operated at a lower instantaneous luminosity of $2 \times 10^{32}\, cm^2 s^{-1}$. With this configuration, each LHC bunch crossing at the LHC*b* interaction point is domi-

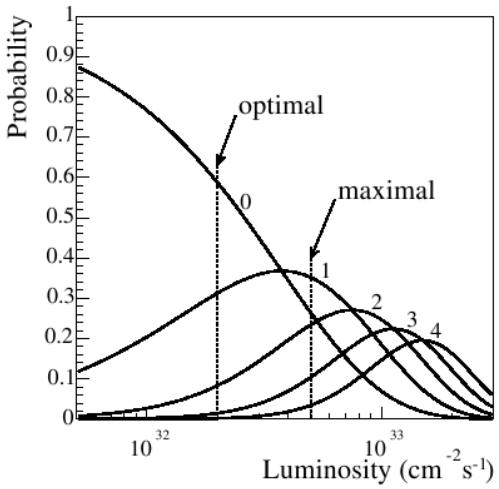

Figure 5.1: The probability of having different number of proton proton collisions per bunch crossing, as a function of instantaneous luminosity (Figure from [67]).

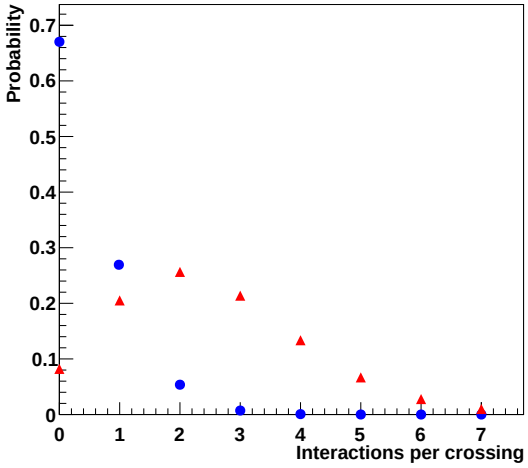

Figure 5.2: Probability of having a number of proton proton collisions in a bunch crossing at the LHCb interaction point. Blue circles are for the nominal LHCb operation μ =0.4 and red triangles are for μ = 2.5.

nated by a single proton proton collision, as shown in Fig. 5.1. This choice was motivated by the reconstruction of rare B decays, which benefits from the cleaner environment, as the detector occupancy is relatively lower in events with a single pp interaction. For this scenario, the mean (μ) of the Poisson probability to have an inelastic pp interaction in a bunch crossing, at the LHCb collision point is 0.4. The distribution of the probability as a function of the number of pp interactions is shown as blue circles in Fig. 5.2.

In 2010, the LHC started operating at a collision energy of 3.5 TeV per beam and at a lower than nominal instantaneous luminosity. In order to collect sufficient integrated luminosity (Fig. 5.3), the beam optics were adjusted such that the per bunch interaction probability (μ), at the LHCb interaction point was about $\sim$ 1.7 to 2.5, significantly higher than what the detector was designed for. In such running conditions, the probability to have more than one pp interactions per bunch crossing is much higher than the default scenario of μ =0.4, as shown by the red triangles in Fig. 5.2. Nevertheless, the LHCb trigger and reconstruction software have been adapted very well for performing in such harsh environment, which we will discuss after describing the detector layout.

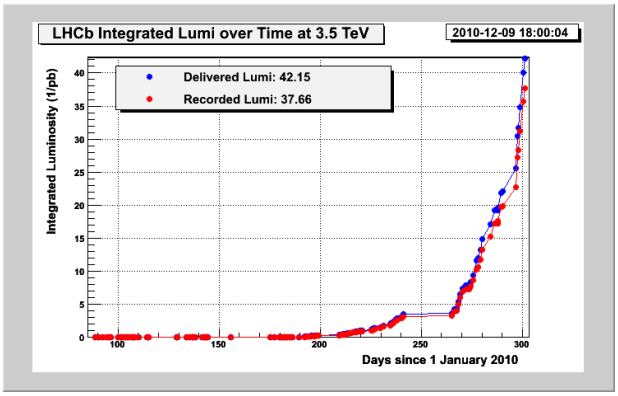

Figure 5.3: Trend plot of the integrated luminosity collected by the LHCb detector in 2010. By the end of 2010, the detector accumulated $\sim 38\,\mathrm{pb}^{-1}$.

5.1.1 Detector Layout

The $b\bar{b}$ quark pairs produced in pp collisions at LHC are produced in a backward or forward cone around the interaction point [68], and therefore, LHCb has been designed as a single arm spectrometer from a series of sub-detectors (Fig. 5.4). The sub detectors, in sequence of their distance from the interaction point are:

1. The vertex locator, VELO, a Silicon strip detector composed of semi circular detecting planes, arranged in two halves around the beam pipe. The VELO provides excellent vertex reconstruction and Impact parameter resolution.

2. The Ring Imaging Cherenkov Detector (RICH1), uses aerogel and C_4F_{10} gas as radiators and provides particle identification (PID) for low momentum particles 1-60 GeV/c.

3. The Trigger Tracker (or TT), a Silicon strip detector, part of the tracking system.

4. The (warm) spectrometer dipole magnet, covers the entire LHCb acceptance and provides an integrated field of 4.2 Tm.

5. The tracking stations T1 - T3, employing Silicon strip in the innermost part and Straw tube technology in the outer part.

6. The RICH2 detector, uses CF_4 gas as radiator and provides PID for high momentum particles 15-100 GeV/c

7. The Calorimeter system, consisting of Scintillator Pad Detectors and Preshower (SPD and PS), Electromagnetic and Hadronic calorimeters (ECAL and HCAL). The system provides particle identification and energy measurement for photons, electrons and hadrons. It also participates in the Level 0 trigger.

8. The Muon stations, realised as Multi Wire Proportional Chambers. They provide muon identification and momentum determination and also the Level 0 muon trigger.

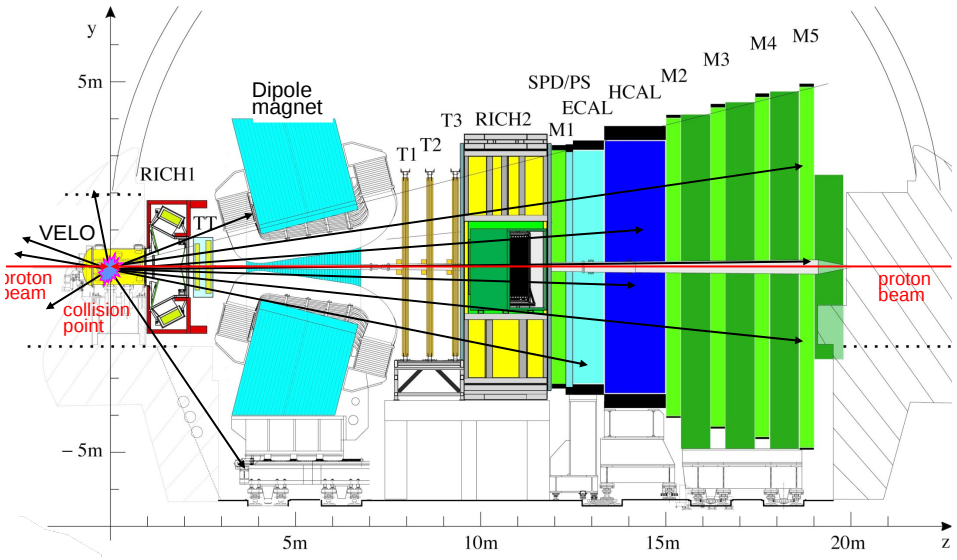

Figure 5.4: Schematic view of the LHCb detector. The two proton beams of the LHC and their interaction point in the LHCb detector are indicated (Figure from [68]).

The LHCb spectrometer has an outer acceptance of 300 mrad in the horizontal direction and 250 mrad in the vertical direction. The larger horizontal acceptance is due to the LHCb magnet, which bends the charged particles in the horizontal plane. The inner acceptance of 10 mrad in both directions, is given by the LHC beam pipe.

The sub detectors particularly important for the reconstruction of radiative decays are the VELO, the tracking stations, the RICH PID system and the ECAL. In the following we briefly review the validation of their performance with the 2010 data set.

5.2 VELO

The VELO is used to reconstruct the Primary and Secondary (B decay) vertices, denoted later in the text by PV and SV respectively. The performance of the VELO detector is reflected in the vertex and Impact Parameter (IP) resolutions. The PV resolution is measured in data by randomly splitting the tracks into two subsets, and reconstructing a vertex from each of them.

Fig. 5.5 and 5.6 show the vertex resolution in x, y and z coordinates, as a function of the number of tracks used to reconstruct them. A resolution of $\sim 15\,\mu$m for the x and y coordinates, and of $\sim 90\,\mu$m for the z coordinate has been achieved [69] for vertices made with more than 25 tracks, which is close to the performance expected from MC.

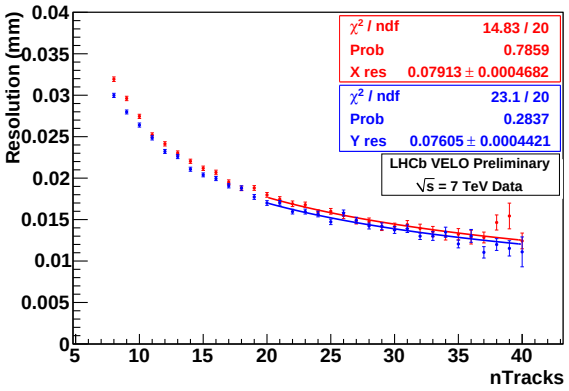

Figure 5.5: The PV resolution in the x and y coordinates, measured in the 2010 data (Figure from [70]).

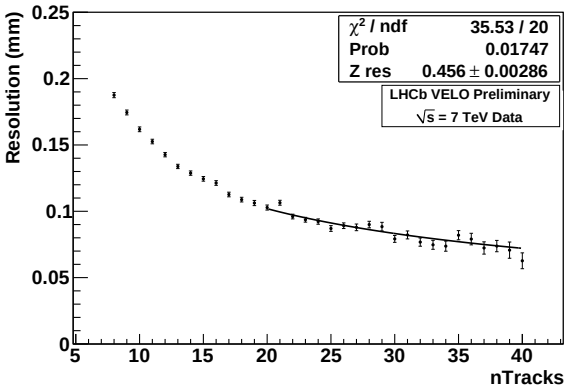

Figure 5.6: The PV resolution in the z coordinate, measured in the 2010 data (Figure from [70]).

The IP resolution is closely related to the PV resolution, and is a crucial ingredient for the analysis of $B_s \to \phi\gamma$ and $B_d \to K^*\gamma$ decays, where the χ^2 of the IP of the charged tracks (from the ϕ and K^*) is used as a discriminating variable to separate signal and background [71]. The IP resolution measured in data is very close to the expectation from simulation, especially for tracks with high P_T. Fig. 5.7 shows the IP resolution measured in data, as a function of the inverse of the P_T of the track, along with the MC expectation. For this study, events with only one reconstructed PV which produced more than 25 tracks were used, and the PVs were refitted after excluding the track, the IP of which was being calculated [69].

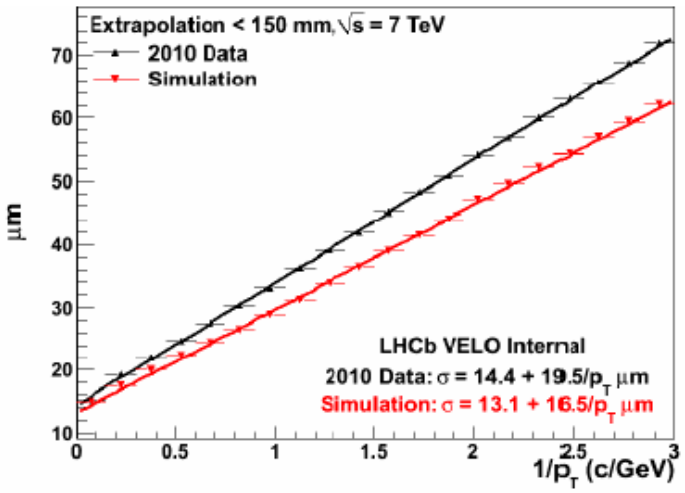

Figure 5.7: The resolution on the Impact Parameter (IP), as a function of inverse P_T of the charged tracks. Only the tracks which had the first hit in VELO within 150 mm of the PV were considered (Figure from [72]).

Individual hit resolution in the VELO sensors and the individual sensor alignment have also been measured and found to be very close to MC expectations [73, 74]. The most probable cause of the remaining small discrepancies between data and simulation is material description, and this issue is being addressed with due urgency.

5.3 The RICH Detectors

The separation between *pions* and *Kaons* is an important ingredient in the analysis of B decays. Specifically, for $B_s \to \phi\gamma$ and $B_d \to K^*\gamma$, this separation is an important variable used to discriminate between signal and background [71].

As an illustration of the importance of PID, the invariant mass of two *Kaons* forming $\phi \to KK$ candidates in $\sqrt{s} = 900$ GeV data is shown in Fig. 5.8, with and without the use of PID information. From the plot on the left, we can see that the signal is barely visible with the use of kinematic cuts, while the ϕ peak is clear after the use of PID information on the *Kaons*. For this figure, a $\Delta log\mathcal{L}(k-\pi) > 15$ has been applied on both kaons. This means that the likelihood returned by the RICH algorithms for the track to be a *Kaon* is greater than 10^{15} times the likelihood for it to be a *pion*.

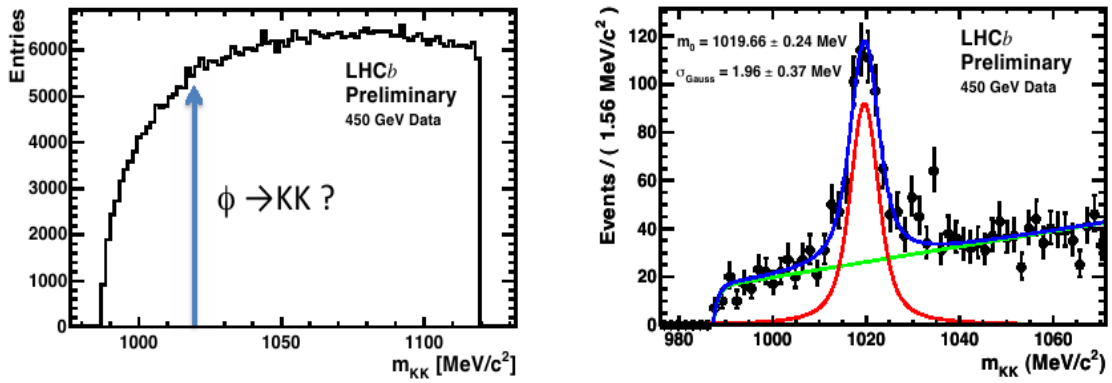

Figure 5.8: Performance of the RICH PID. Left, the KK invariant mass with kinematic cuts only. Right, *Kaon* PID cut applied on both charged tracks (Figure from [75])

LHCb houses two RICH detectors (Fig. 5.4) which use three different radiators, to provide PID for *pions*, *Kaons* and *protons* over a wide momentum range. These detectors use Cherenkov light (photons emitted by charged particles as they travel in a certain medium at a speed greater than the speed of light in that medium) to determine the speed

of the charged particles traversing their volume. Cherenkov light is emitted in a cone, the opening angle (Cherenkov angle, θ) of which is related to the particle speed (βc) and the refractive index of the medium (n) by

$$cos\theta = \frac{1}{n\beta}. \tag{5.1}$$

The RICH1 detector uses two radiators, aegorel and C_4F_{10} and is located right after the VELO, upstream of the LHCb magnet. It provides PID for relatively low momentum particles (1-60 GeV), which are likely to be bent out of the acceptance by the magnet. The RICH2 detector uses CF_4 gas radiator and is located downstream of the magnet and the tracking stations. It provides PID for particles in the momentum range of 15-100 GeV.

Both RICH detectors use the Hybrid Photon Detectors (HPDs) to detect the Cherenkov photons. Due to material budget constraints, the photon detectors cannot be placed within the LHCb acceptance, so a set of spherical and planar mirrors are used to focus and reflect the Cherenkov light onto the photon detectors. The HPD planes are located above and below the beam pipe in RICH1, while in RICH2, they are located on the right and left side of the beam pipe, as shown in Fig. 5.9 and 5.10.

5.3.1 Monitoring of the RICH mirrors

The performance of the RICH detectors depends upon the resolution of the Cherenkov angle. This resolution has contributions from many sources discussed in [76, 68]. Any possible misalignment of the mirrors and photon detector planes will degrade this resolution. Hence, they must be understood and controlled if possible, to ensure that their contribution is negligible as compared to other sources of finite angular resolution. Several steps have been taken to achieve this understanding. A survey of mirror and detector components

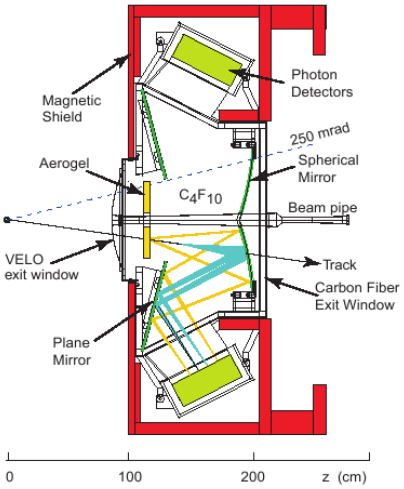

Figure 5.9: Schematic of RICH1 detector, indicating various hardware components (Figure from [68]).

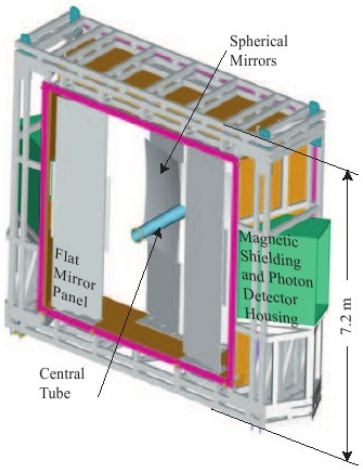

Figure 5.10: Schematic of RICH2 detector, indicating various hardware components (Figure from [68]).

and the alignment of the RICH mirrors with data are described in [77]. A Laser Alignment Monitoring Systems (LAMS) is installed inside each of the RICH detectors to monitor the stability of the mirrors. The basic idea of the system can be visualized in Fig. 5.11 which shows the two coupled units of the RICH1 LAMS system.

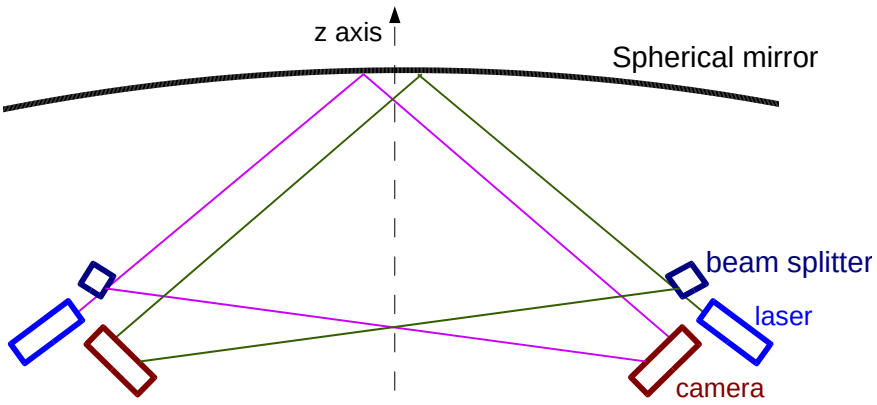

Figure 5.11: Two coupled units of the LAMS as seen from above the beam pipe. For the purpose of clarity, various optical components are colour coded and so are the laser beams. The direction of the beam pipe is indicated by the vertical arrow, which is the direction of the z axis in LHCb coordinate system.

Each unit is composed of a Laser, a beam splitter and a camera. The laser mounted on the unit on the left sends part of the laser beam to the camera mounted on the unit on the right (the resulting spot on the camera is called the reference spot later in the text) and part of it to the spherical mirror in front of it (i.e. left in the picture), which after reflection goes to the camera on the unit to the right (the resulting spot on the camera is called the reflected spot later in the text). Therefore, the camera attached to the unit on the right monitors the mirror segment on the left and vice versa.

The purpose of the reference spot is to distinguish between a movement of the mirror segment and of the LAMS subsystem (or even individual units of the system), because the former causes only the reflected spot to move while the latter causes both of the spots to move, but a combination of the two movements is also possible.

In order to do any calculations with the above setup, three dimensional equations are required. However, since the center of curvature of the mirror, the camera, and the laser source are arranged to lie in the same plane, the problem can be reduced to a two dimensional one. The position and angle of the optical components can be calculated for them to be in the same plane as the center of curvature of the mirrors. This setup was not precisely achieved because during the installation of the system, one required additional flexibility because the optical components had to be installed in such a way to allow the laser beam to hit the correct mirror at the desired location and then get the reflected beam to hit the camera sensor on the other side.

No survey has been conducted after the installation of the LAMS [1], so the exact angles and positions of the optical components are not known. This information, however, is very

[1] This would have required exposing the hygroscopic aerogel to the atmosphere for longer than we would wish

important for a complete understanding of the data from this system. Once the system is understood, it can act as a very sensitive and complementary hardware test of the global software alignment.

A quick calculation for the sensitivity of the system can be performed using Fig. 5.11. Once a beam is reflected off a mirror, the distance it has to travel to get to the camera sensor can be estimated to be about 1 m. If the reflected spot on the camera sensor moves by 0.1 mm (or 13 pixels on the camera sensor) the movement will correspond to a 0.05 mrad rotation/distortion of the mirror or the gas enclosure. And if the spot positions can be calculated down to pixel level, one could achieve sensitivity to a rotation of 0.005 mrad.

The author wrote the analysis software (in C++) to analyse the images and calculate the position of the spot centers. This is a simple weighted average of the positions of the pixels with a certain "signal" height (The details are documented in this LHC*b* note [2]). Some results are shown in Fig. 5.12, where the change in the y coordinate (in a two dimensional coordinate frame, the (0,0) of which lies at the center of the camera sensor) of the center of the reference spot on one of the RICH1 cameras (in pixel numbers) is plotted vs time. Also shown are the pressure and temperature values.

The movements of the spots on the camera sensor can be seen to be strongly correlated with temperature and pressure changes in the gas enclosure. In the particular case in Fig. 5.12, there was a quite large temperature variation of about 2 Kelvin and the spot centers moved by 3-4 pixels. This corresponds to ~ 0.08 mm on the camera sensor and a $<$ 0.05 mrad rotation/distortion of the gas enclosure, mirror or both. The spot positions are sensitive to quite small pressure variations as well, those observed here are of the order of 0.2 mbar. They do not correspond to a significant rotation/distortion in the gas enclosure

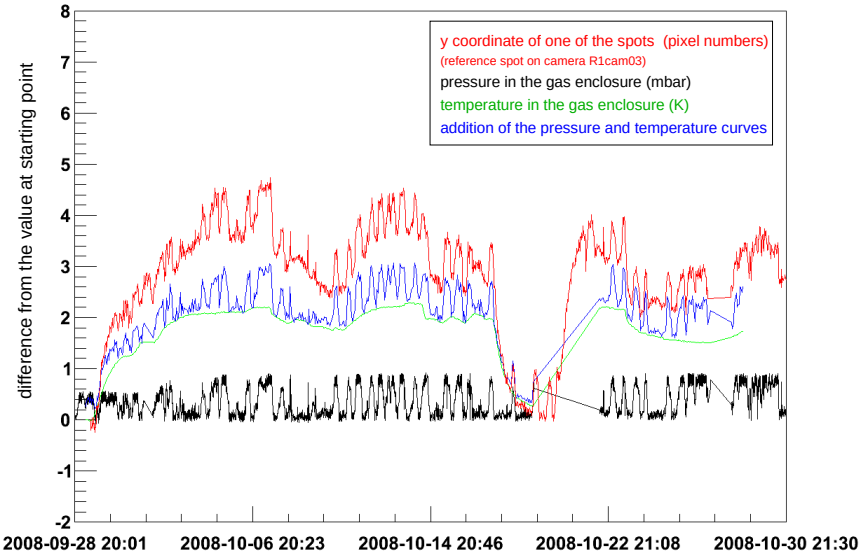

Figure 5.12: The red curve is the shift in pixel numbers, of the y coordinate of the reference spot on a RICH1 camera. The green curve is the change in temperature inside the gas enclosure (in Kelvin) and the black curve is the change in the pressure (in mbar). The difference from the initial values of these quantities at the time of the start of data taking are plotted. In blue is a simple addition of the black and green curves. The horizontal axis is the date and time of when the particular image was taken.

but illustrate the sensitivity of the system.

The blue curve shows the addition of the temperature and pressure (differences and not absolute values) and this naive addition very closely follows the behaviour of the spot coordinate (shown in red). This seems promising because one can fit the data for the following equation

$$\Delta x = aT + bP \tag{5.2}$$

where x is x or y coordinate of a light spot and T and P are the temperature and pressure values respectively. One can extract the constants a and b for all the light spots, which could then be used to disentangle the movements due to pressure or temperature changes and due to some other effect. Such an analysis will be pursued in future.

The author played a vital role in setting up and debugging of the analysis software package, and also analysed large volumes of data manually, until the system was automatised. Currently, data acquisition is done via a control software developed using PVSS 3.8 [78]. The project runs on a dedicated Linux machine at Point 8, collects and saves images from each of the LAMS cameras (4 and 11 inside RICH1 and RICH2 respectively) at regular intervals (30 minutes and 1 hour for RICH1 and RICH2 respectively). The saved images are accessed by the analysis algorithm, and the results are returned to the control system. This communication employs CERN's Distributed Information Management system (DIM) [79]. On receiving analysis results, the control system checks for error reports before appending the results to the accumulated data for each camera. A graphical user interface or panel has also been developed as part of the control system (not by the author), which allows for monitoring and control of the processes described above, as well as the display of the accumulated image analysis results. This system is available to the person in control of the RICH detectors at the LHCb control room for monitoring purposes.

5.3.2 The RICH PID performance

The performance of the PID is expressed as the probability to identify a particular species of particles correctly, as a function of their momenta. The probability to correctly identify a *Kaon* is determined by tag and probe method, where one kaon from $\phi \rightarrow KK$ is required to have a "good" *Kaon* PID while and the PID of the other *Kaon* is probed. This approach was used in 2009 (during the 450 GeV per beam LHC run), while with larger statistics in 2010, $D^* \rightarrow D(K\pi)\pi$ decays were used. Clean samples of D^* decays can be isolated with kinematic cuts only, where the mass difference $m_{D^*} - m_{(D \rightarrow K\pi)}$ provides a very good handle to reject background. Fig. 5.13 shows results after a $\Delta log\mathcal{L}(k - \pi) > 0$ cut on the *Kaon* track has been applied. The efficiency of this cut, i.e. a positive identification of *Kaons*, is

better than 80% for a large momentum range, and matches well with MC expectations as shown in Fig. 5.13.

To quantify the chance of mis-identifying *pions* as *Kaons*, $K_s \rightarrow \pi\pi$ decays are used, where a clean signal can be obtained with kinematic cuts alone, and one can thus calculate the probability of assigning a *Kaon* PID to a *pion* [75]. After a cut of $\Delta log\mathcal{L}(k-\pi) > 0$, the mis-ID is estimated to be $<= 20\%$ as shown in Fig. 5.13. These results are already close to MC expectations and further improvements in the performance are foreseen [75].

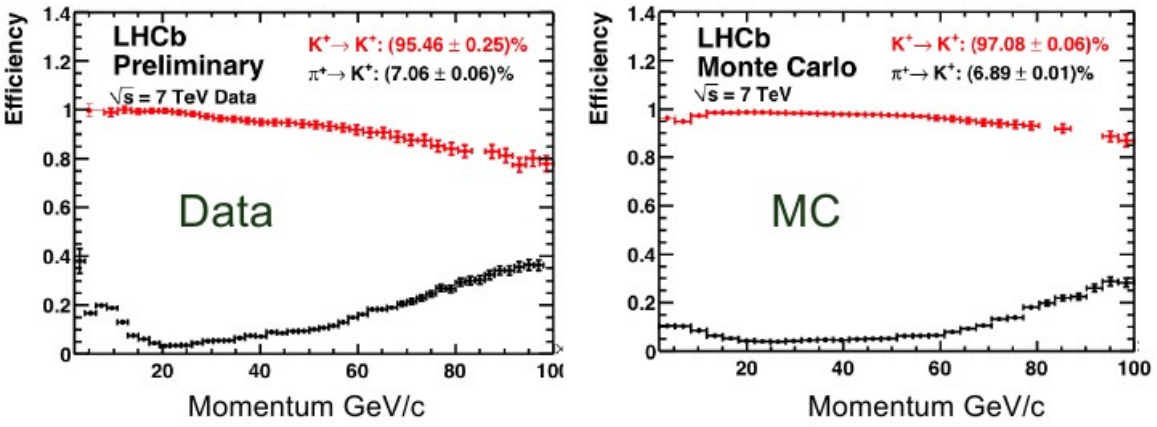

(a) (b)

Figure 5.13: RICH performance using $D^* \rightarrow D(K\pi)\pi$ decays as measured in data (a) and predicted in MC (b). The red curve shows the probability to identify a *Kaon*, while the black one shows the probability to mis-identify a *pion* as a *Kaon*.

As mentioned earlier, the LHC*b* detector has performed very well even in a high multiplicity environment it was not designed to handle. Fig. 5.14 shows the RICH performance for positive *Kaon* identification and *pion* mis-ID probability for events with different track multiplicities. A slight degradation in performance is seen for very high multiplicity events. Nevertheless, the mis-ID efficiency can still be kept relatively low (15%) while keeping a reasonably high (90%) efficiency for positive identification.

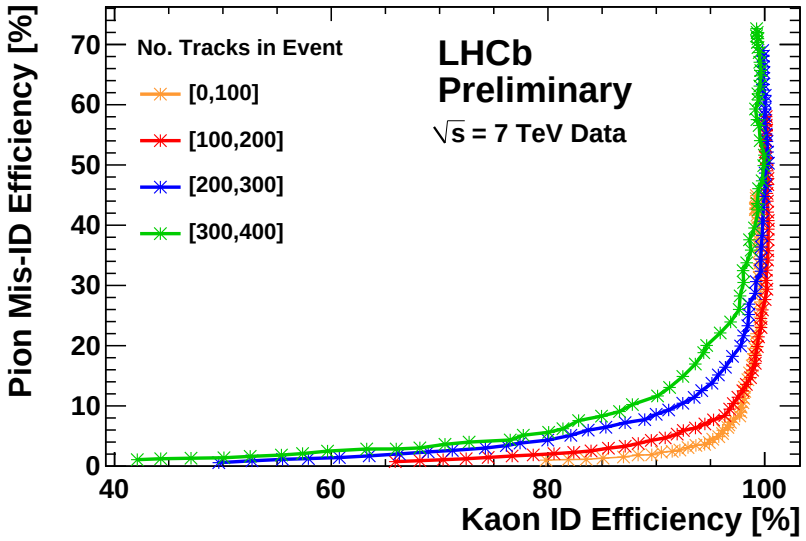

Figure 5.14: The RICH PID performance (all three radiators) for tracks with $P < 10\,\mathrm{GeV/c}$. The different curves show the positive *Kaon* ID and the *pion* mis-ID efficiency for events with different track multiplicity (Figure from [80]).

5.4 The Tracking system

The tracking system is composed of a Silicon strip detector (TT) upstream of the magnet, and three tracking stations T1-T3 downstream, which employ Silicon strip technology in the inner part (IT) and Straw tube technology in the outer parts (OT).

The hit resolution has been measured in data for the TT and IT to be 55 μm and 250 μm for the OT [69], which are close to the ones predicted by simulation. The remaining modest discrepancies are expected to shrink with further understanding of the detector alignment and improvements in simulation.

The tracking efficiency for long tracks (tracks that traverse the entire tracking system, VELO, TT, T1-3) has also been measured in data as shown in Fig. 5.15. The method employed here is again tag and probe, using $K_s \to \pi\pi$ decays, where the tag *pion* is reconstructed as a long track and the probe *pion* is reconstructed using only the VELO track

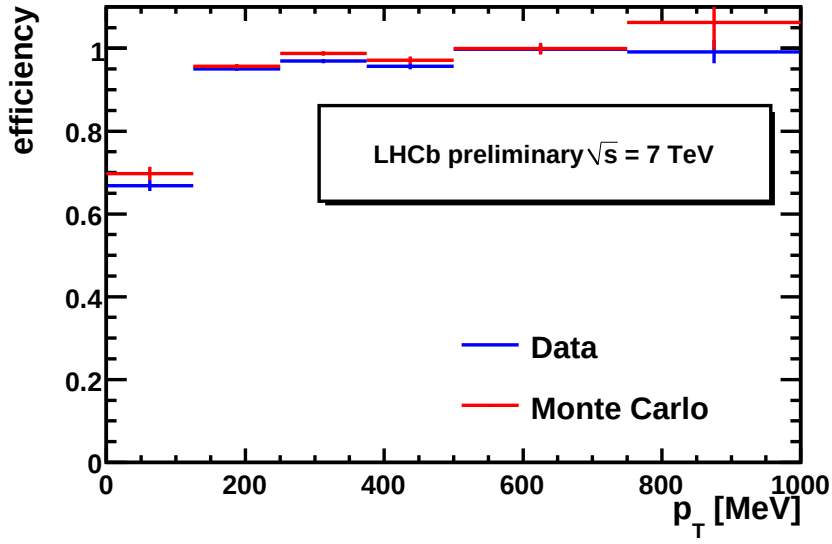

Figure 5.15: The tracking efficiency for long tracks, using tag and probe method on the *pions* from $K_s \to \pi\pi$ (Figure from [70]).

segment and calorimeter cluster. The efficiency of the tracking stations is then measured by requiring a matching track segment (for the probe track) in the tracking stations. From Fig. 5.15, this efficiency is above 95% for tracks with a reasonably high P_T of >200 MeV.

The momentum resolution achieved by the tracking detectors is quite close to MC predictions, which is reflected in the excellent mass resolutions achieved on various B and D decays [70, 73].

5.5 Calorimeter

LHCb uses a sampling calorimeter system to provide identification for electrons, photons and hadrons and to measure their energy and position. The system is situated downstream of the RICH2 detector (Fig. 5.4) and is composed of a Scintillating Pad Detector (SPD) and Preshower (PS) system followed by an electromagnetic (ECAL) and a hadronic calorimeter (HCAL). A schematic view of the system is shown in Fig. 5.16.

The SPD/PS system helps to distinguish between charged and neutral particles, as only charged particles will produce light in the SPD. Further, the PS provides separation between electrons and charged *pions*, as the electrons will shower in the 15 mm thick lead absorber placed between the SPD and PS, while *pions* will shower much later. So the presence of energy in the PS helps to separate *electrons* from *pions*. The calorimeter decision is also used in the Level 0 trigger, which in implemented in the hardware.

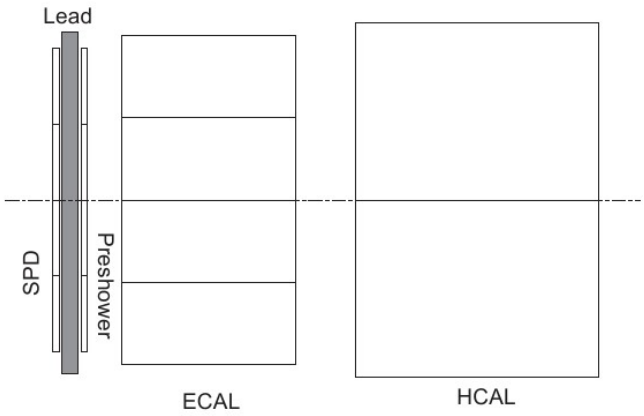

Figure 5.16: Schematic side view of the calorimeter system (Figure from [81]).

All the detectors in the calorimeter system use similar technology, scintillating tiles as active material, lead or iron as absorbers. The SPD and PS systems constitute 2 radiation lengths, while the ECAL and HCAL, respectively, are 25 radiation lenghts and 5.6 interaction lengths deep. These detectors are read out using wavelength shifting fibres and Photon Multiplier Tubes (PMTs). The outer acceptance of the calorimeter system matches the LHCb acceptance, but its inner acceptance is limited to 30 mrad to avoid radiation damage of the detector elements.

The ECAL cells have a variable lateral segmentation, due to the varying hit density over the calorimeter surface. The choice of segmentation is largely influenced by the re-

quirement to separate the two photons from high energy π^0s. In the inner region (close to the beam pipe), the cell size is 40.4 mm while in the middle and outer regions it is 60.6 mm and 121.2 mm respectivly, as shown in Fig. 5.17. The number of cells in each of these regions was optimized, taking a total of about 6000 channels as a constraint [82]. The HCAL is divided into two regions, the inner with a cell size of 131.3 mm and the outer with a cell size of 262.6 mm, and a total of about 1500 channels.

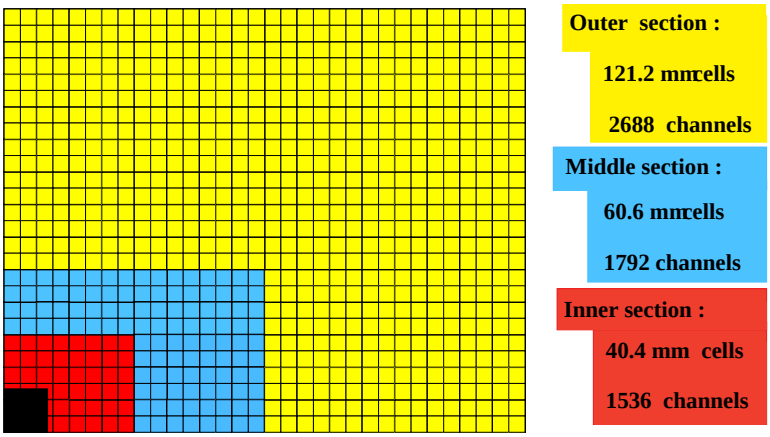

Figure 5.17: The lateral segmentation of the LHCb ECAL, SPD and PS (Figure from [82]).

The ECAL is vital to the triggering and reconstruction of radiative decays $B_s \to \phi\gamma$ and $B_d \to K^*\gamma$. The mass resolution of these decays is about 100 MeV [71] and is dominated by the calorimeter resolution, which is given by [68]

$$\frac{\sigma_E}{E} = \frac{10\%}{\sqrt{E}} \oplus 1\% \quad \text{(E in GeV)} \tag{5.3}$$

The noise term contributes 0.1% up to 1% depending on polar angle of the cluster being reconstructed, because the ECAL is calibrated in transverse energy. This term is neglected in the fit [83].

Each of the four calorimeter sub systems are equipped with LEDs to monitor the gain stability of the PMTs, even during data taking. The idea of the monitoring system is to illuminate the PMT using an LED. The LED also illuminates a PIN diode to monitor its light output. The intensity of the LEDs is controllable and is varied to monitor the linearity of the PMTs.

Since the start of the 2010 data taking period, a gain stability of 1% has been observed for the calorimeter cells. Decays like $\pi^0 \to \gamma\gamma$, $J/\psi \to ee$ and D decays involving π^0s have been reconstructed with close to Monte Carlo resolutions (Fig. 5.18), demonstrating an excellent understanding of the calibration.

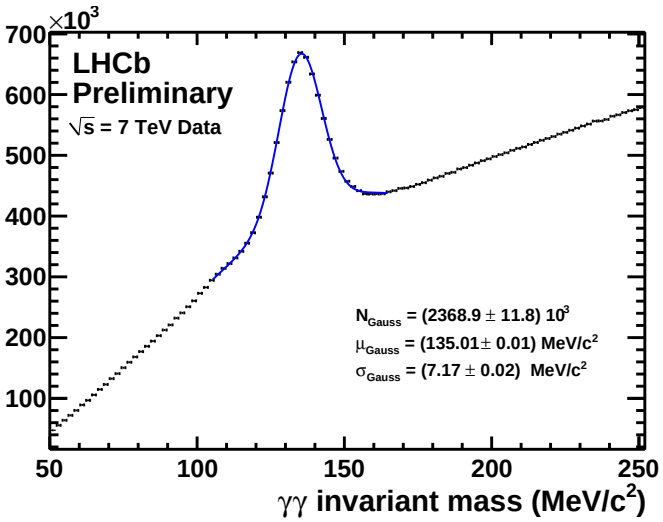

Figure 5.18: $\pi^0 \to \gamma\gamma$ reconstructed in the 2010 data, with a resolution of 7 MeV. The resolution expected at the time of the Technical Design Report was 5.7 MeV [82].

5.6 Summary

The LHCb detector has shown excellent performance during the 2010 data taking. The experiment has adapted well to the harsh running environment which it was not designed for. A testimony to the excellent performance of the detector are the measurements of the $b\bar{b}$, $c\bar{c}$ and open charm cross sections within less than a year of the nominal operation of the detector. The $b\bar{b}$ cross section has been measured at LHCb using semileptonic $B \to DX\mu\nu$ decays, $B \to D^*X\mu\nu$ decays and $B \to J/\psi X$ decays, and reported in [66, 84, 85] respectively while the $c\bar{c}$ and open charm cross section measurements are reported in [84, 86]. Given that the $c\bar{c}$ cross section is more than 20 times higher than $b\bar{b}$, CP violation and rare decays in the charm sector are also a part of the LHCb physics program.

The detector has already seen the first signals of B decay channels useful for CP violation analyses, like $B_s \to J/\psi\phi$ and radiative and electroweak penguin decays $B_s \to \phi\gamma$, $B_d \to K^*\gamma$ and $B_d \to K^{*0}\mu^+\mu^-$. The LHCb limit on the $B_s \to \mu\mu$ branching ratio has already reached the sensitivity of the current best limits [12, 13] and will surpass the latter soon after the start of data taking in 2011.

In this chapter we presented the performance of the sub detectors related to the reconstruction of radiative decays at LHCb. Before we discuss the radiative signal seen in the data, we describe the LHCb trigger, which is a very important part of the experiment. Again, emphasis will be on aspects relevant to the triggering of radiative decays.

Chapter 6

The LHCb trigger

6.1 Introduction

At nominal LHC running conditions, the rate of visible interactions[1] at LHCb is 10 MHz, while the write-to-tape rate of the detector is 2 kHz. The $b\bar{b}$ cross section is two orders of magnitude smaller than the total inelastic cross section at the LHC, and interesting B decays typically have branching ratios smaller than 10^{-4}. This makes a highly discriminating trigger a vital part of the experiment. The LHCb trigger is designed to reduce the rate from the visible interaction rate to 2 kHz, while keeping a high efficiency on B events and rejecting the overwhelming backgrounds.

The LHCb trigger is executed in two steps, one is called the Level 0 (L0) trigger which is implemented in the hardware. The next level is the High Level Trigger (HLT), which is software based. For the execution of the latter, the complete LHCb detector has to be read out, which can be done only up to a rate of 1 MHz. Therefore, the L0 trigger has to reduce the rate to 1 MHz, and the HLT then reduces it to 2 kHz.

[1] A visible interaction is defined as one in which at least two tracks are reconstructed in the LHCb acceptance

The L0 trigger decision is based on information from the calorimeter and the muon systems. The L0 calorimeter triggers select events with high energy photons, electrons and hadrons. The energy deposited in 2×2 clusters of calorimeter cells is added up and the cluster with the largest transverse energy is selected. The SPD, PS, ECAL and HCAL information is used to classify the clusters as photon, electron or hadron candidates. The L0 muon trigger selects two highest P_T muon candidates from each quadrant of the muon system. This is made possible by the stand alone momentum reconstruction of the muon chambers ($\sigma_{P_T} \sim 20\%$ [68]). The L0 calorimeter and muon triggers send this information to the L0 Decision Unit, which performs simple logic to combine this information into a trigger decision per crossing.

The HLT algorithms use the information from the full detector and are executed in the LHC*b* computing farm. The HLT is sub-divided into two stages, the HLT1 and HLT2. At the HLT1 stage, the rate is still too high to perform a complete reconstruction of the event, and the HLT1 algorithms mainly *confirm* the L0 candidates. The HLT1 is composed of several "alleys" to select events which have similar topology or final state particles. The alleys are Muon, Electromagnetic and Hadron, and the algorithms of a certain alley are executed if the relevant L0 trigger is fired. The concept of the LHC*b* trigger is illustrated in Fig. 6.1.

At the stage of HLT2, a complete reconstruction of the event is performed which is close but not identical to the offline reconstruction. This is due to timing constraints in the HLT2. So some reconstruction steps are simplified or omitted with respect to the offline, for example, a simplified detector description is used in the tracking algorithms and the RICH PID is calculated for only a sub set of tracks [87].

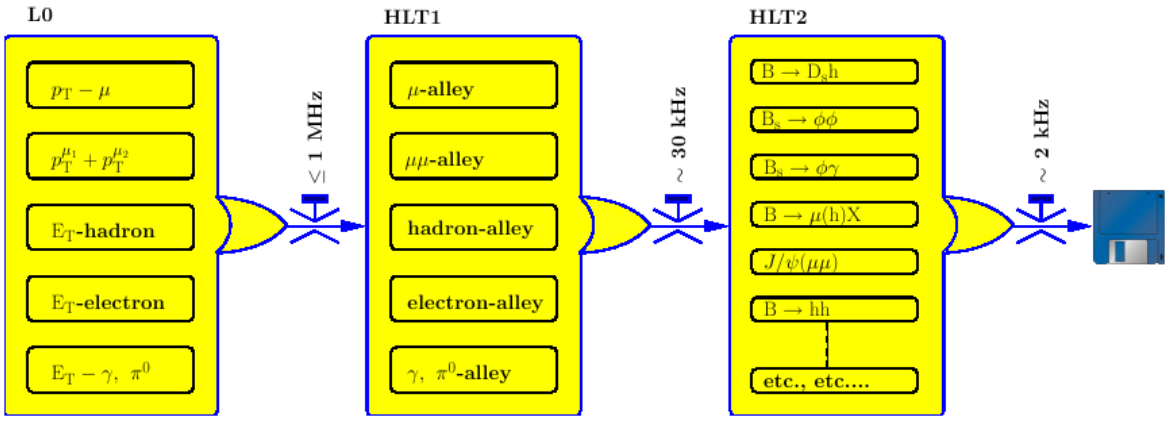

Figure 6.1: Flow of trigger algorithms in the LHC*b* trigger

The HLT2 algorithms include several algorithms (or HLT2 lines) dedicated to selecting a multitude of channels with similar final state particles or topologies, which are called *inclusive* lines. There are also some *exclusive* lines that attempt to reconstruct individual channels.

The radiative channels $B_s \to \phi\gamma$ and $B_d \to K^*\gamma$ are triggered mainly by the photon and electron triggers at the stage of L0. The high level triggers (HLT1 and 2) also have dedicated lines to trigger on radiative channels.

6.1.1 L0 calorimeter trigger for radiative decays

The basic idea of the L0 calorimeter trigger is to trigger on an interesting photon, electron or hadron candidate. There are a total of 6016 readout channels in the ECAL segmentation and 1488 in the HCAL segmentation. Each Front End (FE) board is connected to 32 channels (188 FE boards in total) and each board finds the highest energy "cluster" (2×2 cells) and sends it to the corresponding "Validation board". There are 28 validation boards, one for every 8 (6 or 7 in some cases) FE boards. A validation board receives

information about the hits in SPD and PS, using which it builds the photon, electron, π^0 and hadron candidates. There are a total of five types of L0 calorimeter candidates, and the highest P_T amongst each type is selected as the trigger candidate.

An ECAL candidate is identified as electron if either 1 or 2 of the four corresponding PS cells are above threshold, and an SPD cell in the corresponding area is hit. In the absence of an SPD hit, the candidate is classified as a photon. With this scheme, converted photons will be classified as electrons in the L0 trigger decision. Therefore, the radiative channels gain a substantial fraction of efficiency ($\sim$30%) by using the L0 electron trigger in addition to L0 photon, as reported in [88].

The other types of L0 calorimeter candidates are the π^0 and hadron candidates, and the former is further classified into local and global π^0. All L0 ECAL candidates are summarised in the following table.

Candidate type	Cluster size	SPD requirement	PS requirement
L0 photon	2×2	No hit in SPD	1 or 2 PS cells above threshold
L0 electron	2×2	A hit in SPD	1 or 2 PS cells above threshold
L0 local π^0	4×8	No requirement	At least 1 hit in front of the highest 2×2 cluster of the FE board
L0 global π^0	Two 2×2 clusters from adjacent FE boards	No requirement	No requirement

Table 6.1: Summary of L0 ECAL trigger candidates

The HCAL (hadron) candidates are built by looking for an ECAL candidate geometrically in front of the HCAL candidate, and adding the ECAL energy to the latter.

Each type of L0 calorimeter candidates has a selection card, and the information from all the validation boards is sent to these cards. So, each selection card receives 28 candi-

dates. It chooses the highest E_T one and sends it to the L0 Decision Unit, which makes a trigger decision per crossing, using information from all L0 triggers.

Only the L0 photon and electron triggers are considered relevant for triggering radiative decays [88]. The reasons for that are that the L0 hadron trigger was typically expected to have quite a high threshold on the hadron P_T, and hence was not expected to give a lot of efficiency on radiative decays. Another reason for not considering the L0 hadron trigger is that the rate and processing time of the dedicated radiative HLT1 algorithms cannot be sustained if they are run starting from an L0 hadron decision, in addition to the L0 photon and L0 electron decisions [88].

6.1.2 HLT for radiative decays

HLT1 for radiative decays

The HLT1 electromagnetic "alley" is a set of algorithms dedicated to select radiative decays. The Photon lines of this alley were developed to retain maximum possible efficiency on offline selected events[2], while keeping the background rejection high and is detailed in [88]. As described earlier, the L0 electron also contributes a substantial part to the efficiency on radiative signals, the HLT1 photon lines were executed if L0 electron or L0 photon trigger was fired. The efficiency of the HLT1 dedicated photon lines on offline selected $B_s \to \phi\gamma$ events is listed in 6.1.2, and the efficiency was similar on $B_d \to K^*\gamma$ signal events.

The reason for developing dedicated photon lines was that out of the other HLT1 alleys, the Muon alley did not give any substantial efficiency for radiative signals, as it triggers

[2]For the trigger studies, the efficiency is measured on the events that can be reconstructed with offline selection cuts which are listed in Table 8.1. The signal events that are reconstructed in LHCb and pass these cuts will be referred to as "offline selected" events.

Trigger Decision	A: L0 Photon	B: L0 Electron	A OR B
L0	35%	21.9%	54.1%
L0×HLT1	25.5%	14.9%	39.7%

Table 6.2: L0 and HLT1 efficiencies for offline selected $B_s \to \phi\gamma$ events where the L0 photon and electron thresholds were 2.3 GeV and 2.6 GeV respectively (Table taken from [88]).

on the presence of high P_T muons. The HLT1 hadron lines envisaged hard cuts on P_T and IP of the tracks. The efficiency of the former cut on final state hadrons in radiative decays is quite low. In addition to that, these cuts have non trivial effects on proper time acceptance, and were avoid as much as possible in the dedicated HLT1 photon lines.

HLT2 for radiative decays

Dedicated HLT2 lines to select $B_s \to \phi\gamma$ and $B_d \to K^*\gamma$ were developed by the author [1], the emphasis being on maximum possible efficiency on offline selected signal events, low background retention and avoiding proper time biasing cuts. These algorithms attempt to reconstruct all the final state particles in the decays and perform a vertex fit.

The reconstruction in HLT2 is a faster version of the offline reconstruction, therefore, some resolution effects in the reconstructed quantities are expected in HLT2 with respect to offline reconstruction. For this reason, the cut values in HLT2 radiative lines were chosen to be relaxed with respect to the offline cut values (Table 8.1). Therefore, this trigger should ideally retain 100% efficiency on signal events which can be selected offline and are passed by the L0 and HLT1 triggers. However, the signal efficiency of the lines was found to be 90% for $B_s \to \phi\gamma$ and 70% for $B_d \to K^*\gamma$ signal events respectively [1]. This is due to the lower track finding efficiency in HLT2 with respect to the offline track finding.

6.2 Summary

The trigger strategy for radiative decays at LHCb is the following

- L0 photon threshold $> 2.8\,\text{GeV}$ [88]
- L0 electron threshold $> 2.6\,\text{GeV}$ [88]
- Dedicated HLT1 radiative lines [88]: start from an L0 photon or L0 electron trigger. Photon $P_T > 2.5\,\text{GeV}$, Track IP $> 0.15\,\text{mm}$ and Track $P_T > 650\,\text{MeV}$
- Dedicated HLT2 radiative lines [1]: reconstruct the entire decay chain, applying relaxed cut values with respect to the offline selection. (Table 8.1).

Using estimates of efficiencies from these trigger configurations and offline selection cuts, the number of reconstructed $B_s \to \phi\gamma$ and $B_d \to K^*\gamma$ events expected for $2\,\text{fb}^{-1}$ at LHCb was calculated to be 11k and 68k respectively. The B/S ratio was calculated to be $<$0.55 at 90% CL for $B_s \to \phi\gamma$ signal and 0.6$\pm$0.16 for $B_d \to K^*\gamma$ signal [71][3].

In the next chapter, we describe the trigger evolution during the 2010 LHCb data taking, relevant to radiative decays and present the $B_d \to K^*\gamma$ and $B_s \to \phi\gamma$ signal from the 2010 data.

[3] These estimates were made with a simulation at $\sqrt{s}$ =14 TeV.

Chapter 7

Radiative signal in the 2010 data set

As noted previously, LHCb was optimized to run at a luminosity of $2{\times}10^{32}$ cm^{2}s^{-1}, and a Poisson probability μ of a visible pp interaction per bunch crossing of 0.4. The trigger strategy was also developed to run the detector at such conditions. In 2010 however, the running conditions were much harder, with the $\mu \sim$ 1.7-2.5 as shown in Fig. 7.1.

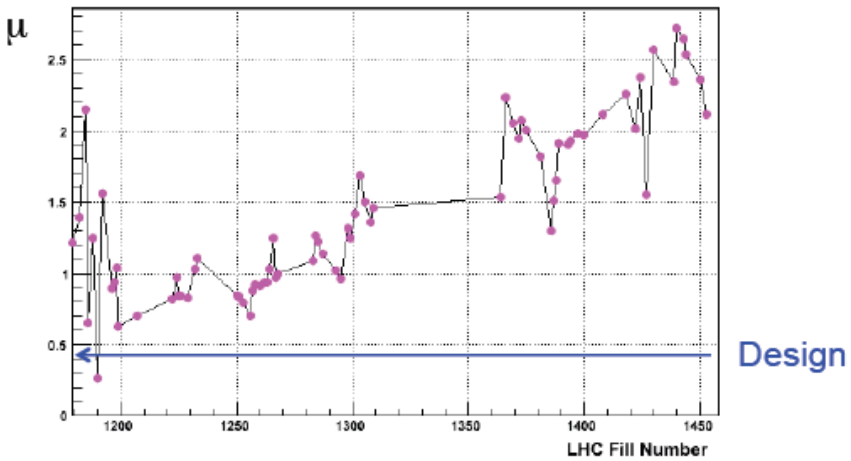

Figure 7.1: The evolution of μ at LHCb during the 2010 data taking (Figure from [89]).

The higher μ results in higher multiplicity events, so the Global Event Cuts (GECs) were introduced in the trigger to veto high occupancy (or multiplicity) events. Such events are relatively difficult to reconstruct in the HLT and consume more time per event. Such events are also important for the L0, since one needs to control not only the input rate

from L0 to HLT, but also the event size. This is because the L0 bandwidth is limited and the maximum rate at which the detector can be read out depends on the event size, which depends on the multiplicity in the event. High multiplicity events can be rejected by cutting on simple variables like the SPD multiplicity at the stage of L0 trigger, since the total number of SPD hits provides a fast indication of the track multiplicity in the event.

Fig. 7.2 shows the correlation between μ and the event size for different values of the SPD multiplicity cut. The event size (or occupancy) does not depend on μ if a cut of < 450 is applied on the SPD, which is important for maintaining a constant L0 and HLT output rate. Other GECs can be made in the HLT stages, like the number of VELO tracks, and the number of OT and IT clusters.

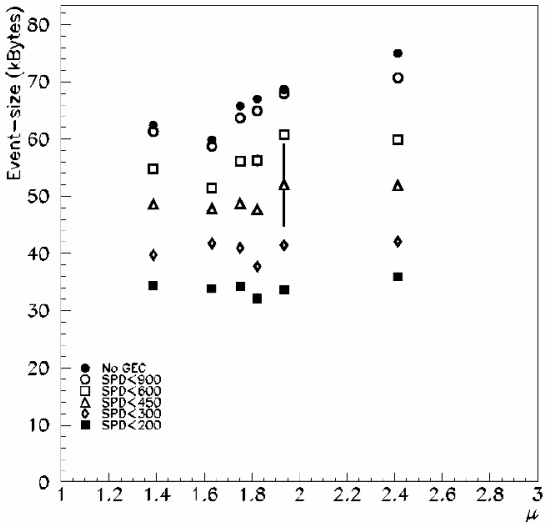

Figure 7.2: Event size as a function of μ, for different values of SPD multiplicity cut. For a cut of < 450 or harder on the SPD multiplicity, the event size or occupancy is almost independent of μ, which is important for maintaining constant output rate from L0 and HLT.

Changes were also made to the trigger to cope with the rate; the L0 thresholds were increased and the HLT1 and HLT2 selections were tightened to fit the trigger output into the 2 kHz LHCb write-to-tape rate. Some parts of the trigger, for example the L0 and

HLT Muon triggers remained almost unchanged with respect to their Monte Carlo tuning, while the L0 Hadron, Electron and Photon thresholds were increased by a few 100 MeV. Other changes in HLT1 and HLT2 specific to radiative decays and their effect on the trigger efficiency on signal will be discussed later in this chapter.

As described in Chapter 5, the LHCb detector has performed exceedingly well in the running environment of 2010, and Figs. 7.3 and 7.4 show respectively the $B_d \to K^*\gamma$ and $B_s \to \phi\gamma$ signals from the entire data set of 2010, where the ϕ and K^* are reconstructed in their K^+K^- and $K^+\pi^-$ modes respectively. The distributions have been fitted with a Gaussian and an exponential for signal and background components respectively, and no fit parameters were fixed.

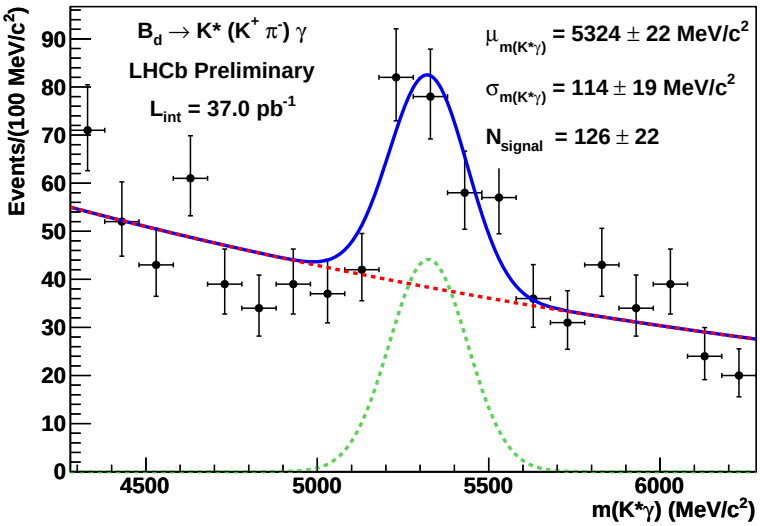

Figure 7.3: The $B_d \to K^*\gamma$ signal from the entire 2010 data set, corresponding to about 37 pb^{-1} of integrated luminosity.

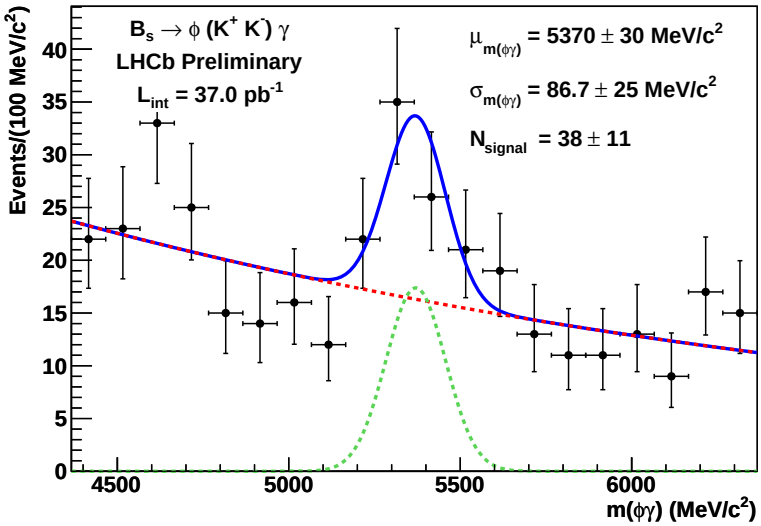

Figure 7.4: The $B_s \to \phi\gamma$ signal from the entire 2010 data set, corresponding to about $37\,\mathrm{pb}^{-1}$ of integrated luminosity.

Due to the low statistics for $B_s \to \phi\gamma$ channel, we will discuss only the $B_d \to K^*\gamma$ signal in the rest of this chapter.

7.1 Trigger evolution in 2010

During the 2010 operation of the LHC, the experiments were required to be ready to handle the increasing μ (Fig. 7.1), in order to maximize the integrated luminosity. At LHCb, different configurations or recipes of the trigger were prepared to cope with different running conditions. These are called the trigger configuration keys or TCKs. They were introduced so that during data taking, the person on duty in the LHCb control room is able to switch to a trigger configuration suitable for the LHC running condition without requiring a new release of the trigger software. The TCK is a 32 bit number that defines the sequence of algorithms and the cuts that were made in those algorithms [90]. The TCK is the only way to reproduce fully a certain trigger condition, as it encodes complete information about the entire trigger chain. Some important and relevant items of information are

- The GEC values, e.g. the cut on SPD multiplicity
- The thresholds and pre/post scales for all L0 triggers
- The cuts made in the HLT reconstruction algorithms, e.g. in the tracking
- The list of HLT lines that were run as part of that configuration
- The various cuts/thresholds and pre/post scales for all HLT lines

In Table. 7.1 we list the TCKs used during the 2010 data taking, along with their corresponding luminosities. Also listed are the P_T thresholds for the L0 electron, photon and hadron triggers.

Number	TCK	Luminosity(nb^{-1})	SPD cut	L0e	L0γ	L0Hadron
1	0x1D0030	157.4	900	3000	4400	2600
2	0x1F0031	102.2	450	3000	4400	3600
3	0x1E0030	2117.7	900	3000	4400	2600
4	0x1F0029	3078.8	900	3000	4400	3600
5	0x24002A	1212.6	900	3000	3200	3600
6	0x24002C	1356.9	450	3000	3200	3600
7	0x25002A	35.2	900	3000	3200	3600
8	0x25002C	1946.2	450	3000	3200	3600
9	0x2B002A	1839.1	900	3000	3200	3600
10	0x2A002A	4179.1	900	3000	3200	3600
11	0x2A002C	468.5	450	3000	3200	3600
12	0x2E002C	8911.2	450	3000	3200	3600
13	0x2E002A	8668.9	900	3000	3200	3600
14	0x2D002B	2.5	900	3000	3200	3600

Table 7.1: List of the TCKs and their corresponding luminosity for the 2010 data set. The P_T thresholds for the L0 electron, photon and hadron triggers are given in MeV.

The bulk of the 2010 data sample was taken with TCKs 5-14 of Table. 7.1, which corresponds to about $28.6\,\mathrm{pb}^{-1}$ of integrated luminosity. For this part of data taking, the HLT2 tracking algorithms had a cut of P_T/P of $> 500/5000\,\mathrm{MeV}$ on all tracks, i.e. no

tracks below these thresholds were reconstructed. Also, the dedicated "radiative" HLT1 lines as described earlier were turned off for these TCKs, and the only HLT1 line relevant to radiative decays was the "HLT1TrackPhoton" line [87]. This line or algorithm was executed only if the L0 photon trigger was fired and it tried to find one "good" track in the event fulfilling the criteria in Table 7.2. This HLT1 line is very similar to the ones developed for the dedicated radiative HLT1 alley. However, the P, P_T and IPχ^2 cuts in this line are quite hard and result in loss of efficiency[1], but these cuts were unavoidable for the reasons of background rejection and time available for the trigger decision. Also note that this line is executed only if the L0 Photon trigger is fired whereas previously, the Radiative HLT1 lines were designed to start from both L0 Photon and L0 Electron triggers.

The "HLT1TrackPhoton" line also requires that the track left at least 9 hits in the VELO and that the number of missing hits is less than 3. The latter number is calculated by using the VELO geometry and track angle, and predicting how many hits are expected for such a track. The number of missing hits is then the observed number of hits subtracted from the expected number. These cuts are useful in rejecting ghost tracks [87].

IP	PT	P	Track χ^2/dof	Track $IP\,\chi^2$	Missing Velo hits	Velo hits
> 0.13 mm	> 800 MeV	> 8000 MeV	< 5	> 50	< 3	>9

Table 7.2: Cuts made in the "HLT1TrackPhoton" line [87].

It should be noted that some choices during the 2010 running were motivated by the partial HLT computing farm available during that time [87], apart from the harsh running conditions of the LHC machine. The full HLT farm which is available for the 2011 running, contains approximately 20,000 processor cores. For an L0 output rate of 1 MHz, this translates into a computing time of 20 ms per event, and this time has to be shared

[1]We quote efficiency on events passed by the offline selection cuts (Table 8.1), and these HLT1 cut values are harder compared to offline values.

by HLT1 and HLT2. Only a fraction of this farm (about 4400 cores) was available in 2010, which limited the L0 output rate to about 200 kHz for the same timing of the HLT algorithms [87]. This is why L0 thresholds were increased by a few 100 MeV; in particular, the L0 Photon threshold was 3200 MeV for most of the data taking, while it was earlier foreseen to be about 2600 - 2800 MeV.

The 2011 trigger optimization is ongoing and the author played an active part and provided many inputs from the radiative decays perspective. The studies towards understanding the L0 Photon trigger performance using the $B_d \to K^*\gamma$ signal from data will be reported in this chapter.

As we described above, TCKs 5-14 are very similar in terms of L0 thresholds, tracking and GEC cuts. Therefore, for the sake of simplicity, only this subset of the 2010 data set (corresponding to 28.6 pb^{-1}) will be referred to as "data", unless specified explicitly.

7.2 Efficiency on signal and yield expectation

We evaluate the signal efficiency of a trigger representing TCKs 5-14 using the full LHC*b* simulation. For this study we used 10 M $B_d \to K^*\gamma$ signal events (5 M in each magnet polarity), generated within the LHC*b* detector acceptance and with the latest knowledge of the detector alignment, as measured in the 2010 data. This simulation was generated with a μ of 1.75 to emulate the data taking conditions in 2010, however, this μ is still significantly lower than what the detector was operated at, especially towards the end of the 2010 run (Fig. 7.1).

The offline selection cuts listed in Table 8.1 select about 166.5k events out of the 10 M

we started with. We also apply cuts made in the trigger chain that are additional to or harder than the offline criteria (the "trigger cuts"):

- L0: The photon P_T cut is $> 3200\,\text{MeV}$. This trigger accepts only unconverted photons. i.e. there should be no SPD hit in front of the ECAL cluster (Table. 6.1).
- HLT1: At least one of the tracks (K or π from the K^*) are required to have a P/P_T of $> 8000/800$ MeV
- HLT2: Both tracks are required to have a P/P_T of $> 5000/500$ MeV

Applying these cuts to the events which were passed by the offline criteria leaves us with 75.5k events. In LHCb jargon, the requirement that the trigger decision is made due to the presence of signal particles alone is called "Trigger On Signal" or TOS, so we require the events to have been TOSed by the relevant trigger chain[2]. Therefore, we are left with 35.3k events after all the offline and "trigger" cuts and TOS requirements, the mass distribution of which is shown in Fig. 7.5.

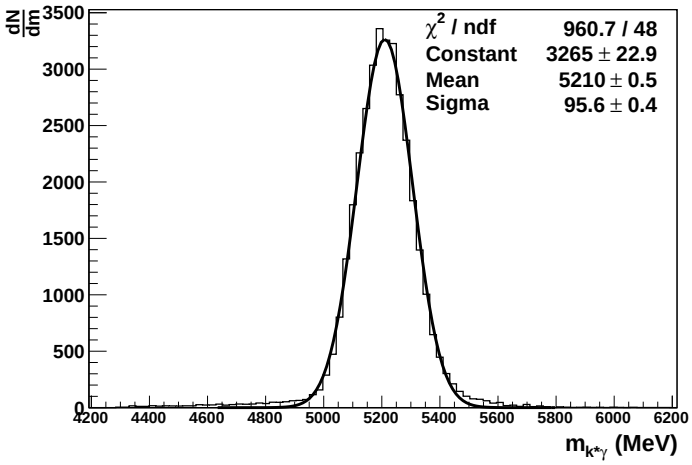

Figure 7.5: The invariant mass distribution of the $B_d \to K^*\gamma$ candidates from the signal MC sample, after all selections cuts and TOS requirement from the relevant triggers. A Gaussian function has been fitted to this distribution, however, the tails due to calorimeter calibration are not fitted very well by the function.

[2]the L0Photon line, the HLT1TrackPhoton line and the HLT2Bd2KstGamma line

Therefore, the efficiency of all the cuts and trigger[3] requirements on $B_d \to K^*\gamma$ signal events is about 0.35%. We calculate the expected yield of $B_d \to K^*\gamma$ in $28.6\,\text{pb}^{-1}$ of data using an efficiency of $\eta_{sel} = 0.0035$, the LHCb measurement of $\sigma_{b\bar{b}}$ inside the experiment's acceptance of $(75.3 \pm 5.4 \pm 13.0)\,\mu$b [66], the probability f_{B0}, for a b quark to hadronize into a $B0$ of 0.4 and $29{\times}10^{-6}$ for the visible branching ratio of $B_d \to K^*\gamma$ [71]:

$$\begin{aligned} \text{N} &= \mathcal{L} \times \sigma_{b\bar{b}} \times 2 \times f_{B0} \times BR_{\text{vis,B}_\text{d}\to\text{K}^*\gamma} \times \eta_{sel} \\ &= 28.6\,\text{pb}^{-1} \times (75.3 \times 10^6)\,\text{pb} \times 2 \times 0.4 \times (29 \times 10^{-6}) \times 0.0035 \\ &= 175 \end{aligned}$$

We therefore expect 175 ± 31 $B_d \to K^*\gamma$ signal events[4] from the data sample corresponding to $28.6\,\text{pb}^{-1}$. There is no prediction for the B/S from this MC sample due to limited statistics of minimum bias simulation available. Previously, it was estimated to be 0.6±0.16 [71].

7.3 $B_d \to K^*\gamma$ signal in data

Fig. 7.6 shows the distribution of the $K^*\gamma$ invariant mass from $28.6\,\text{pb}^{-1}$ of data, where all the offline selection cuts [71] and the additional trigger cuts (Section. 7.2) have been applied and a TOS from the L0 photon, HLT1TrackPhoton line and the HLT2 signal line has been required.

The distribution has been fitted with a Gaussian and an Exponential for signal and background respectively[5]. We observe 45 events from a data sample of $\sim$28.6 pb^{-1} where

[3] The TCK 0x2E002A was applied to the $B_d \to K^*\gamma$ MC sample. This TCK is quite representative of the TCK 4-15 in Table 7.1.

[4] The dominant errors are of $\sigma_{b\bar{b}}$ (18%) and luminosity (10%), so we quote an 18% error on 175.

[5] The fit is an unbinned maximum likelihood fit made with the RooFit package and none of the fit parameters were fixed.

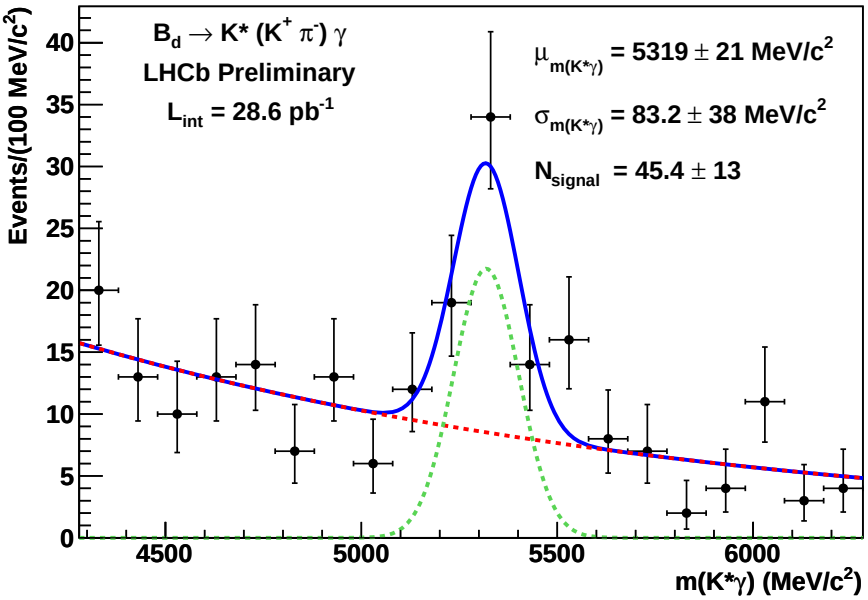

Figure 7.6: The invariant mass distribution of the $B_d \to K^*\gamma$ candidates from 28.6 pb^{-1} of data.

as the expectation from MC was 175 ± 31 events. This discrepancy will be discussed later in this chapter. The B/S calculated in ± 250 MeV around the fitted mean of 5319 MeV, is about 1.0. The mass resolution is (83 ± 38) MeV, which is compatible with the MC prediction (Fig. 7.5) of about 95 MeV.

In the following we investigate the issue of the lower yield further, by comparing the multiplicity seen in data to its distribution in simulation. The study described in the next section may also be relevant to the understanding of the worse B/S with respect to MC expectation, but this requires dedicated studies.

We will also discuss the L0 photon trigger, which is very important for radiative decays. Other signal decays like $B_d \to J/\psi K^*$ at LHCb have been found to have yields compatible with the MC predictions [91], which demonstrates that the trigger and reconstruction steps for charged particles are well modelled in simulation. The tracking performance has

been demonstrated to be in excellent agreement with expectations; the IP resolution has been validated using tracks from PV and the momentum resolution over a large invariant mass range has been validated using the various resonances like $J/\psi \to \mu\mu$ and two body hadronic B decays decays. The tracking efficiencies in the trigger and reconstruction have been determined using tag and probe method with J/ψ, Λ and K_s decays. However, there is no such evidence for the L0 Photon trigger, which is the main trigger for radiative decays. There is no standard candle/calibration channel to determine efficiencies for photon trigger and reconstruction and calorimeter calibration. Decays such as $\pi^0 \to \gamma\gamma$ do not provide photons in the momentum range we are interested in for $B_d \to K^*\gamma$ and $B_s \to \phi\gamma$, so these studies have to be done with signal decays themselves.

The optimization of the photon trigger and offline reconstruction is ongoing at the moment and in this chapter we discuss some initial studies which were provided as input to this process.

7.4 Data/MC comparison in SPD multiplicity

The reason for the discrepancy between data and MC, in the number of signal events can be due to the modelling of track multiplicity in the MC, because trigger and selection efficiencies are strong functions of the multiplicity in the event, as shown in Fig. 7.7.

The multiplicity seen in data has not been fully reproduced in the MC, as seen in Fig. 7.8 which shows the SPD multiplicity of the $B_d \to K^*\gamma$ MC sample (offline selection and the trigger TOS requirements made), and the background subtracted[6] distribution from the $B_d \to K^*\gamma$ events from data.

[6]For background subtraction, the SPD multiplicity distribution in the left and right sidebands is averaged and subtracted from the distribution in the signal mass window.

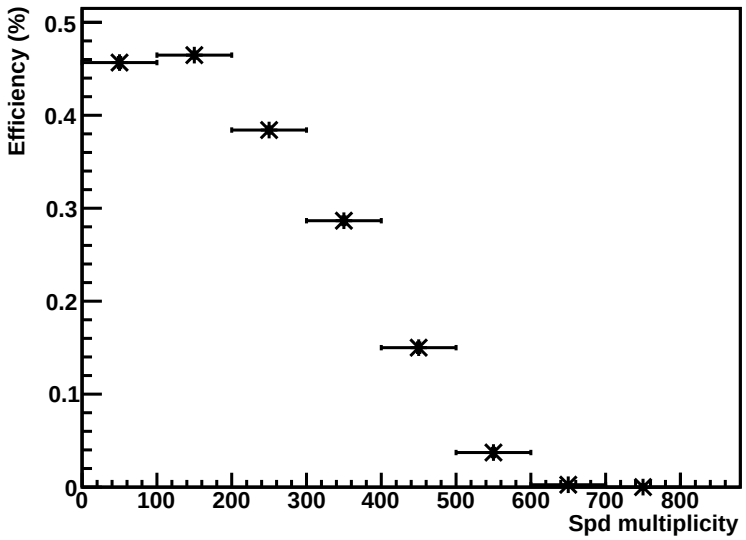

Figure 7.7: The combined efficiency of selection and trigger cuts, and the trigger TOS requirement on the generated $B_d \to K^*\gamma$ MC sample, as a function of SPD multiplicity. This sample was generated within the acceptance of the experiment, so no geometric efficiency is included here.

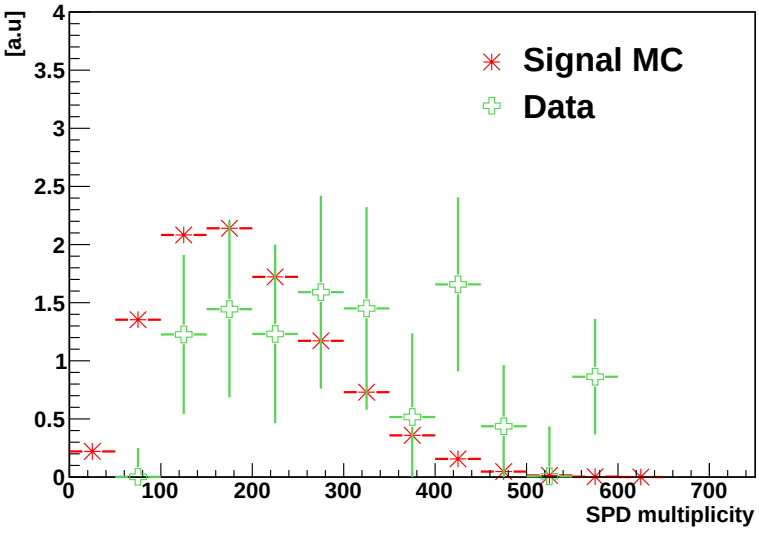

Figure 7.8: The SPD multiplicity distribution for $B_d \to K^*\gamma$ signal MC and background subtracted data, for which the signal window was chosen to be $\pm 250\,\text{MeV}$ around the fitted mean.

It in important to note here that out of the $28.6\,\mathrm{pb}^{-1}$, about 12.7 was taken with an SPD multiplicity < 450 cut while $16\,\mathrm{pb}^{-1}$ was taken with SPD multiplicity < 900. In the signal MC, there is a loss of $\sim 1\%$ of signal events if a cut of SPD multiplicity < 450 is applied. However, in data the signal events seem to have an almost flat distribution in the SPD multiplicity, and could have a long tail extending even beyond 900 (Fig. 7.8). We therefore separate the data samples taken with the two different SPD cuts and evaluate the expected signal yield for them.

The expected yields are $\mathcal{N}_{SPD\,450} = 78 \pm 14$ and $\mathcal{N}_{SPD\,900} = 98 \pm 18$ signal events (using Eq. 7.1) for the two sub-samples of data and their $K^*\gamma$ invariant mass distributions are plotted in Figs. 7.9 and 7.10 [7]. The results are summarised in Table 7.3.

SPD cut	MC expectation	Observed yield	$\frac{\mathcal{N}_{Expected}}{\mathcal{N}_{Observed}}$
<450	78 ± 14	15±5	5.2 ± 1.9
<900	98 ± 18	34±8	2.9 ± 0.87

Table 7.3: Observed and expected number of $B_d \to K^*\gamma$ signal events in the SPD < 450 and SPD < 900 sub-samples of the 2010 data.

The observed yields are incompatible with the MC predictions and no significant signal is observed in the SPD < 450 sample. We will therefore develop the study further using only the SPD < 900 sample.

[7] The distributions are after the application of all selections cuts and requiring the relevant triggers to be TOS on the $B_d \to K^*\gamma$ candidate. They have been fitted with a Gaussian and Exponential for signal and background respectively, and the width was fixed to the MC expectation of 95 MeV.

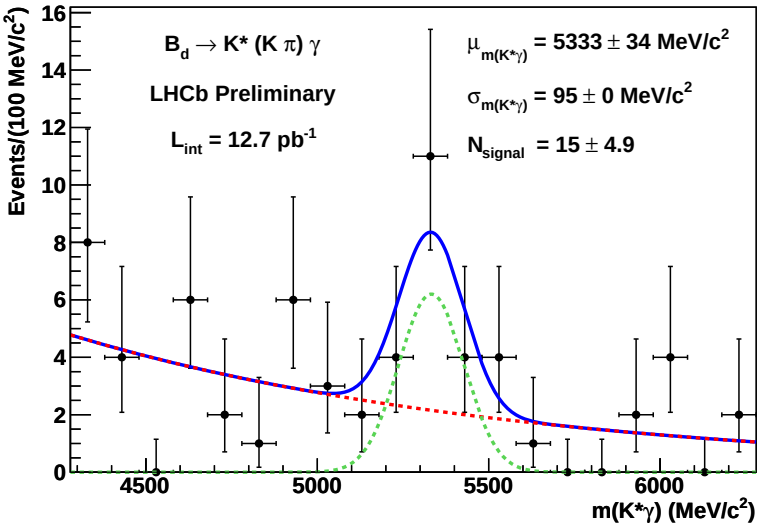

Figure 7.9: The invariant mass distribution of the $B_d \to K^*\gamma$ candidates from $12.7\,\mathrm{pb}^{-1}$ of data taken with a < 450 cut on the SPD.

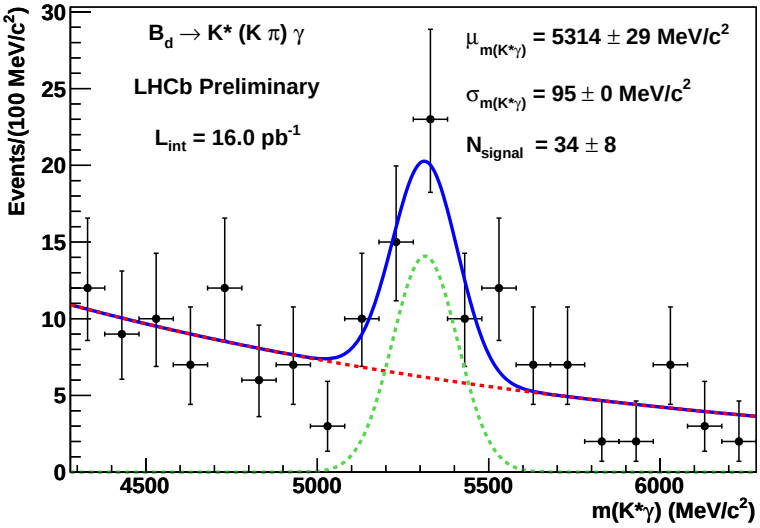

Figure 7.10: The invariant mass distribution of the $B_d \to K^*\gamma$ candidates from $16.0\,\mathrm{pb}^{-1}$ of data taken with a < 900 cut on the SPD.

7.4.1 Correction for SPD multiplicity

We investigate if the SPD multiplicity is the only cause of this yield discrepancy. To do so, we make an efficiency corrected distribution of the SPD multiplicity from data and measure the visible branching ratio of $B_d \to K^*\gamma$. Fig. 7.11 shows the background subtracted SPD

multiplicity distribution of the SPD < 900 sub-sample of data, compared to signal MC distribution.

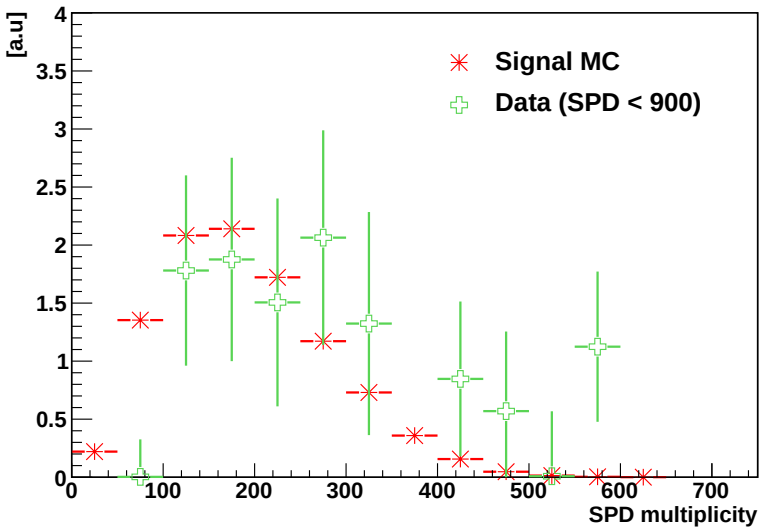

Figure 7.11: The SPD multiplicity distribution for $B_d \to K^*\gamma$ signal MC and background subtracted data with a < 900 cut on the SPD multiplicity. The signal mass window in data was chosen to be $\pm 250\,\mathrm{MeV}$ around the fitted mean.

The efficiency corrected distribution from data (Fig. 7.11) using the efficiency in Fig. 7.7 is plotted in Fig. 7.12. The integral of this corrected distribution is 21500 $\pm$ 5000 (we assign a 23% error, from the observed number of events, which was 34 $\pm$ 8), from which we *measure* $BR_{vis,B_d\to K^*\gamma}$ as

$$BR_{(SPD<900)} = \frac{21.5 \times 10^3}{16.0\ \mathrm{pb}^{-1} \times 75.3 \times 10^6\,\mathrm{pb} \times 2 \times 0.4} = 22.3 \times 10^{-6}$$

The taking into account the 23% error on the numerator and the dominant 18% error on $\sigma_{b\bar{b}}$ in the denominator, the error on the above calculated quantity is about 28%, therefore, $BR_{(SPD<900)} = (\ 22.3 \pm 6.2) \times 10^{-6}$.

The branching ratio of $B_d \to K^*\gamma$ is 29×10^{-6}, so after taking into account the observed SPD multiplicity distribution in data, the discrepancy in the observed and predicted signal

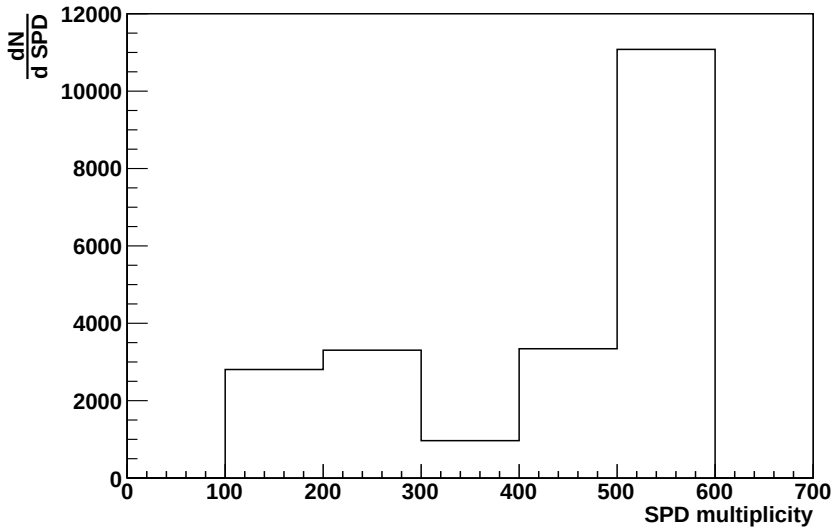

Figure 7.12: Efficiency corrected SPD multiplicity distribution of the data (Fig. 7.11). The integral of this distribution is 21.5 k.

events of $B_d \to K^*\gamma$ becomes 1.3 ± 0.36 for the SPD < 900 sample. This discrepancy was 2.9 ± 0.87 before taking this effect into account (Table 7.3). Due to the small statistics, and consequently the large error, it is hard to conclude from the predicted/observed ratio of 1.3 ± 0.36 if the discrepancy was only due to the multiplicity distribution of the events in data or some other source as well.

The other aspect that can have a large bearing on the radiative signal yield is the L0 photon trigger, the main L0 trigger for radiative decays. This will be motivated in the next section, in which we present some studies to validate the L0 photon performance with data.

7.5 Validation of L0 photon trigger in data

Before stating the more technical aspects of the discussion, we recall the strategy to trigger and select $B_d \to K^*\gamma$ events at LHCb. With the modifications made to the trigger

chain for the 2010 data taking, the strategy was to use only the L0 Photon trigger and "HLT1TrackPhotonLine" at HLT1. The HLT2 selections have remained essentially the same as described in Chapter 6, so has the offline selection strategy.

An inefficiency in any of these trigger and selection steps that is unaccounted for in the MC can be the reason for this observed data/MC discrepancy of the $B_d \to K^*\gamma$ yield. The performance of HLT tracking has been validated on data as discussed in Chapter 5 and the same is true for offline selections [91] which gives confidence in the MC simulation of the HLT1, 2 and offline cut variables related to charged particle reconstruction. The L0 Photon trigger and the offline photon reconstruction efficiency remain to be validated. Both of these can be studied using $B_d \to K^*\gamma$ signal events coming from the hadron lines of L0 and HLT, but this study needs more statistics than we have used for this thesis. In the next sections, we study the L0 Photon trigger efficiency which can be studied using Minimum bias events as well. Before we describe the method, we remind the reader of two important points regarding the implementation of this trigger:

1. The L0 photon triggers only on unconverted photons, which are defined in the next section. Important to note here is that the proportion of Unconverted photons in the entire signal sample is very difficult to model in simulation, especially due to the material between the magnet and the calorimeter system. This may have a sizeable contribution in the discrepancy of observed v/s predicted signal events.

2. This trigger requires either 1 or 2 Preshower cells above threshold in front of the trigger candidate (Table. 6.1). Both the number of Preshower cells and the threshold tuning was MC driven and may not be optimal for data.

We will use only offline reconstructed and unconverted photons to evaluate the efficiency of L0 Photon trigger, hence point (1) above does not have a significant impact on the re-

sults of this study. However, point (2) above is still a concern, given the high multiplicity environment the detector is operating in.

In the following, we estimate the efficiency of the L0 Photon trigger from data themselves and compare it to the MC efficiency. The signal and Minimum bias simulation used here was generated with a μ of 1.75, and the trigger corresponding to TCK "0x2E002A " was applied to it.

7.5.1 Event samples used

We use three samples for the L0 photon efficiency discussion:

- The $B_d \to K^*\gamma$ signal MC sample, where a loose selection for $B_d \to K^*\gamma$ decays has been applied. For the exercise here, this serves as a sample of "signal" photons.

- The Minimum bias (MB) sample from the same MC production as above, where it is required that a photon with $P_T > 2800\,MeV$ is found by the offline reconstruction.

- The MB sample from data, where it is required that a photon with $P_T > 2800\,MeV$ is found by the offline reconstruction. Note that for this study we have used only the data taken with TCK "0x2E002A ", which was applied to the MC samples.

In the signal sample, there are no events with more than one "offline" photon candidates per event. In the MB samples from simulation and data however, it is quite likely that there are multiple photon candidates per event, since in these samples the photon candidates almost always result from π^0 decays. For such situations, we randomly choose one offline photon candidate from each event. This is to avoid double counting of high multiplicity events in our distributions, since they are more likely to have more than one photon candidate.

7.5.2 "Unconverted" photons

In the following discussion, we will use *offline reconstructed and Unconverted* photon candidates since the L0 Photon triggers only on *Unconverted* photons. In LHC*b* jargon, Unconverted photons are defined as ones which did not leave a hit in the SPD. At the L0 trigger level, where the photon candidate is built from 2×2 calorimeter cells, it is required that there is no hit in any of the 4 SPD cells geometrically in front of the cluster. In the offline reconstruction, the photon candidate is built from 3×3 cells and for a photon to be unconverted, it is required that there is no hit in any of the 9 corresponding SPD cells. Also note that in the current implementation of the L0 and offline clustering, while it is likely that the 2×2 L0 cluster is a subset of the 3×3 offline cluster, it is not guaranteed to be so. This is an important point because the "no SPD hit" requirement at L0 and offline stages of photon making can cause a relative inefficiency between the two stages.

7.5.3 Photons and π^0 content of samples

While the signal MC sample contains "true" photons, the photons in Minimum bias samples (from MC and data) usually result from π^0 decays. However, it is important to note that the purpose of this study is to determine the efficiency of the L0 photon trigger over an object that can be reconstructed offline as an Unconverted photon. Considering the description of the offline and L0 photon building (Section. 7.5.2 and Table. 6.1 of Chapter 6) we assume that a candidate that was reconstructed as an offline Unconverted photon should have triggered the L0 photon trigger as well. Hence, we determine the L0 photon efficiency using the above described samples.

7.5.4 L0 Photon efficiency

To evaluate the L0 Photon trigger efficiency in each sample, we require the L0 Photon TOS on each of the offline reconstructed photons in the sample. In Fig. 7.13 the P_T distribution of the offline reconstructed photons in the $B_d \to K^*\gamma$ signal MC sample is shown by the solid lines. The open squares show the distribution for the candidates from the same MC sample, which were triggered by the L0 Photon trigger (TOS). Fig. 7.14 shows the efficiency of the L0 Photon trigger which has been fitted with an Erf function.

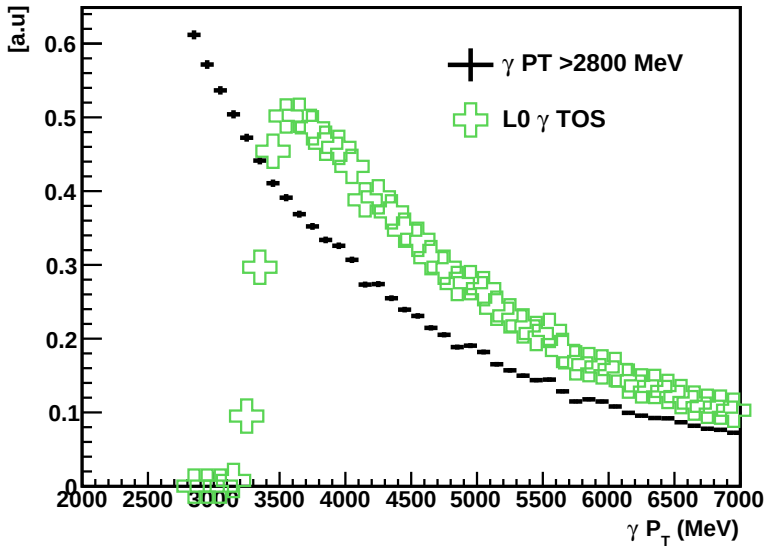

Figure 7.13: From $B_d \to K^*\gamma$ MC signal sample: P_T distribution of the offline reconstructed photons (solid lines) and the ones triggered by L0 Photon (open crosses). Both histograms have been normalized arbitarily, to be shown on the same scale.

We define 'offset' as the difference between the point along the turn on where the efficiency is 50% of its maximum value, and the L0 Photon P_T threshold. With this definition, the 'offset' can be expected to be positive because the L0 photon clustering is 2×2 while the offline uses 3×3 clusters. The L0 Photon threshold was 3200 MeV for the TCK that was applied to this signal MC sample, and the point along P_T where the efficiency rose to 50% of its maximum value was 3358 MeV in this case. So the offset is

3358-3200, or about $\sim 150\,\text{MeV}$ and the photon P_T resolution is about $130\,\text{MeV}$.

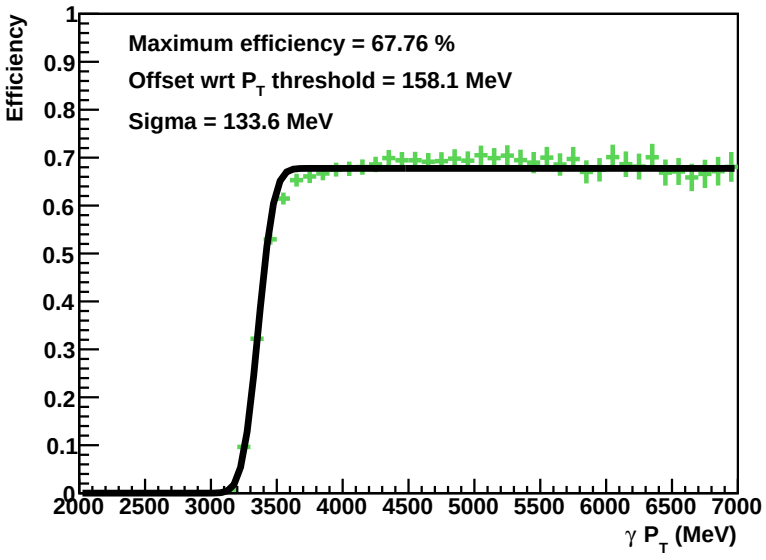

Figure 7.14: Efficiency of the L0 Photon (TOS) requirement on the offline reconstructed photons in the $B_d \to K^*\gamma$ signal MC, fitted with an Erf function.

Compare these to the L0 Photon efficiency parameters for the Minimum bias samples from MC and data, which are shown in Figs. 7.15 and 7.16 respectively.

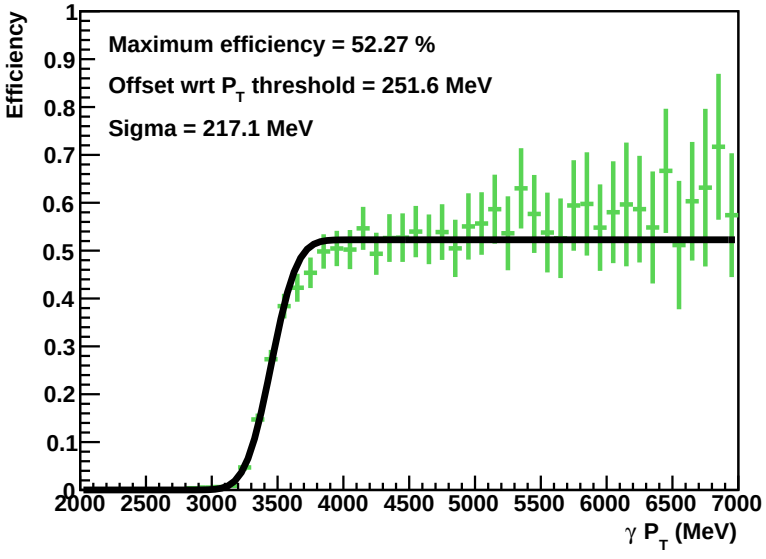

Figure 7.15: Efficiency of the L0 Photon (TOS) requirement on the offline reconstructed photons in the Minimum bias MC, fitted with an Erf function.

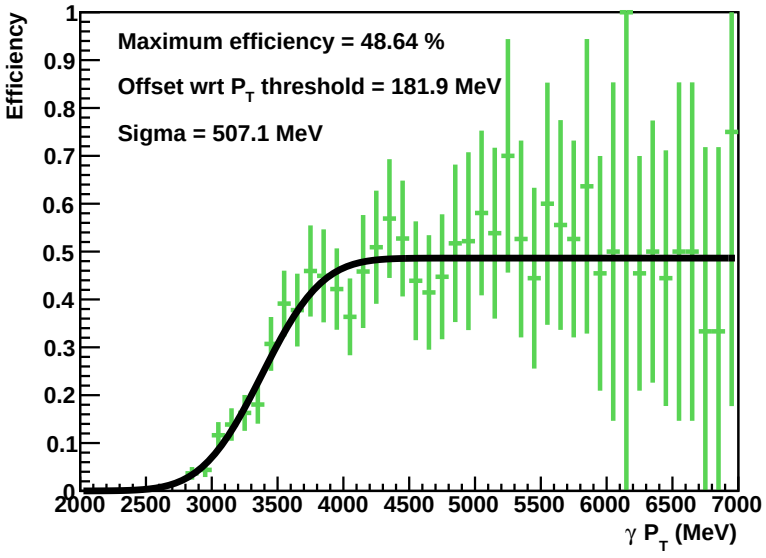

Figure 7.16: Efficiency of the L0 Photon (TOS) requirement on the offline reconstructed photons in the Minimum bias events in data, fitted with an Erf function.

Comparing the two Minimum bias samples, the L0 photon resolution is twice as large in data and the maximum efficiency, i.e. for very high P_T ($> 4000\,\text{MeV}$) photons is also smaller in the latter sample. These figures also show that not only is there a discrepancy between data and MC, there is some difference between the signal MC and Minimum bias MC samples as well.

The most probable cause for the latter is that the signal MC sample contains "true" photons while the Minimum bias MC sample mainly contains π^0s and other random clusters being reconstructed as photons. The "photon" candidates in the Minimum bias samples are therefore likely to have different behaviour in terms of the energy deposited and the number of Preshower cells above threshold as a result of that deposit, as compared to the photons from the signal MC sample.

A photon PID variable has been developed (Not by the author. See for example Ref. [88].) which is a multivariate combination of cluster-track matching χ^2, energy de-

posited in the SPD and Preshower detectors, and the ratio of the energy of the entire cluster and the energy of the cluster seed, designed to separate photons from merged π^0s. We use this variable to decrease the fraction of merged π^0s in the photon samples we selected. The distribution of this variable for the signal MC, Minimum bias MC and data is shown in Figs 7.18, 7.19 and 7.20 where for each sample of photons, we show the PID for the MC (un)matched photons and the ones TOSed by L0 Photon trigger[8].

In the offline reconstruction, the Preshower energy is added to the ECAL energy of the photon candidate. However, at the L0 level, the Preshower is operated as a counter reporting a hit if the energy deposit was above the threshold, which was $\sim 16\,\text{MeV}$ for the 2010 running. The distribution of this variable from $B_d \to K^*\gamma$ signal MC, for the MC (un)matched photons and the ones TOSed by L0 Photon trigger is shown in Fig. 7.17. This can also be a cause of inefficiency between an L0 photon and an offline photon, so we put a cut on the Preshower energy of $> 20\,\text{MeV}$ on the offline photon candidates.

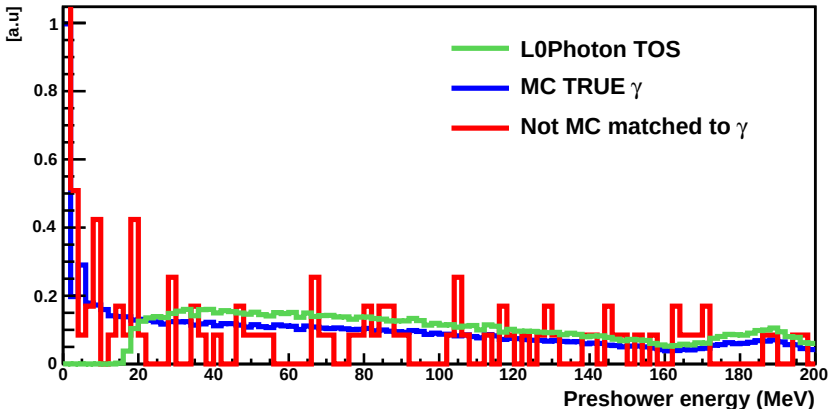

Figure 7.17: $B_d \to K^*\gamma$ signal MC: The distribution of the Preshower energy (MeV) for all photons with P_T above 2800 MeV (blue), the ones triggered by L0 Photon (green) and the photons not matched to an MC true photon (red).

[8]For Figs. 7.17 to 7.20 the histograms in the same figure are normalised to the same area.

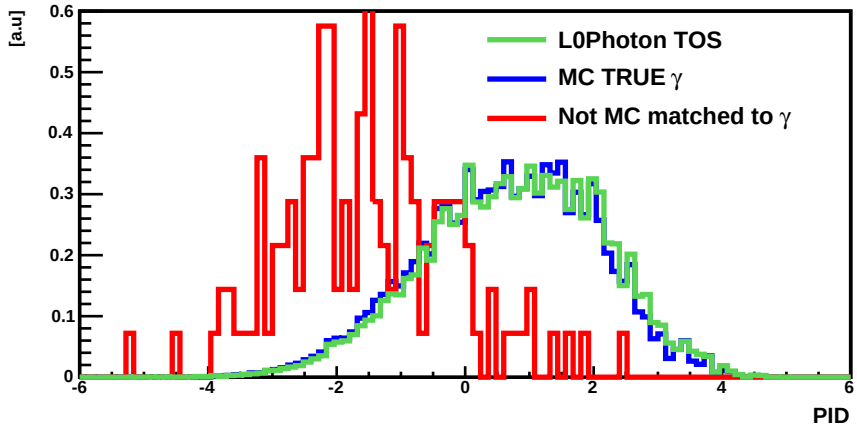

Figure 7.18: $B_d \to K^*\gamma$ signal MC: The distribution of the photon PID variable for all photons with P_T above 2800 MeV (blue), the ones triggered by L0 Photon (green) and the photons not matched to an MC true photon (red).

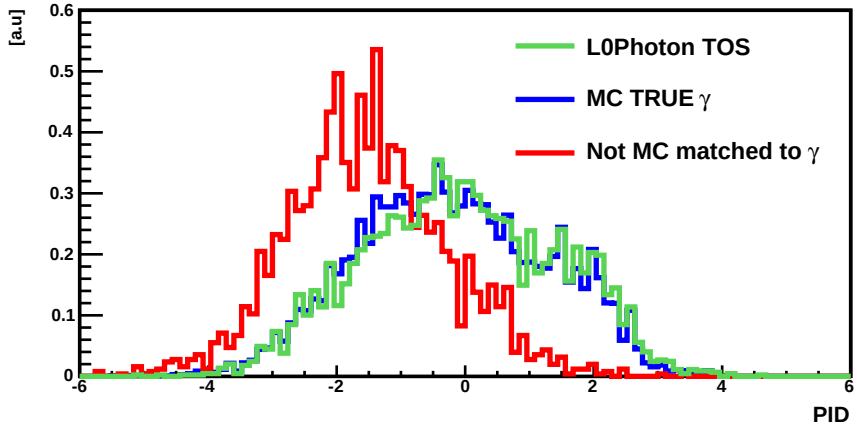

Figure 7.19: Minimum bias MC: The distribution of the photon PID variable for all photons with P_T above 2800 MeV (blue), the ones triggered by L0 Photon (green) and the photons not matched to an MC true photon (red).

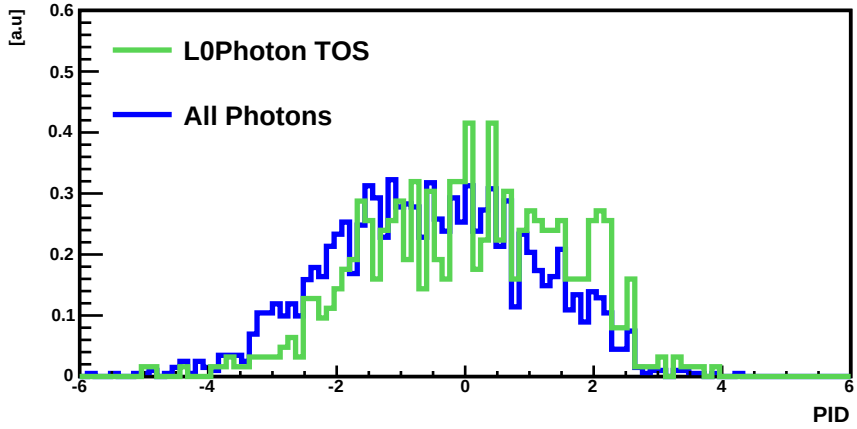

Figure 7.20: Minimum bias Data: The distribution of the photon PID variable for all photons with P_T above 2800 MeV (blue) and the ones triggered by L0 Photon (green).

For a cut of PID> 0 and Preshower energy > 20 MeV we achieve a purity of ∼98% in the Minimum bias MC sample, where purity is defined as the number of photons matched to an MC true photon, normalized to the total number of photons in the sample. Note that the MC matching here does not mean that the photon candidate did not come from a π^0, but only that it was not a hadronic or random cluster.

The results for the L0 Photon trigger efficiency on each of these samples after the application of "purity" cuts on the photons are summarised in Table 7.4.

Sample			L0 resolution	L0 offset	$\epsilon_{PT>4000MeV}$
Signal MC	1	γ_{PT} >2800 MeV	134 MeV	158 MeV	68%
	2	purity cuts	124 MeV	138 MeV	92%
Min Bias MC	3	γ_{PT} >2800 MeV	217 MeV	252 MeV	52%
	4	purity cuts	146 MeV	159 MeV	80%
Min Bias Data	5	γ_{PT} >2800 MeV	507 MeV	182 MeV	49%
	6	purity cuts	363 MeV	-28.3 MeV	69%

Table 7.4: Summary of the L0 photon efficiency on various MC and data samples. Note that the total efficiency (ϵ) of the different samples is not comparable because it depends on the photon P_T spectrum.

The "γ_{PT} >2800 MeV" rows in Table. 7.4 represent the efficiency parameters for the case where only this cut was applied to the particular sample (shown in Figs. 7.14 to 7.16) while the rows starting with "purity cuts" represent the cases where in addition to the γ_{PT} cut, the photon PID and Preshower energy cuts were also applied.

The difference in the efficiency parameters between rows 1 and 3, and 2 and 4 can be attributed to the possible contamination of the MB sample with π^0s, the clusters produced by which have different topology than the ones produced by photons. Given that there are subtle difference between how a photon candidate is built offline and at the L0 trigger level, these topology differences could play a role to cause the efficiencies to differ.

Another cause of the lower efficiency in Minimum bias MC sample wrt the signal MC sample can be the difference in their SPD multiplicity distributions, which are shown in Fig. 7.21.

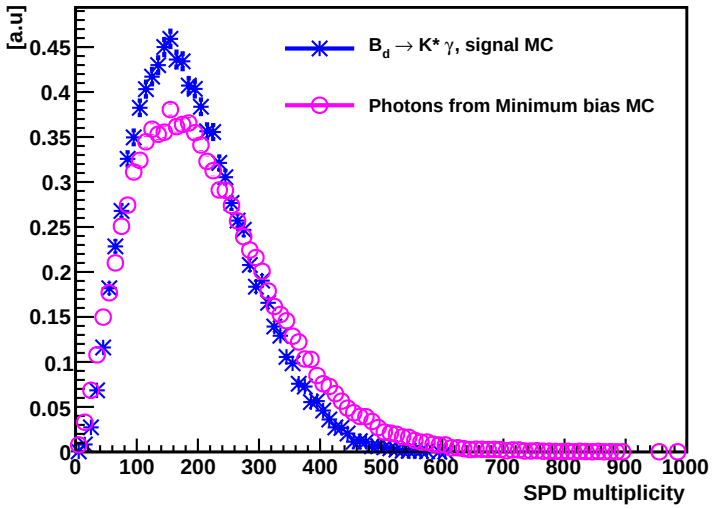

Figure 7.21: The SPD multiplicity in the selected and triggered $B_d \to K^*\gamma$ signal MC and the Minimum bias MC sample.

The same can be the cause for the difference in the L0 Photon performance in Minimum bias in Data and MC (rows 3 and 5, and 4 and 6 in Table 7.4). The SPD multiplicity distribution of two samples before and after the purity cuts are shown in Fig. 7.22.

An important point to note here is that the L0 Photon efficiency as a function of SPD multiplicity is also not modelled very well in MC as shown in Fig. 7.23. In data, the efficiency drops by about 30% as the SPD multiplicity becomes > 400, while in MC it stays almost flat for this range. Note here that the data and MC Minimum bias samples might have a different response to the requirement of the Preshower energy deposit and number of cells. As mentioned earlier, it is difficult to model the development of the energy deposit by photons, due to the presence of material upstream of the calorimeters.

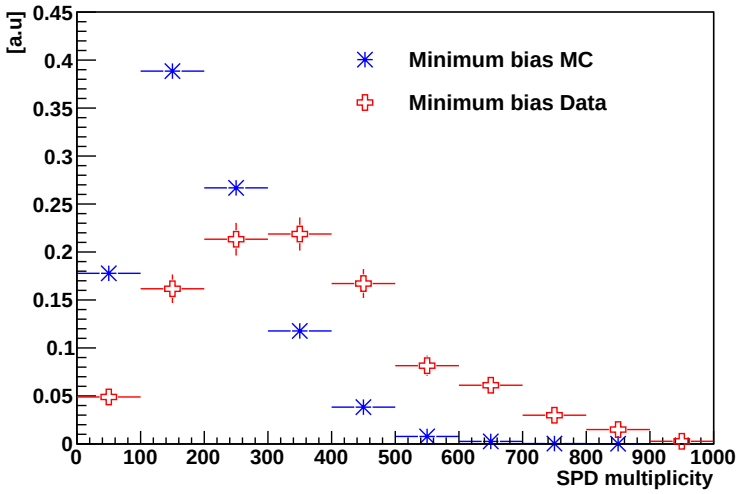

Figure 7.22: The SPD multiplicity distribution of the events where at least one high P_T photon was reconstructed offline, from Minimum bias Data and MC samples.

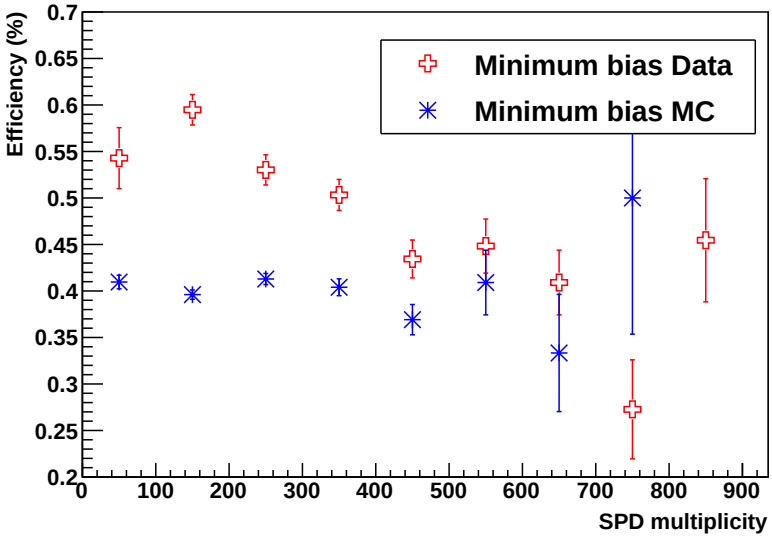

Figure 7.23: Efficiency of the L0 Photon trigger on the offline selected photons in the Minimum bias sample from Data and MC. The Photon P_T, PID and Preshower energy cuts have been applied to the offline photons in each bin, and the efficiency for the L0 Photon trigger to have TOSed the candidate is shown.

However, the efficiency in data seems to be higher than predicted in MC. The P_T spectrum of the photons in the two samples is very similar, as shown in Fig. 7.24, so this difference in the total efficiency (Fig. 7.23) is likely to be due to the larger width of the

L0 Photon efficiency curve in data as compared to MC, since the plateau is lower in the former.

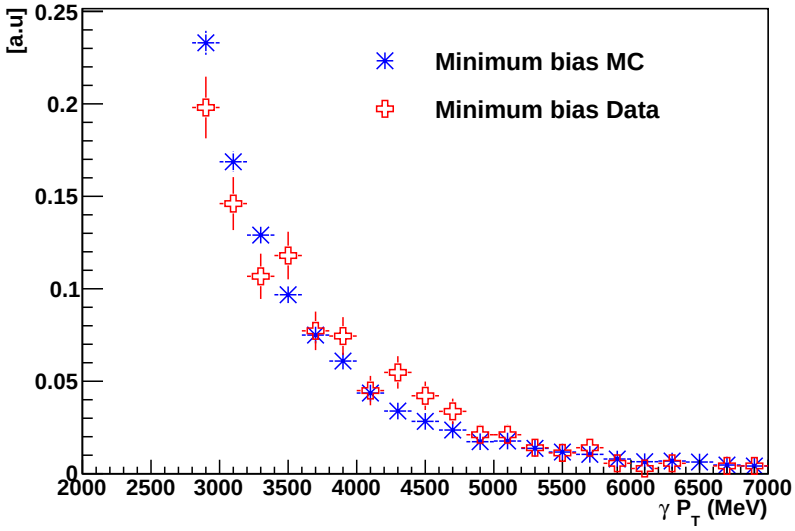

Figure 7.24: P_T distribution of offline reconstructed photons from Minimum bias Data and MC samples, after the application of purity cuts.

These preliminary studies show that it is non optimal to separate *Un*converted photons from the converted ones at the Level 0 trigger. For the 2011 data taking, the HLT1 line for radiative decays will indeed start from L0 Photon and L0 Electron decisions. Also, the requirement of having only 1 or 2 Preshower cells above threshold needs to be revisited, and while the threshold for Preshower cells has been lowered, dedicated study is needed to optimize this cut in the L0 Photon and Electron lines.

7.6 Summary

The first penguin decays reconstructed at LHCb were the $B_d \to K^*\gamma$ and $B_s \to \phi\gamma$ signals from the 2010 data set, which were shown in this chapter. We used a subset of the 2010 data corresponding to $28.6\,\text{pb}^{-1}$, to compare the signal yield and B/S of $B_d \to K^*\gamma$ with MC expectations and investigated the possible reasons for the observed discrepancy between data and simulation.

As discussed in the start of this chapter, the running conditions in 2010 were not optimal for LHCb even though the detector has adapted very well to reconstruct events with higher detector occupancy than it was designed to handle (Chapter 5). However, the selection and trigger efficiency for $B_d \to K^*\gamma$ is a strong function of the detector occupancy in the event and in this chapter we showed first studies aimed at quantifying that effect as a function of the SPD multiplicity, which is a good indicator of the former.

The simulation of the signal sample does not model the SPD multiplicity very well and we corrected the MC efficiency for $B_d \to K^*\gamma$ for the observed SPD multiplicity. This reduces the discrepancy but it is difficult to conclude if the discrepancy is entirely removed, because of the limited statistics.

We also reported a comparison of L0 Photon trigger efficiency in data and simulation, and we found that the simulation does not model the loss in efficiency as a function of SPD multiplicity. We also noted that some of the choices made in the trigger and offline photon building are non optimal and for some cases could be orthogonal to each other. The studies summarised here and some others were an important input to the tuning of the trigger for the 2011 running and will also be used to improve the offline reconstruction of photons.

Chapter 8

Reconstruction of proper time of $B_s \to \phi\gamma$ at LHC*b*

As shown in Chapter 4, the understanding of the B_s proper time reconstruction is a key ingredient of the $B_s \to \phi(K^+K^-)\gamma$ analysis. As discussed in that chapter, the proper time resolution has been parametrized as a double Gaussian while the acceptance as $\epsilon(t) = \frac{(at)^c}{1+(at)^c}$. The parameters obtained from the full LHC*b* Monte Carlo at $\sqrt{s}$ =10 TeV are reported in Table 8.2 (reproduced from Chapter. 4) and the selection cuts are summarised in Table 8.1.

Keeping in view the sensitivity of this analysis to the B_s proper time, no explicit cuts on proper time are made. However, the IPχ^2 and the direction angle cut (this cut requires that the momentum of the B candidate and the vector formed by its flight distance are almost parallel to each other, as shown in Fig. 8.4) are potentially proper time biasing. In Fig. 8.1, the proper time bias (mean of the core Gaussian component in the fit to $\tau_{reco} - \tau_{MC}$) is shown as a function of the IPχ^2 on the charged tracks, where all other cuts except the direction angle have been applied at their nominal values. Fig. 8.2 shows the

same quantity as a function of the direction angle cut on the B_s candidate, where all other cuts except the *Kaon* IPχ^2 have been applied.

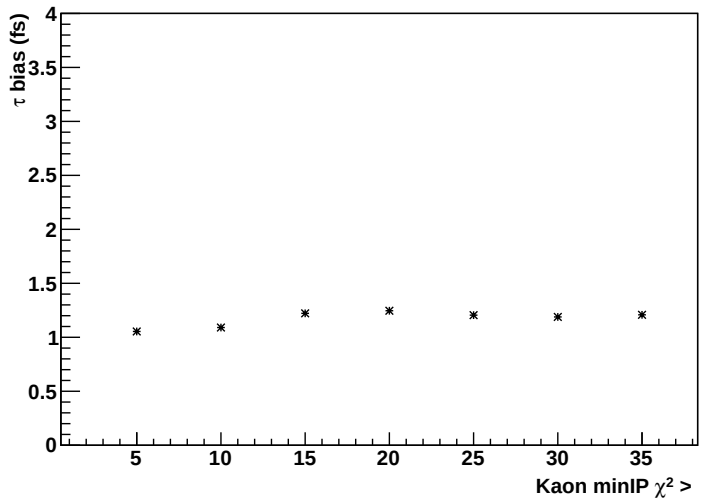

Figure 8.1: Bias in the proper time (in fs) as a function of the minimum IPχ^2 cut on the *kaons* (all other cuts applied, but the direction angle cut).

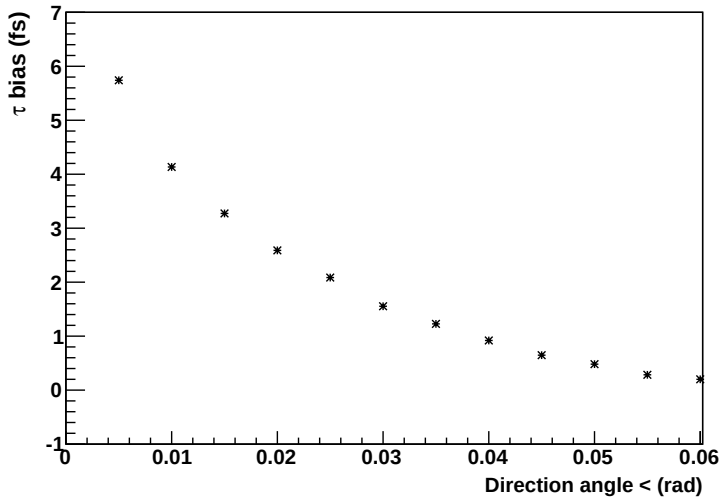

Figure 8.2: Bias in the proper time (in fs) as a function of the direction angle cut (all other cuts applied, but the *kaon* minimum IPχ^2 cut).

While the dependence on the $IP\chi^2$ cut is modest, the bias in the proper time reconstruction depends very strongly on the direction angle cut. However, this cut is the most powerful in discriminating between signal and background [71].

Cut	$B_d \to K^*\gamma$	$B_s \to \phi\gamma$	Comments
$K/\pi\ minimum\ IP\chi^2$	>25	>25	Charged tracks do not point to the PV
$K\ \Delta log\mathcal{L}(K-\pi)$	>3	>3	*Kaon* is more likely to be a *Kaon* than a *pion*
$K\ \Delta log\mathcal{L}(K-p)$	>5	none	*Kaon* is more likely to be a *Kaon* than a *proton*
$\pi\ \Delta log\mathcal{L}(K-\pi)$	<5	none	*pion* is more likely to be a *pion* than a *Kaon*
$\Delta_{Mass}\ K^*/\phi$	<100 MeV	<10 MeV	$m_{PDG\{\phi/K^*\}} - m_{reconstructed\{KK/K\pi\}}$ is reasonable
$Vertex\chi^2\ K^*/\phi$	<9	<9	Charged tracks make a good vertex
γ_{PT}	>2.8 GeV	>2.8 GeV	Photon has high P_T
$B_d/B_s\ minimum\ IP\chi^2$	<9	<9	B_d/B_s is compatible with coming from PV
$B_d/B_s\ directionangle$	<8 mrad	<10 mrad	B_d/B_s points to the PV
$\lvert\cos\theta_H\rvert$	<0.8	<0.8	To reject $B_{\{d,s\}} \to \pi^0\{K^*,\phi\}$ contribution

Table 8.1: The offline selection cuts for $B_d \to K^*\gamma$ and $B_s \to \phi\gamma$ (taken from [71]). The ϕ and K^* are reconstructed in their K^+K^- and $K^+\pi^-$ modes respectively.

σ_{core}	50 fs
σ_{wide}	110 fs
μ_{core}	4 fs
μ_{wide}	22 fs
$fraction_{core}$	83%
$\epsilon(t)$	a = 0.84 , c = 2.16

Table 8.2: Parameters of the proper time resolution and acceptance, obtained from MC09 $B_s \to \phi\gamma$ signal events.

An alternative approach was tried where the direction angle cut was replaced with explicit cuts on the proper time and proper time χ^2, they are discussed in detail later in this chapter. Such cuts get rid of the overall bias but this turns out to be accidental, since the bias is a function of variables as described in the next section.

8.1 Proper time reconstruction

This is an appropriate place for an explanation of the calculation of the proper time. The explicit formula for the proper time is

$$\tau = \frac{m \times \vec{p}.\vec{d}}{|\vec{p}|^2} \tag{8.1}$$

where m is the mass of the B_s candidate, p is its momentum, PV is the primary vertex, SV is the secondary or B_s decay vertex and the distance $d = SV$ - PV is the flight distance of the B_s. A bias in any of these quantities will result in a bias on the calculated proper time τ. Note here that the mass (m) and the momentum (p) are correlated.

The quantity d has contributions from both PV and SV reconstruction, but we can safely assume that the PV is known to a much better precision than the SV and the latter is the dominant source of any bias in d. The ϕ vertex reconstruction is very important here because the ϕ provides all the vertexing information there is in $B_s \rightarrow \phi\gamma$.

The open circles in Fig. 8.3 show the bias in the reconstructed z coordinate of the B_s decay vertex, which is the same point in space as the reconstructed ϕ vertex. As the momentum of the ϕ becomes larger, the lateral separation between the two *kaons* from its decay becomes smaller, resulting in their vertex being reconstructed more upstream than it is.

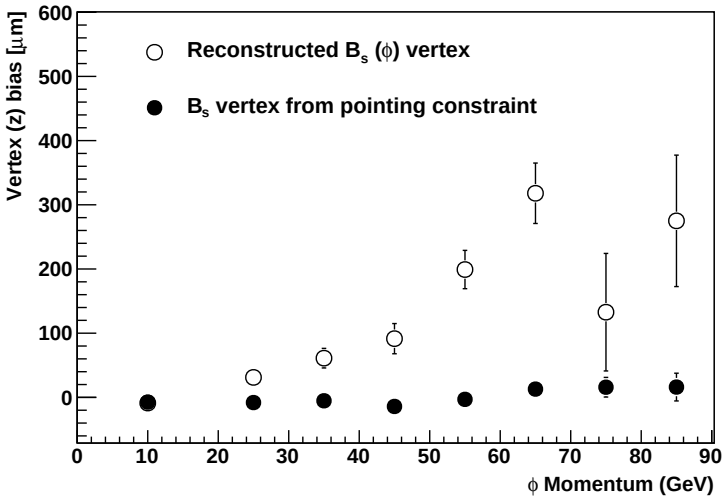

Figure 8.3: Bias in the reconstructed z coordinate of the B_s (or the ϕ meson), where the open circles represent the bias using the reconstructed ϕ vertex. The solid circles represent the same bias when instead of the reconstructed vertex, the B_s decay point that are reached at by the proper time fitter is used.

The B_s vertex can also be determined by using the pointing constraint[1]. The basic idea of the constraint is to vary each input of Eq. 8.1 (PV, SV, p) within its error and reach a configuration where the vectors $\vec{d}$ and $\vec{p}$ are aligned with each other, as illustrated in Fig. 8.4.

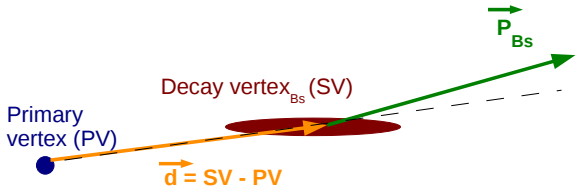

Figure 8.4: Sketch of the "pointing" constraint

The pointing constraint actually arrives at the "true" B_s vertex point very well, i.e. the B_s vertex position determined with this method is unbiased to within $\pm$ 30 μm, as shown by the solid circles in Fig. 8.3.

[1]For this study we have used a full LHCb Monte Carlo simulation of $B_s \to \phi\gamma$ at $\sqrt{s}$ =10 TeV

A proper time fitter is used to calculate the B_s proper time. This uses the values obtained with the pointing constraint for the quantities in Eq 8.1, to determine the B_s proper time. Given that the vertex position reached by the fitter (pointing constraint) is not biased, the only other source of the proper time bias is a bias in the reconstruction of the momentum of the B_s, which is shown in Fig. 8.5.

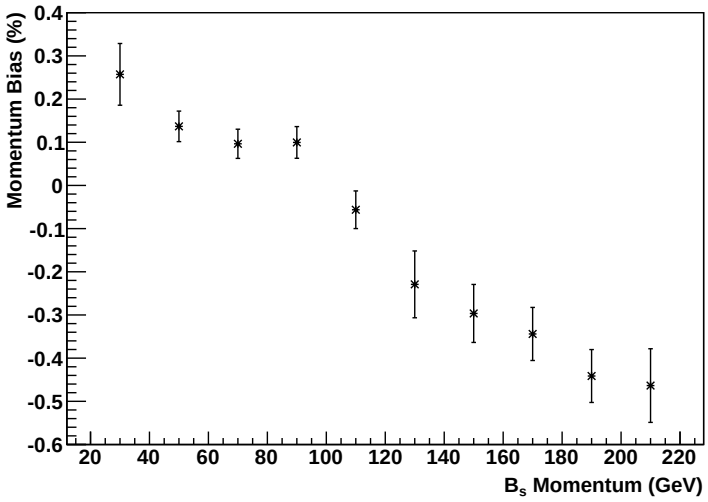

Figure 8.5: Bias in the reconstructed B_s momentum, as a function of the reconstructed B_s momentum. The quantity on the y axis is the mean of the "reconstructed - true" momentum, as a percentage of the reconstructed momentum.

8.1.1 Momentum reconstruction and proper time

As shown in Fig. 8.5, the B_s momentum reconstruction has a small bias of up to 0.5% depending on the momentum, and this effect is large enough to cause the observed proper time bias. Fig. 8.6 shows the proper time bias as a function of the reconstructed B_s momentum. The trend in these figures are consistent since the proper time is over estimated when the momentum is under estimated and vice versa.

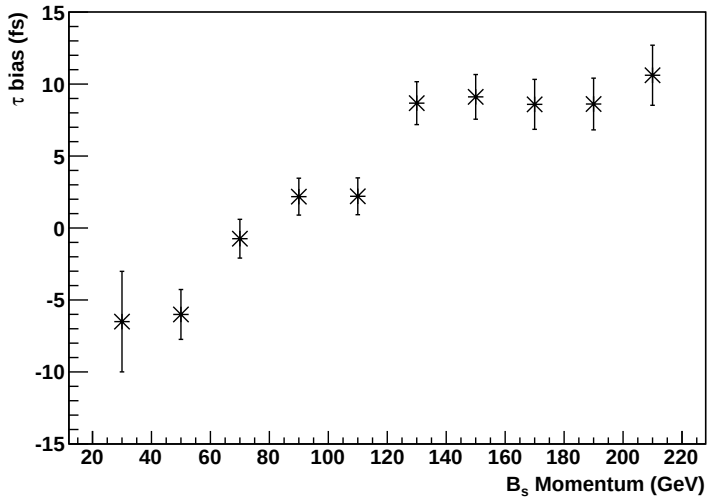

Figure 8.6: Bias in the B_s proper time reconstruction (in fs) as a function of the reconstructed B_s momentum.

The B_s momentum is reconstructed from the momenta of its daughters, the ϕ and the Photon. Figures 8.7 and 8.8 show the bias in the reconstruction of the ϕ and Photon momenta respectively. The bias is plotted as a percentage of the reconstructed momentum, and clearly, the Photon momentum reconstruction produces a much bigger effect than the ϕ momentum.

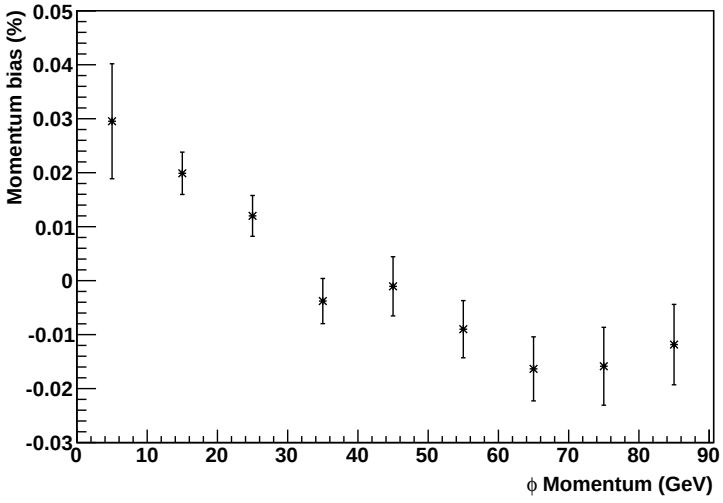

Figure 8.7: Bias in the reconstructed ϕ momentum as a function of the reconstructed ϕ momentum. The quantity on the y axis is the mean of the "reconstructed - true" momentum, as a percentage of the reconstructed momentum.

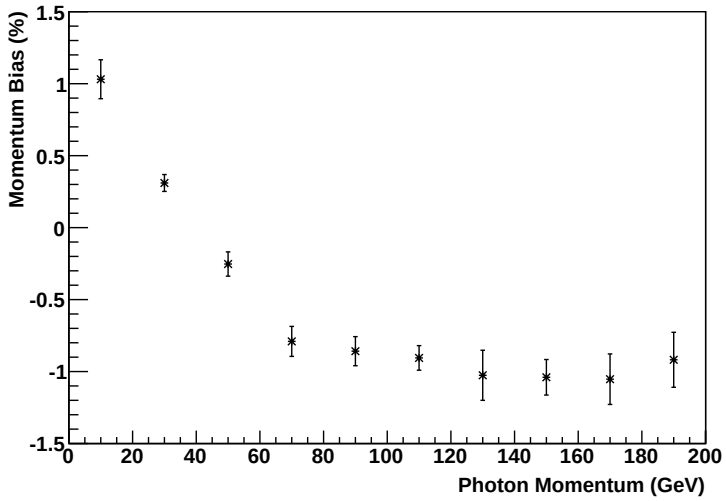

Figure 8.8: Bias in the reconstructed Photon momentum as a function of the reconstructed Photon momentum. The quantity on the y axis is the mean of the "reconstructed - true" momentum, as a percentage of the reconstructed momentum.

However, before concluding that the dominant source of the proper time bias is the photon momentum reconstruction, we should rule out the possibility of the bias being a combination of the photon momentum reconstruction and the downstream bias of the reconstructed vertex. In other words, the question is whether the pointing constraint can find the "best" value of the B_s momentum if given an unbiased vertex.

Therefore, we perform an exercise to assign MC "true" quantities (The errors on them were not changed) to the "reconstructed" photon and ϕ, and combine them to form a B_s candidate. Fig. 8.9 shows the result of this exercise, where the bias in the proper time calculation is plotted as a function of the photon momentum, for the three cases where

- Photon and ϕ had "reconstructed" momenta and vertex (for the ϕ only), represented by crosses. Notice the similarity to Fig. 8.6
- ϕ was assigned the momentum and vertex of its MC counter part, i.e. it had the "true" momentum and vertex position, represented by triangles
- Photon was assigned the momentum of its MC counter part, i.e. it had the "true" momentum, represented by circles

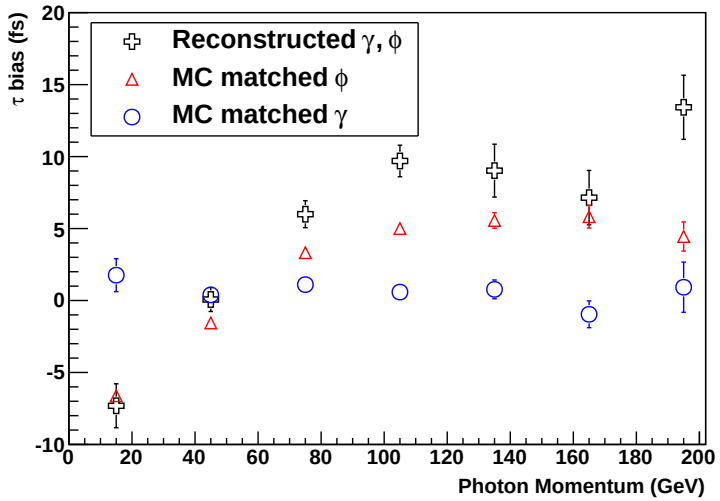

Figure 8.9: The bias in the resolution of proper time (in fs) a function of the photon momentum for the three cases where both ϕ and photon had "reconstructed" momenta and vertex (crosses), when the ϕ was assigned "true" momentum and vertex (triangles) and when the photon was assigned the "true" momentum (circles).

Fig. 8.9 shows that even if it were possible to reconstruct the ϕ vertex and momentum to their *true* values, there would still be a proper time bias, having the same dependence as a function of photon momentum. For an unbiased reconstruction of the proper time, a <1% calibration of the photon momentum is required (Fig. 8.8)[2].

[2]A mass constrained fit on the B_s does not help because the B_s momentum and mass are correlated and both enter into the formula of Eq. 8.1.

8.1.2 Correction for photon momentum

We try to do an event by event correction to the photon momentum assuming that

- The ϕ momentum is reconstructed perfectly, or at least to our required precision (Compare Fig. 8.7 and 8.8)
- The photon momentum reconstruction is only biased in magnitude and not in direction, i.e.

$$\frac{P_{x\gamma}}{E_\gamma} = \frac{P_{x\gamma(true)}}{E_{\gamma(true)}}, \quad \frac{P_{y\gamma}}{E_\gamma} = \frac{P_{y\gamma(true)}}{E_{\gamma(true)}}, \quad \frac{P_{z\gamma}}{E_\gamma} = \frac{P_{z\gamma(true)}}{E_{\gamma(true)}} \tag{8.2}$$

Under these two assumptions, we can derive an equation for the energy of the photon as

$$\begin{aligned}
m_{Bs}^2 &= (E_\gamma + E_\phi)^2 - (\vec{P}_\gamma + \vec{P}_\phi)^2 \\
m_{Bs}^2 &= E_\phi^2 - \vec{P}_\phi^2 + 2E_\gamma E_\phi - 2\vec{P}_\gamma.\vec{P}_\phi \\
m_{Bs}^2 - m_\phi^2 &= 2(E_\gamma E_\phi - P_{x\gamma}P_{x\phi} + P_{y\gamma}P_{y\phi} + P_{z\gamma}P_{z\phi}) \\
m_{Bs}^2 - m_\phi^2 &= 2(E_\gamma E_\phi - E_\gamma(\frac{P_{x\gamma}}{E_\gamma})P_{x\phi} + E_\gamma(\frac{P_{y\gamma}}{E_\gamma})P_{y\phi} + E_\gamma(\frac{P_{z\gamma}}{E_\gamma})P_{z\phi}) \\
E_\gamma &= \frac{m_{B_s}^2 - m_\phi^2}{2(E_\phi - (\frac{P_{x\gamma}}{E_\gamma})P_{x\phi} + (\frac{P_{y\gamma}}{E_\gamma})P_{y\phi} + (\frac{P_{z\gamma}}{E_\gamma})P_{z\phi})}
\end{aligned} \tag{8.3}$$

The above equation gives a reasonable estimate of the photon momentum, if we plug in the true B_s and ϕ mass (5366.3 MeV and 1019.455 MeV respectively). This is shown in Fig. 8.10 where bias in the photon momentum reconstruction is shown as a function of photon momentum, before and after this correction by crosses and squares respectively.

This simple correction improves the bias in the photon momentum by about a factor of 10, and consequently decreases the bias in the B_s proper time. The effect of which can be seen in the reconstruction of the B_s proper time in Fig. 8.11.

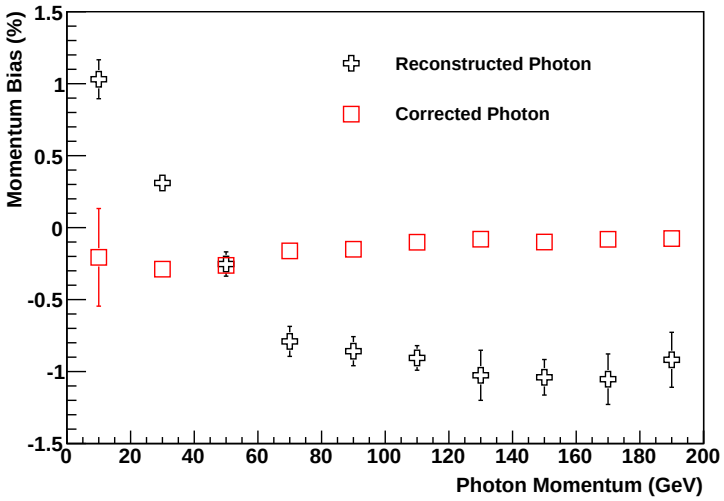

Figure 8.10: The bias in the reconstructed photon momentum as a percentage of the reconstructed photon momentum. The crosses show the quantity for *reconstructed* momentum while the squares show same for *corrected* momentum.

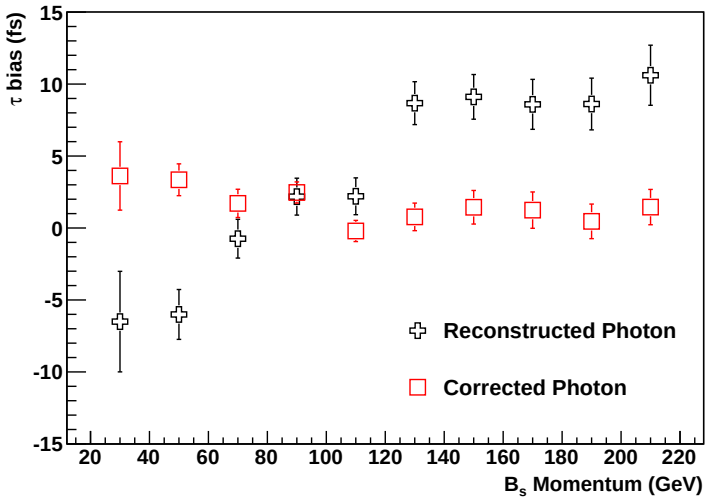

Figure 8.11: The bias in proper time of the B_s, as a function of the reconstructed B_s momentum. The crosses and squares respectively represent the cases where the reconstructed and "corrected" photon momentum was used to reconstruct the B_s candidate.

The conditions in Eq. 8.2 do not hold entirely and there are still some residual biases in the position determination of the photon cluster as well, which results in a directional or angular bias, and are reflected in the graph represented by squares in Fig. 8.10, which should ideally form a straight line. This effect can possibly be calibrated as well, but nevertheless, it is too small to contribute to the resolution for this analysis.

Such a correction for the photon momentum can be extracted from $B_d \to K^*\gamma$ decays in data themselves, reducing the need for MC inputs into this analysis. In data however, the $B_d \to K^*\gamma$ signal has background underneath, and a selection designed to achieve a very low B/S may be necessary to extract the photon momentum correction with sufficient precision.

8.2 The proper time acceptance function

In this section[3] we report the progress on extracting the proper time acceptance function for $B_s \to \phi\gamma$. As shown in Chapter 4, for this analysis, the parameters of the proper time acceptance are required to be known to 2-3 % precision.

The decay $B_d \to K^*\gamma$ has the same topology as $B_s \to \phi\gamma$ since both decays are selected through the same trigger at L0 and HLT1 level, and have very similar cuts in their HLT2 and offline selections (Table. 8.1). The proper time distribution of $B_d \to K^*\gamma$ and $B_s \to \phi\gamma$ selected using the cuts in Table. 8.1[4] is shown in Fig. 8.12 while the proper time acceptance of both decays, fitted with $\epsilon(t) = \frac{(at)^c}{1+(at)^c}$ (Eq. 4.16) is shown in Figs. 8.13 and 8.14.

[3] In this part of the chapter, we use the full LHCb simulation of $B_d \to K^*\gamma$, $B_s \to \phi\gamma$ and $B_s \to J/\psi\phi$ at $\sqrt{s}$ =7 TeV and μ =1.75. The same simulation that was used in Chapter. 7

[4] no trigger requirements made

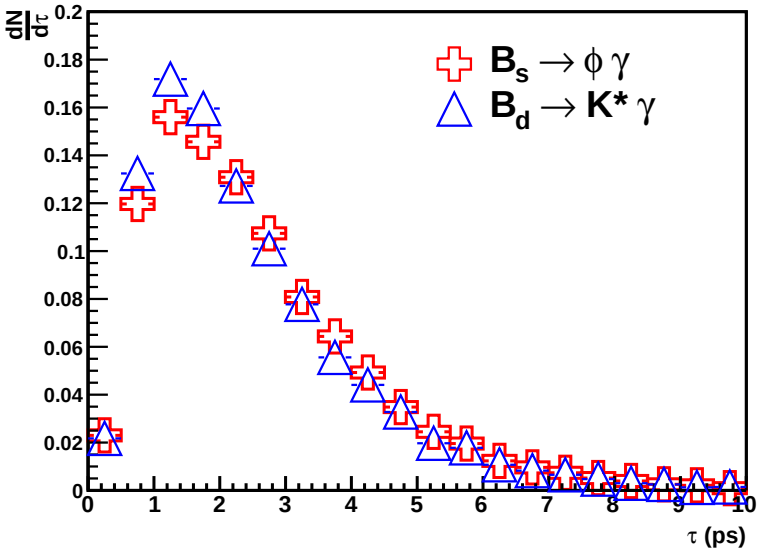

Figure 8.12: Proper time distribution of offline selected $B_d \to K^*\gamma$ and $B_s \to \phi\gamma$ events using the full LHCb Monte Carlo simulation.

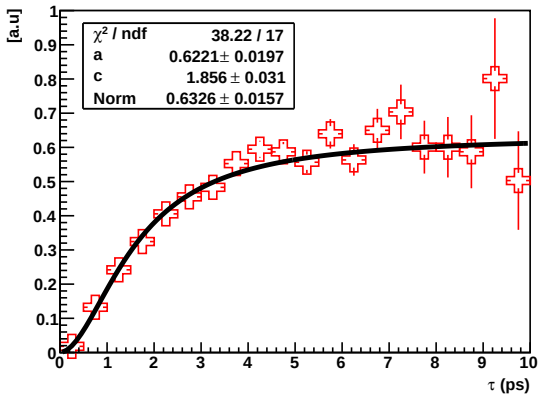

Figure 8.13: Proper time acceptance of the selected $B_s \to \phi\gamma$ events (Fig. 8.12).

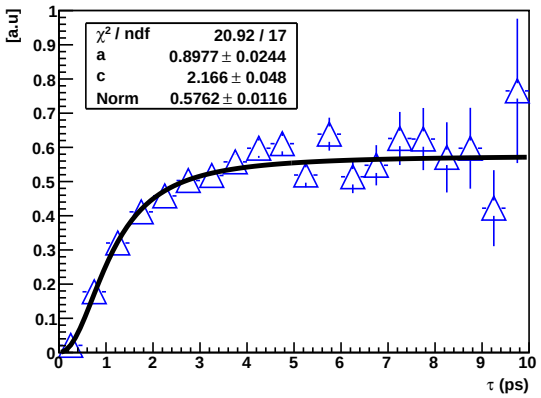

Figure 8.14: Proper time acceptance of the selected $B_d \to K^*\gamma$ events (Fig. 8.12).

The acceptance parameters a and c are quite different for $B_d \to K^*\gamma$ and $B_s \to \phi\gamma$, the difference is believed to be mainly due to the direction angle cut and the $IP\chi^2$ cut on the B candidate. It was shown in the first part of this chapter that the poor reconstruction of the ϕ vertex is not the source of the proper time bias. However, it affects the efficiency to select events with small proper times, in a way that is not reproduced in the K^* vertex.

In the case of $B_d \to K^*\gamma$, the vertex is better defined as compared to the $B_s \to \phi\gamma$ case, where the vertex reconstruction has a larger resolution and downstream bias. This is demonstrated in Figs. 8.15 and 8.16, which show the bias and resolution respectively, on the z coordinate of the K^* and ϕ vertices (from selected $B_d \to K^*\gamma$ and $B_s \to \phi\gamma$ decays), in bins of the momenta of these particles.

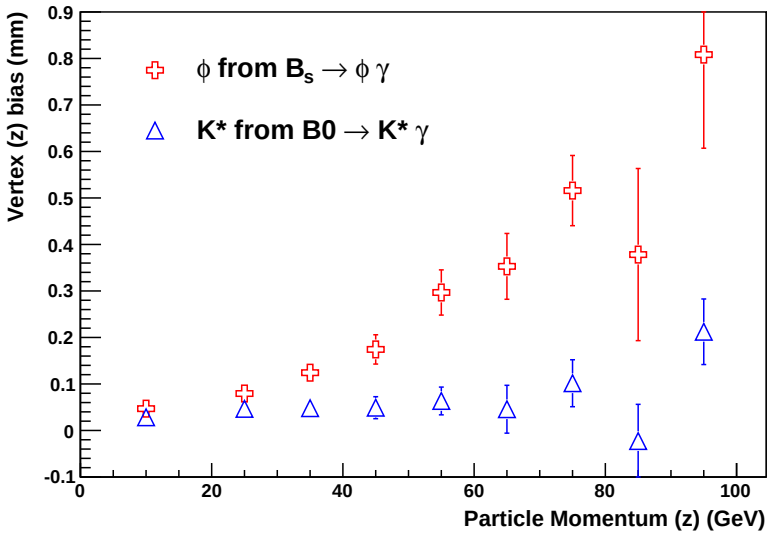

Figure 8.15: Bias in the z coordinate of the vertex, as a function of the momentum of the particle. The crosses represent the ϕ from $B_s \to \phi\gamma$ while the triangles represent the K^* from $B_d \to K^*\gamma$.

To calculate the bias, the distribution of the "reconstructed" z position *minus* the "true" position (in a certain bin of K^* or ϕ momentum) is fitted with two Gaussians. The mean of the dominant Gaussian is quoted as the bias and the width of the dominant Gaussian is quoted as the resolution on the z coordinate.

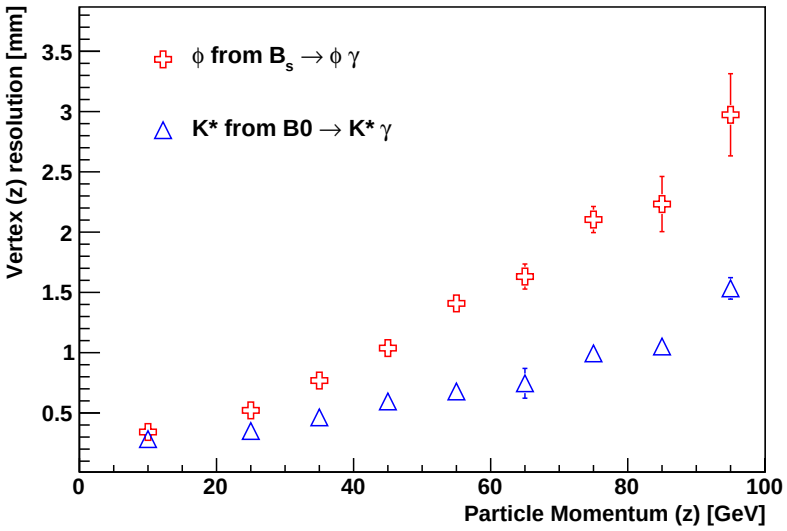

Figure 8.16: Resolution on the z coordinate of the vertex, as a function of the momentum of the particle. The crosses represent the ϕ from $B_s \to \phi\gamma$ while the triangles represent the K^* from $B_d \to K^*\gamma$.

The downstream bias of the reconstructed ϕ vertex can be emulated in $B_s \to J/\psi\phi$ decays. The J/ψ provides a very well measured vertex, so the bias on the ϕ vertex can be extracted by applying the "vertex" cuts used in the $B_s \to \phi\gamma$ selection, on the ϕ and not the B_s vertex in $B_s \to J/\psi\phi$. More technically, we need to apply a "fake" direction angle cut in $B_s \to J/\psi\phi$ to emulate the effect in $B_s \to \phi\gamma$. To do so, in the $B_s \to J/\psi\phi$ sample we use the B_s momentum, the associated primary vertex, and the ϕ vertex rather than the B_s vertex to calculate the direction angle and make the $<$10 mrad cut on it.

The bias in the ϕ vertex reconstruction in $B_s \to J/\psi\phi$, compared to $B_s \to \phi\gamma$ and $B_d \to K^*\gamma$ is shown in Fig. 8.17, which also shows the comparison with the J/ψ vertex. The downstream bias of the ϕ vertex in $B_s \to \phi\gamma$ is closely reproduced in $B_s \to J/\psi\phi$ decays and can be used to do a correction for the $B_s \to \phi\gamma$ vertex, taking into account the ϕ momentum spectra in $B_s \to \phi\gamma$ and $B_s \to J/\psi\phi$, since large statistics of the latter decay will be collected during 2011.

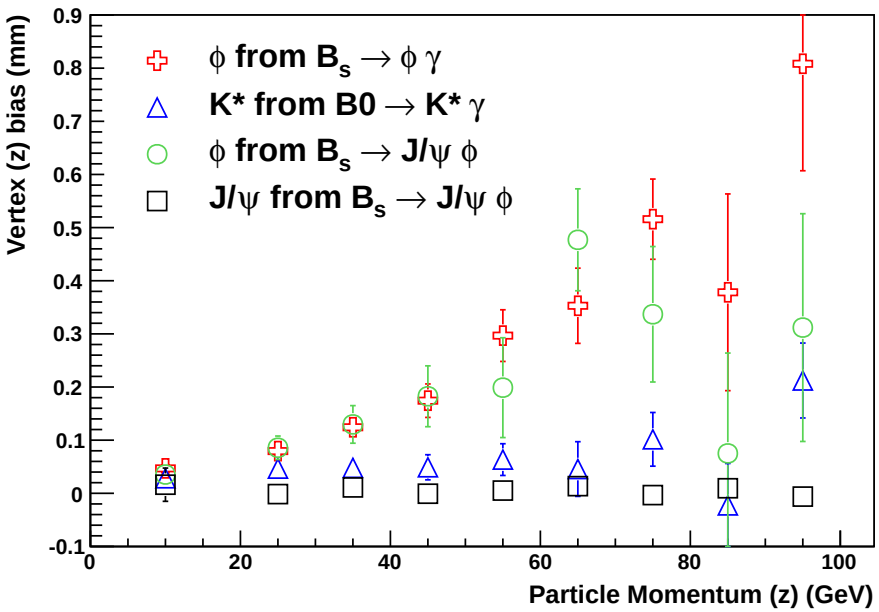

Figure 8.17: Bias in the z coordinate of the vertex, as a function of the momentum of the particle. The crosses represent the ϕ from $B_s \to \phi\gamma$ while the triangles represent the K^* from $B_d \to K^*\gamma$. The circles represent the bias when the direction angle cut is applied on the ϕ rather than the B_s vertex in $B_s \to J/\psi\phi$, while the squares represent the same for the J/ψ vertex.

In the next section we present a study of the ϕ vertex reconstruction from some data taken in 2010.

8.2.1 $\phi \to KK$ vertex reconstruction in data

With the data collected in early 2010 ($< 5\,\text{pb}^{-1}$), we compare the ϕ vertex reconstruction in data to the simulation. For this study we used an offline selected MC signal sample of $B_s \to \phi\gamma$ and Minimum bias sample from data and simulation[5]. We will compare the resolution in bins of polar angle[6] because the ϕ candidates in Minimum bias are more "forward" (have low polar angle) as compared to the ones in the $B_s \to \phi\gamma$ MC sample, as shown in Fig. 8.18.

[5]The latter two at $\sqrt{s} = 7\,\text{TeV}$ while the signal sample from a simulation at $\sqrt{s} = 10\,\text{TeV}$.
[6]The angle with the z coordinate of LHCb, or the LHC beam pipe.

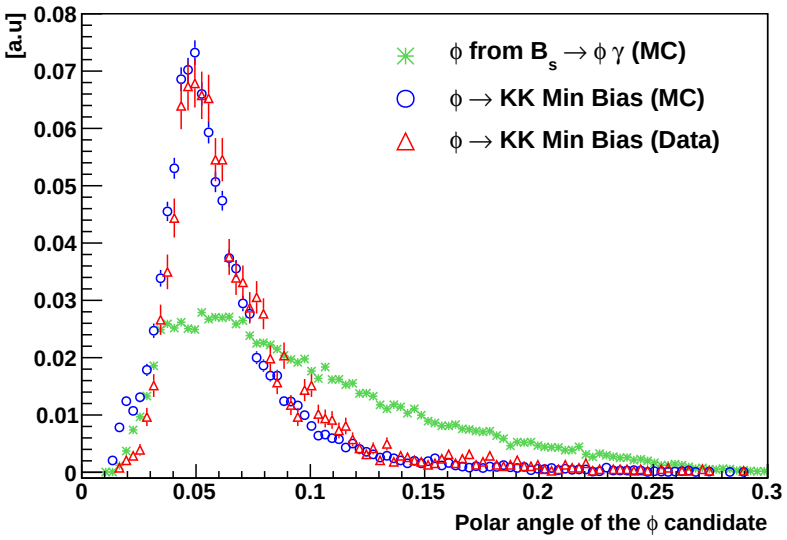

Figure 8.18: Polar angle of the $\phi \to KK$ candidates in selected $B_s \to \phi\gamma$ MC sample (stars), Minimum bias MC (open circles) and Minimum bias data (open triangles).

In the signal sample we use the MC true decay vertex of the B_s to estimate the ϕ vertex resolution. The same can be done in the simulated Minimum bias sample, but not in data. Therefore, in the Minimum bias samples we assume that the "true" decay vertex of the reconstructed $\phi \to KK$ candidate was the primary vertex (PV) the ϕ was associated to[7].

Fig. 8.19 shows that the associated PV is a good approximation for the "true" decay vertex of the ϕ in Minimum bias. In this figure, the difference between the z coordinates of the "MC true" ϕ vertex and its associated PV is shown.

To estimate the resolution on the ϕ vertex, we fit the distribution of the z coordinate of the reconstructed vertex *minus* the z coordinate of the associated PV[8] (we use the MC true vertex in the $B_s \to \phi\gamma$ signal MC sample) with a double Gaussian, and quote the width of the dominant Gaussian.

[7]The associated PV is defined as the one with respect to which the ϕ candidate has the least $IP\chi^2$.
[8]We refit the PV after excluding the two tracks used to reconstruct the ϕ candidate.

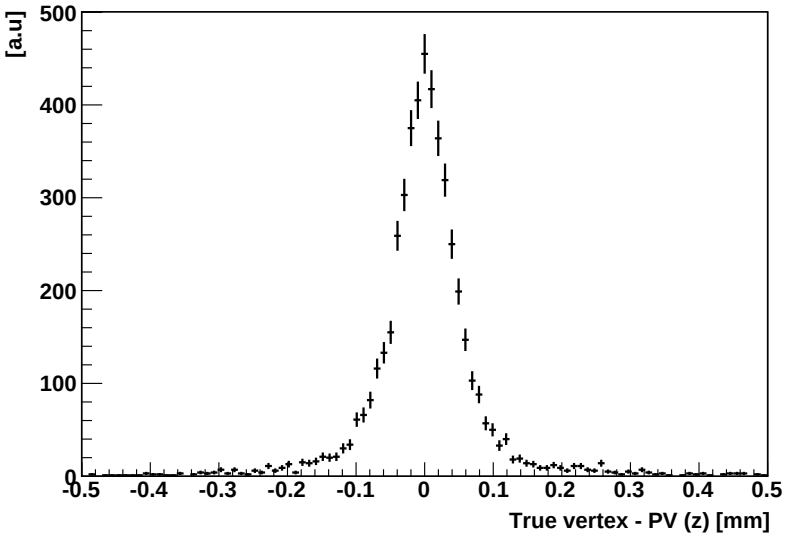

Figure 8.19: From the Minimum bias MC sample, the difference between the z coordinates of the "MC true" ϕ vertex and its associated PV. The RMS of the distribution is $\sim 80\,\mu$m.

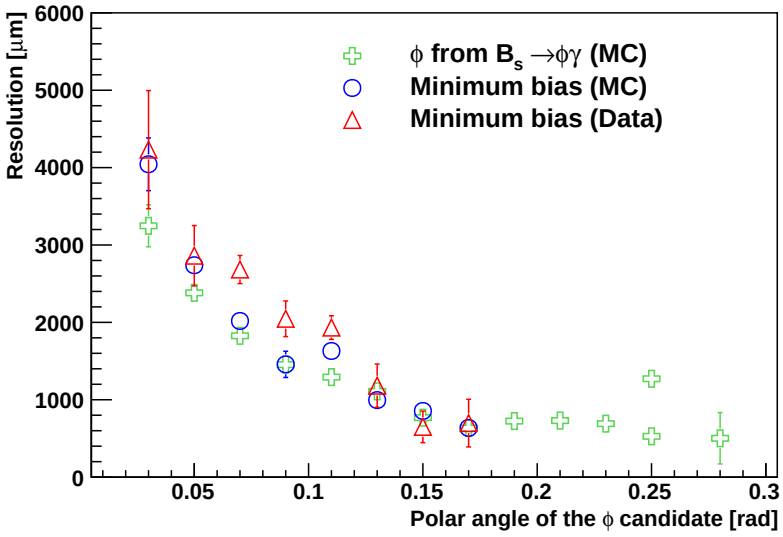

Figure 8.20: The resolution on the ϕ vertex as a function of the polar angle of the ϕ for $B_s \to \phi\gamma$ signal sample (crosses), for the MC Minimum bias sample (circles) and Minimum bias data (triangles).

In Fig. 8.20 we show the resolution for the $B_s \to \phi\gamma$ signal sample, and the two Minimum bias samples. Even though there is some discrepancy in low polar angle bins, the data agree quite well with the simulation, both Minimum bias and signal $B_s \to \phi\gamma$.

This was a very early data study to compare the vertexing of the $\phi \to KK$ decay in data to simulation. As the understanding of trigger and selection cuts optimal for radiative decays evolves, similar studies for the ϕ vertex bias and resolution can be performed with the $B_s \to J/\psi\phi$ sample from data, as LHCb has collected a few thousand in 2010 already. In the next section we briefly discuss an approach which can possibly allow a straightforward extraction of the $B_s \to \phi\gamma$ proper time acceptance from $B_d \to K^*\gamma$ decays.

8.2.2 Extracting $B_s \to \phi\gamma$ proper time acceptance from $B_d \to K^*\gamma$

The proper time acceptance depends heavily on the cuts made on the ϕ vertex, especially the direction angle cut. The ideal channel to extract the $B_s \to \phi\gamma$ acceptance is $B_d \to K^*\gamma$, since it has the same topology, triggers and selection cuts, and its proper time distribution is known. If the direction angle cut can be avoided, $B_d \to K^*\gamma$ can be used to extract the $B_s \to \phi\gamma$ acceptance straight away from data themselves. In order to demonstrate this point, we compare the acceptance for $B_d \to K^*\gamma$ and $B_s \to \phi\gamma$ with two alternative set of cuts where the direction angle and the $IP\chi^2$ cuts on the B candidate have been replaced with explicit cuts on the proper time, as listed below[9]

- Set A: $\tau\chi^2 < 2.0$ and $c\tau > 0.175\,\text{mm}$
- Set B: $\tau\chi^2 < 4.0$ and $c\tau > 0.35\,\text{mm}$

A comparison of the proper time acceptance of $B_s \to \phi\gamma$ for these and the default cuts is shown in Fig. 8.21.

[9]These 'alternative' selections was not developed by the author, and it should be noted that this work is very preliminary and no reference is available at the moment.

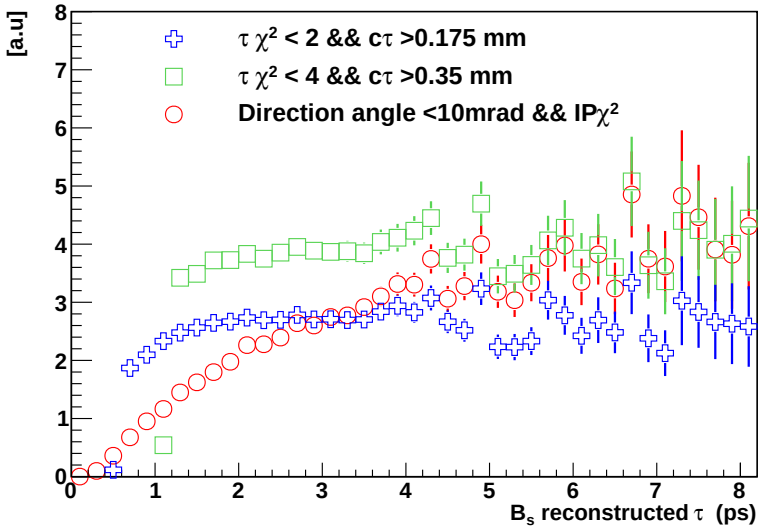

Figure 8.21: Proper time acceptance function for selected $B_s \to \phi\gamma$ events. The circles show the acceptance for all selection cuts in Table 8.1, while the crosses and squares show the acceptance when the $IP\chi^2$ and direction angle cut on the B_s have been replaced with $c\tau > 0.175$ && $\tau_{\chi^2} < 2$ and $c\tau > 0.35$ && $\tau_{\chi^2} < 4$ respectively.

With these sets of cuts, the proper time acceptance of $B_s \to \phi\gamma$ has a faster turn on and matches well with the acceptance for $B_d \to K^*\gamma$. The latter point is demonstrated in Fig. 8.22 and 8.23 which show the comparison between the parameters a and c of the proper time acceptance function for $B_d \to K^*\gamma$ and $B_s \to \phi\gamma$ decays and the x axis represents which cuts were applied to select the decays.

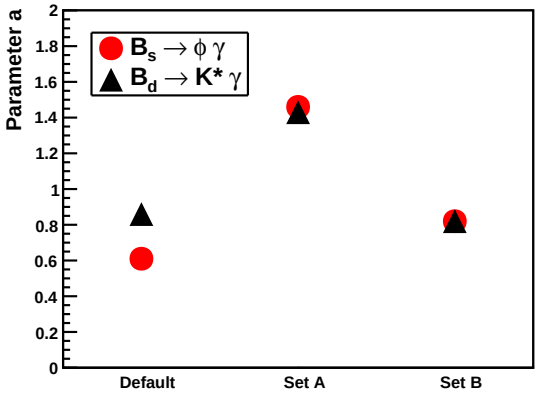

Figure 8.22: Parameter a of the proper time acceptance for different sets of cuts represented by the x axis. The circles and squares represent the parameter value for $B_s \to \phi\gamma$ and $B_d \to K^*\gamma$ respectively.

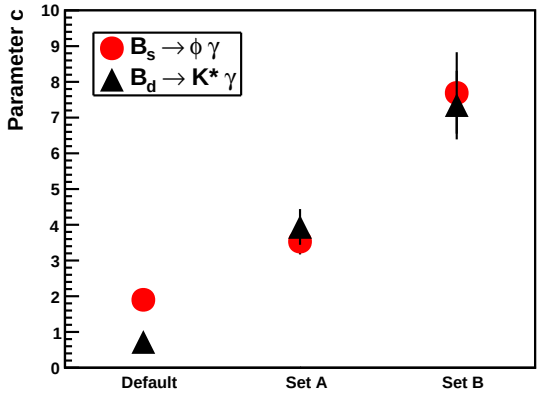

Figure 8.23: Parameter c of the proper time acceptance for different sets of cuts represented by the x axis. The circles and squares represent the parameter value for $B_s \to \phi\gamma$ and $B_d \to K^*\gamma$ respectively.

With the application of direction angle and $IP\chi^2$ cuts, the parameters a and c are very different for $B_s \to \phi\gamma$ and $B_d \to K^*\gamma$, while they agree very well for the two decays if explicit proper time cuts are made. While this is a desirable result, it should be noted that the background suppression or signal purity/significance achievable with these alternative cuts is not known yet.

The measurement of the $B_d \to K^*\gamma$ lifetime in data by using the $B_d \to K^*\gamma$ proper time acceptance extracted from MC can also be a useful study to estimate how well MC reproduces the data. It can also be useful to determine which selection cuts are most robust against the background level and other biases. Work has been started in this direction and such studies will be possible relatively soon after the start of the LHC physics run in 2011.

Chapter 9

Conclusions and outlook

The Standard Model of Particle Physics has been very successful at describing the nature of fundamental particles and the forces that govern their interactions. The many unexplained phenomena (Chapter. 2) point to the fact that it is not the complete story, and the search for beyond Standard Model or New Physics is the driving force for Particle Physics today.

New Physics can be looked for in decays of heavy flavour mesons and a powerful recent entrant in this field is LHCb, which is custom built to reconstruct rare decays of mesons containing b (and c) quarks. These mesons provide a rich ground for New Physics searches as they exhibit the phenomenon of *CP* violation, which essentially means that matter and anti matter behave differently at the fundamental level. *CP* violation is encoded in the CKM matrix, which represents the mixing between the physical states of quarks and their weak eigen states. The single complex phase of this matrix encodes the *CP* violation predicted by the Standard Model and is usually studied by constraining the *Unitarity* triangle (Chapter. 3).

The presence of New Physics particles can also be inferred by measuring the branch-

ing ratios, angular distributions and helicities of the final state particles of loop decays and comparing them to the Standard Model predictions as discussed in Chapter. 4. The measurement of the fraction of left to right handed photons in the decay $B_s \to \phi\gamma$ is an important test of the Standard Model and will be made at LHCb in future, as it requires high statistics. This ratio is sensitive to New Physics as it is predicted to be very small ($\sim$ 1%) in the Standard Model, so a significantly larger value will be a sign of New Physics. Also of interest is the direct CP asymmetry in $B_d \to K^*\gamma$, which again has a <1% prediction in the Standard Model.

In this thesis, we reported sensitivity studies for the analysis of $B_s \to \phi\gamma$ at LHCb, along with the studies for the systematics which need to be controlled/calibrated for this analysis (Chapter. 4). We also showed the signal from $B_s \to \phi\gamma$ and $B_d \to K^*\gamma$ from the 2010 data set and some studies to validate the Level 0 Photon trigger (Chapter. 7). We also show that the calibration of the photon momentum is very important for the $B_s \to \phi\gamma$ analysis and can be performed with $B_d \to K^*\gamma$ and the latter can also be used to extract the $B_s \to \phi\gamma$ proper time acceptance function from data themselves (Chapter. 8). The ϕ provides all the vertexing information in $B_s \to \phi\gamma$ and is very important for the proper time acceptances and we show that the $B_s \to J/\psi\phi$ signal can be used to validate the reconstruction of ϕ vertex in data. We also showed some preliminary studies of ϕ vertex reconstruction validation from the 2010 data set (Chapter. 8).

At the time of writing this thesis, the LHC machine is about to start the 2011 physics run at $\sqrt{s} = 7\,\text{TeV}$. During this run, LHCb is foreseen to collect 2-3 fb^{-1} of integrated luminosity, allowing the experiment to make many "roadmap" measurements. This data sample will provide large statistics of $B_d \to K^*\gamma$ and $B_s \to J/\psi\phi$ decays which are very important calibration channels for the $B_s \to \phi\gamma$ analysis as discussed in Chapter. 8. The

next LHC run will allow the experiment to collect 5-10 fb^{-1}, using which LHCb will be able to make the high statistics measurements like the $B_s \to \phi\gamma$ analysis for the fraction of right to left handed photons in a B_s decay. The LHCb detector performance has been validated with the 2010 data set (corresponding to $\sim 37\,\text{pb}^{-1}$) as discussed in Chapter. 5. The efficiency and resolution on the quantities of interest have been measured to be in good agreement with the predictions by simulation, despite the fact that the running conditions in 2010 were much more difficult than the detector was designed to handle.

Many studies reported in this thesis are "work in progress", and given the excellent performance and data taking efficiency of the LHCb detector, the roadmap measurements with $B_d \to K^*\gamma$ and $B_s \to \phi\gamma$ will be made as soon as sufficient statistics are collected. These measurements will be one of the important measurements at LHCb, which will either discover New Physics or exclude a large parameter space of various New Physics models. The author looks forward to exciting measurements from LHCb and other LHC detectors.

Bibliography

[1] F Soomro and V Belyaev. HLT2 exclusive selections for $B_s \to \phi\gamma$ and $B_d \to K^*\gamma$. LHCb-PUB-2010-007, 2010.

[2] Christopher Blanks, Fatima Soomro, and Jacopo Nardulli. The laser alignment and monitoring system for the lhcb rich detectors. LHCb-PUB-2011-014, 2011.

[3] S. L. Glashow. Partial Symmetries of Weak Interactions. *Nucl. Phys.*, 22:579–588, 1961.

[4] Steven Weinberg. A model of leptons. *Phys. Rev. Lett.*, 19(21):1264–1266, 1967.

[5] Henning Flacher et al. Revisiting the global Electroweak fit of the Standard Model and beyond. *Eur. Phys. J.*, C60:543–583, 2009. Updated results and plots available at: http://gfitter.desy.de/.

[6] Precision Electroweak Measurements and Constraints on the Standard Model. 2009. Updated results and plots available at: http://lepewwg.web.cern.ch/LEPEWWG/.

[7] Peter W. Higgs. Spontaneous symmetry breakdown without massless bosons. *Phys. Rev.*, 145(4):1156–1163, 1966.

[8] T. W. B. Kibble. Symmetry breaking in non-abelian gauge theories. *Phys. Rev.*, 155(5):1554–1561, 1967.

[9] F. Zwicky. On the masses of nebulae and of clusters of nebulae. *Astrophysical Journal, vol. 86, p.217*, 1937.

[10] A. D. Sakharov. Violation of *CP* Invariance, *C* Asymmetry, and Baryon Asymmetry of the Universe. 1967.

[11] Patrick Huet and Eric Sather. Electroweak baryogenesis and standard model cp violation. *Phys. Rev. D*, 51(2):379–394, Jan 1995.

[12] Search for the Rare Decays $B_{s(d)} \to \mu^+\mu^-$. (CDF note 9892), 2009.

[13] G Lanfranchi. Search for the rare decays $B_d^0 \to \mu^+\mu^-$ and $B_s \to \mu^+\mu^-$ with LHCb. LHCb-TALK-2011-030. Presented at *Les Rencontres de Physique de la Vallee d'Aoste*, La Thuile, Italy, 27 Feb - 5 Mar 2011.

[14] C. S. Wu, E. Ambler, R. W. Hayward, D. D. Hoppes, and R. P. Hudson. Experimental test of parity conservation in beta decay. *Phys. Rev.*, 105(4):1413–1415, 1957.

[15] Richard L. Garwin, Leon M. Lederman, and Marcel Weinrich. Observations of the failure of conservation of parity and charge conjugation in meson decays: the magnetic moment of the free muon. *Phys. Rev.*, 105(4):1415–1417, 1957.

[16] T. D. Lee and C. N. Yang. Question of parity conservation in weak interactions. *Phys. Rev.*, 104(1):254–258, 1956.

[17] T. D. Lee, Reinhard Oehme, and C. N. Yang. Remarks on possible noninvariance under time reversal and charge conjugation. *Phys. Rev.*, 106(2):340–345, 1957.

[18] L. Landau. On the conservation laws for weak interactions. *Nuclear Physics*, 3(1):127 – 131, 1957.

[19] J. H. Christenson, J. W. Cronin, V. L. Fitch, and R. Turlay. Evidence for the 2π Decay of the K_2^0 Meson. *Phys. Rev. Lett.*, 13(4):138–140, 1964.

[20] M.S Sozzi. *Discrete symmetries and CP violation*. Oxford University press, 2008.

[21] Nicola Cabibbo. Unitary symmetry and leptonic decays. *Phys. Rev. Lett.*, 10(12):531–533, 1963.

[22] Lincoln Wolfenstein. Parametrization of the kobayashi-maskawa matrix. *Phys. Rev. Lett.*, 51(21):1945–1947, 1983.

[23] K Nakamura et al. Review of particle physics. *Journal of Physics G: Nuclear and Particle Physics*, 37(075021), 2010.

[24] A. Hocker, H. Lacker, S. Laplace, and F. Le Diberder. A new approach to a global fit of the CKM matrix. *The European Physical Journal C - Particles and Fields*, 21:225–259, 2001. 10.1007/s100520100729.

[25] Image from http://ckmfitter.in2p3.fr/plots_ICHEP10/#etiquette0.

[26] O. L. Buchmüller and H. U. Flächer. Fit to moments of inclusive $B \to X_c \ell \nu$ and $B \to X_s \gamma$ decay distributions using heavy quark expansions in the kinetic scheme. *Phys. Rev. D*, 73(7):073008, 2006.

[27] V Klose. Measurement of $|V_{cb}|$ and $b \to c l \nu$ Transitions at *BABAR*. *Journal of Physics: Conference Series*, 110(5):052028, 2008.

[28] Sheldon Stone Marina Artuso, Elisabetta Barberio. B meson decays. *PMC Physics A, 2009, 3:3*, 2009.

[29] From http://pdglive.lbl.gov/listings1.brl?quickin=Y.

[30] R. Fulton et al. Observation of B-meson semileptonic decays to noncharmed final states. *Phys. Rev. Lett.*, 64(1):16–20, 1990.

[31] H. Albrect et al. Observation of semileptonic charmless B meson decays. *Physics Letters B*, 234(3):409 – 416, 1990.

[32] K. Nakamura et al. (Particle Data Group), J. Phys. G 37, 075021 (2010), http://pdg.lbl.gov.

[33] A. V. Artamonov et al. Study of the decay $K^+ \to \pi^+\nu\bar{\nu}$ in the momentum region $140 < P_\pi < 199\, MeV/c$. *Phys. Rev. D*, 79(9):092004, 2009.

[34] Andrzej J. Buras, Martin Gorbahn, Ulrich Haisch, and Ulrich Nierste. Rare Decay $K^+ \to \pi^+\nu\bar{\nu}$ at the Next-to-Next-to-Leading Order in QCD. *Phys. Rev. Lett.*, 95(26):261805, 2005.

[35] A. O. Bazarko et al. Determination of the strange quark content of the nucleon from a next-to-leading-order qcd analysis of neutrino charm production. *Zeitschrift fur Physik C Particles and Fields*, 65:189–198, 1995. 10.1007/BF01571875.

[36] From http://www.utfit.org/foswiki/pub/UTfit/Old/.

[37] K. Vervink. Measurements of the CKM angle ϕ_1/β from *Belle* and *BABAR*. 2008. In proceedings of Flavlour Physics and *CP* violation 2008, Taipei, Taiwan.

[38] Heavy Flavor Averaging Group. Averages of b-hadron, c-hadron, and τ-lepton Properties. 2010.

[39] Michael Gronau and David London. Isospin analysis of *CP* asymmetries in B decays. *Phys. Rev. Lett.*, 65(27):3381–3384, 1990.

[40] B. Adeva et al. Roadmap for selected key measurements of LHCb. 2009.

[41] Michael Gronau and Daniel Wyler. On determining a weak phase from charged B decay asymmetries. *Physics Letters B*, 265(1-2):172 – 176, 1991.

[42] Michael Gronau and David London. How to determine all the angles of the unitarity triangle from $B_d \to DK_s$ and $B_s \to D\phi$. *Physics Letters B*, 253(3-4):483 – 488, 1991.

[43] David Atwood, Isard Dunietz, and Amarjit Soni. Enhanced *CP* Violation with $B \to KD^0(\bar{D}^0)$ Modes and Extraction of the Cabibbo-Kobayashi-Maskawa Angle γ. *Phys. Rev. Lett.*, 78(17):3257–3260, 1997.

[44] S Cohen, M Merk, and E Rodrigues. $\gamma + \phi_s$ sensitivity studies from combined $B_s^0 \to D_s^- \pi^+$ and $B_s^0 \to D_s^\mp K^\pm$ samples at lhcb. Technical Report LHCb-2007-041. CERN-LHCb-2007-041, CERN, Geneva, 2007.

[45] Robert Fleischer. New strategies to extract β and γ from $B_d \to \pi^+\pi^-$ and $B_s \to K^+K^-$. *Physics Letters B*, 459(1-3):306 – 320, 1999.

[46] R. Fleischer. $B_{s,d} \to \pi\pi, \pi K, KK$: status and prospects. *The European Physical Journal C - Particles and Fields*, 52:267–281, 2007. 10.1140/epjc/s10052-007-0391-7.

[47] et al B. Aubert. Measurement of *CP* Asymmetries and Branching Fractions in $B0 \to \pi^+\pi^-$, $B0 \to K^+\pi^-$, $B0 \to \pi^0\pi^0$, $B0 \to K^0\pi^0$ and Isospin Analysis of $B \to \pi\pi$ Decays. 2008.

[48] H. Ishino et al. Observation of Direct *CP* Violation in $B^0 \to \pi^+\pi^-$ Decays and Model-Independent Constraints on the Quark-Mixing Angle ϕ_2. *Phys. Rev. Lett.*, 98(21):211801, 2007.

[49] David Atwood, Michael Gronau, and Amarjit Soni. Mixing-Induced *CP* Asymmetries in Radiative B Decays in and beyond the Standard Model. *Phys. Rev. Lett.*, 79(2):185–188, 1997.

[50] Patricia Ball and Roman Zwicky. Time-dependent *CP* asymmetry in $B \to K^*\gamma$ as a (quasi) null test of the standard model. *Phys. Lett.*, B642:478–486, 2006.

[51] David Atwood, Tim Gershon, Masashi Hazumi, and Amarjit Soni. Mixing-induced *CP* violation in $B \to P_1 P_2 \gamma$ in search of clean new physics signals. *Phys. Rev. D*, 71(7):076003, 2005.

[52] John Ellis, Thomas Hahn, Sven Heinemeyer, Keith A. Olive, and Georg Weiglein. WMAP-compliant benchmark surfaces for MSSM Higgs bosons. *Journal of High Energy Physics*, 2007(10):092, 2007.

[53] Kenneth G. Wilson and Wolfhart Zimmermann. Operator product expansions and composite field operators in the general framework of quantum field theory. *Comm. Math. Phys.*, 24(2):87–106, 1972.

[54] Andrzej J Buras and Robert Fleischer. Quark mixing, *CP* violation and rare decays after the top quark discovery. *Adv. Ser. Direct. High Energy Phys.*, 15(hep-ph/9704376. TUM-HEP-275-97. TTP-97-15):65–238. 180 p, 1997.

[55] Gerhard Buchalla, Andrzej J. Buras, and Markus E. Lautenbacher. Weak decays beyond leading logarithms. *Rev. Mod. Phys.*, 68(4):1125–1244, 1996.

[56] P Ball et al. B decays. B decays at the LHC. (hep-ph/0003238. CERN-TH-2000-101):112 p, 2000.

[57] Tobias Hurth and Mikihiko Nakao. Radiative and Electroweak Penguin Decays of B Mesons. *Annual Review of Nuclear and Particle Science*, 60(1):645–677, 2010.

[58] Measurement of Forward-Backward Asymmetry in $B_d \to K^{(*)}\mu\mu$ and first observation of $B_s \to \phi\mu\mu$. (CDF note 10047), 2010.

[59] See http://www-cdf.fnal.gov/physics/new/bottom/091112.blessed-b2smumu_afb/index.html.

[60] Measurement of the differential branching fraction and forward-backward asymmetry for $B \to K^* l + l-$. *Phys. Rev. Lett.*, 103(17):171801, Oct 2009.

[61] Angular distributions in the decay $B \to K^* l + l-$. *Phys. Rev. D*, 79(3):031102, Feb 2009.

[62] Schune J. Lefrancois, MH. Measuring the photon polarization in $b \to s\gamma$ in the $B_d \to K^* e^+ e^-$ decay channel. CERN-LHCb-2009-008, 2009.

[63] Franz Muheim, Yuehong Xie, and Roman Zwicky. Exploiting the width difference in $B_s \to \phi\gamma$. *Physics Letters B*, 664(3):174 – 179, 2008.

[64] Heavy Flavor Averaging Group. Averages of b-hadron and c-hadron Properties at the End of 2007. 2007.

[65] O Leroy. Prospects for CP violation in $B_s^0 \to J/\psi\phi$ from first LHCb data. LHCb-TALK-2011-028. Presented at *Les Rencontres de Physique de la Vallee d'Aoste*, La Thuile, Italy, 27 Feb - 5 Mar 2011.

[66] The LHCb Collaboration. Measurement of $\sigma(\mathrm{pp} - > b\bar{b}\ \mathrm{X})$ at $\sqrt{s} = 7$ TeV in the forward region. *Physics Letters B*, 694:209–216, 2010.

[67] J.Albrecht. *Fast Track Reconstruction for the High Level Trigger of the LHCb Experiment.* PhD thesis, University of Heidelberg, Germany, 2009.

[68] A. Augusto Alves et al. The LHCb Detector at the LHC. *JINST*, 3:S08005, 2008.

[69] S. Borghi. Performance of the Tracking system at the LHCb experiment. *Proceedings of Science*, (PoS ICHEP 2010, 005), 2010.

[70] Silvia Borghi. Performance of the tracking system at the lhcb experiment. LHCb-TALK-2010-094, 2010. Presented at the 35th International Conference on High Energy Physics, Paris, France, Jul 2010.

[71] L.Shchutska, A.Golutvin, and I.Belyaev. Study of radiative penguin decays $B_s \to \phi\gamma$ and $B_d \to K^*\gamma$ at LHCb. CERN-LHCb-2007-030, 2007.

[72] A Golutvin. Status and Results from LHCb. LHCb-TALK-2011-029. Presented at *Les Rencontres de Physique de la Vallee d'Aoste*, La Thuile, Italy, 27 Feb - 5 Mar 2011.

[73] A. Golutvin. LHCb status and highlights. *Proceedings of Science*, (PoS ICHEP 2010, 541), 2010.

[74] S. Borghi. First Results from the LHCb Vertex Locator. *Proceedings of Science*, (PoS ICHEP 2010, 030), 2010.

[75] Andrew Powell. Particle ID at LHCb. LHCb-TALK-2010-104, 2010. Presented at the 35th International Conference on High Energy Physics, Paris, France, Jul 2010.

[76] LHCb rich technical design report. CERN-LHCC-2000-037, 2000.

[77] C D'Ambrosio, B J Franek, C Gaspar, M Laub, R Lindner, F Muheim, A Papanestis, and FJP Soler. Monitoring, alignment and control of the rich detectors. Technical Report LHCb-2000-080, CERN, Geneva, 2001.

[78] See `http://www.etm.at/`.

[79] See `http://dim.web.cern.ch/dim/`.

[80] From `http://www-pnp.physics.ox.ac.uk/~powell/LHCC/`.

[81] LHCb Trigger System Technical Design Report. CERN-LHCC-2003-031, 2003.

[82] LHCb calorimeters technical design report. CERN-LHCC-2000-036, 2000.

[83] Beam test results of the LHCb electromagnetic calorimeter. CERN-LHCb-2007-149, 2008.

[84] Measurement of the J/ψ production cross-section at $\sqrt{s} = 7$ TeV in LHCb. LHCb-CONF-2010-010, 2010.

[85] Measurements of B^0 mesons production cross-section in pp collisions at $\sqrt{s} = 7$ TeV using $B^0 \to D^{*-}\mu^+\nu_\mu X$ decays. LHCb-CONF-2010-012, 2010. Presented at the 35th International Conference on High Energy Physics, Paris, France, Jul 2010.

[86] The LHCb collaboration. Prompt charm production in pp collisions at $\sqrt{s} = 7$ tev. LHCb-CONF-2010-013, 2010. Presented at : 6th International Workshop on the CKM Unitarity Triangle, Warwick, United Kingdom, 6 - 10 Sep 2010.

[87] Vladimir V Gligorov. A single track HLT1 trigger. CERN-LHCb-PUB-2011-003, 2011.

[88] K Senderowska, M Witek, and A Zuranski. HLT1 Electromagnetic Alley. LHCb-PUB-2009-001, 2010.

[89] M Pepe-Altarelli. LHCb First Results and Prospects. LHCb-TALK-2011-021. Presented at *Aspen Winter Conference on Particle Physics: New Data from the Energy Frontier*, Aspen, United States Of America, 13 - 18 Feb 2011.

[90] `https://twiki.cern.ch/twiki/bin/view/LHCb/TCK`.

[91] F Soomro. $B \to X_s\gamma$ and $B \to X_s l^+ l^-$ decays at LHCb. LHCb-PROC-2011-003. Presented at the *6th International Workshop on the CKM Unitarity Triangle*, Warwick, United Kingdom, 6 - 10 Sep 2010.